8024

CONTRACTOR REPORT

SAND87—7014
Unlimited Release
UC—62

Point-Focus Concentrator Reflector Assembly

Phase I

Solar Kinetics, Inc.
10635 King William Drive
Dallas, TX 75220

Prepared by Sandia National Laboratories Albuquerque, New Mexico 87185 and Livermore, California 94550 for the United States Department of Energy under Contract DE-AC04-76DP00789

Printed November 1987

Issued by Sandia National Laboratories, operated for the United States Department of Energy by Sandia Corporation.

Printed in the United States of America
Available from
National Technical Information Service
U.S. Department of Commerce
5285 Port Royal Road
Springfield, VA 22161

NTIS price codes
Printed copy: A08
Microfiche copy: A01

SAND87-7014
Unlimited Release
Printed November 1987

Distribution
Category UC-62

Point-Focus Concentrator Reflector Assembly - Phase I

Solar Kinetics, Inc.
10635 King William Drive
Dallas, Texas 75220

Sandia Contract #21-3695

ABSTRACT

A point-focus concentrator reflective assembly was developed in Phase I on contract 21-3695 under the direction of Sandia National Laboratories, Albuquerque. This concentrator is conventional in presentation, yet innovative in detail. The development concentrated on structural efficiency and production design to achieve a high performance at minimum cost. The concentrator design achieves stiffness and strength through the integration of two structural elements. The optical element provides the reflective surface accuracy; a secondary support structure provides resistance to uniform and non-uniform load conditions. A retractable receiver strut, which moves the power conversionassembly out of focus in emergency power loss, was also incorporated. This same assembly provides maintenance access to the engine near ground level. A full-scale optical element was fabricated. Slope error was measured at 1 mrad. Concentrator performance was projected to be 88 percent, optical. This point-focus concentrator reflector assembly design provides low weight, low cost, and simplicity. Our analysis indicates these benefits are gained without impairing performance.

CONTENTS

LIST OF FIGURES

LIST OF TABLES

1.0 INTRODUCTION

An integral part of the National Solar Thermal Technology Five Year Plan is the continued improvement of point-focus technology. Parabolic dish point-focus concentrators offer near-term prospects for the production of electricity and high-quality thermal energy from solar energy. As part of this plan, a research and development project was initiated to develop a high performance point-focus concentrator. This report documents all work completed under Phase I of contract 21-3695, performed under the direction of Sandia National Laboratories, Albuquerque.

The objective of this development was to design a parabolic concentrator reflective assembly of substantially increased value. The foundation for design and comparison was defined as existing technology developed from previous research and development efforts. This scope was limited, in Phase I efforts, to investigation of the reflector assembly only. The reflector design was demonstrated with prototype sample fabrications.

The presentation that follows is divided into three major sections: Design; Manufacturing, Construction, and Cost; and Prototype Development. Section 2.0, Design, provides the requirements imposed upon the development, a baseline design that addressed these requirements, and a detailed investigation and refinement of the baseline concentrator. Manufacturing, Construction, and Cost (Section 3.0) is a descriptive section on fabrication of the concentrator reflector assembly and, ultimately, the specific cost. Section 4.0, Prototype Development, incorporates all efforts at demonstration of the proposed design.

1.1 Major Conclusions

The reflective assembly selected for development was fabricated from 30 identical petals that radiated from the vertex to perimeter and formed a complete paraboloid of revolution. These optical panels were designed to provide the stiffness required to maintain accuracy under operational loads. A rear support structure provided for load transfer to the drive, particularly in survival conditions (Figures 1.1 and 1.2). Two separate components were selected for the structure in reaction to two separate design criteria: deflection under operational load and stress/failure in survival conditions. The structures were not independent. Coupling between the optical elements and supporting structure was considered in the detailed design.

The stiffness relationship between the optical panels and support structure was a key element in design. The optical panel

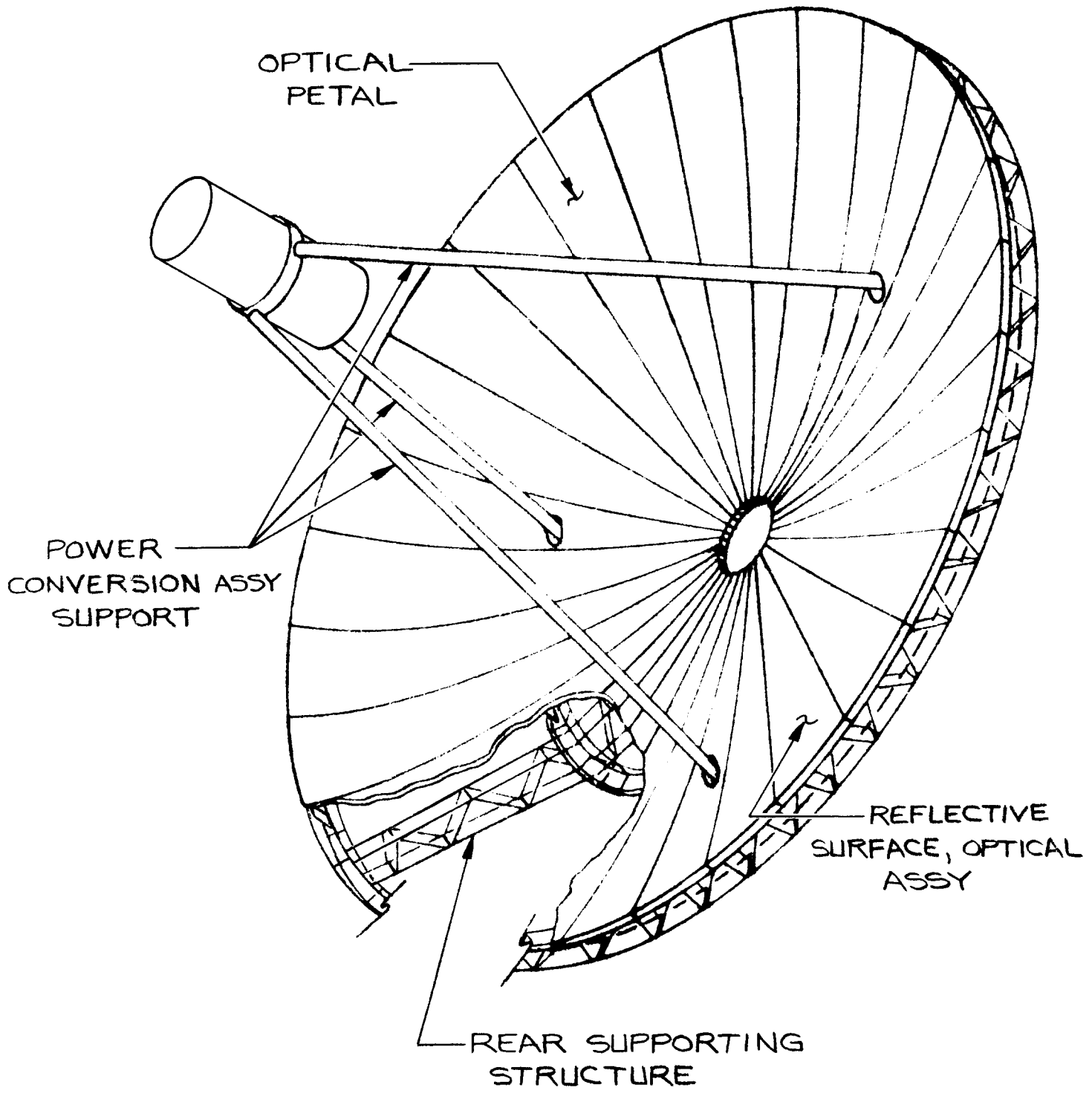

FIG. 1.1 REFLECTIVE ASSEMBLY, FRONT VIEW

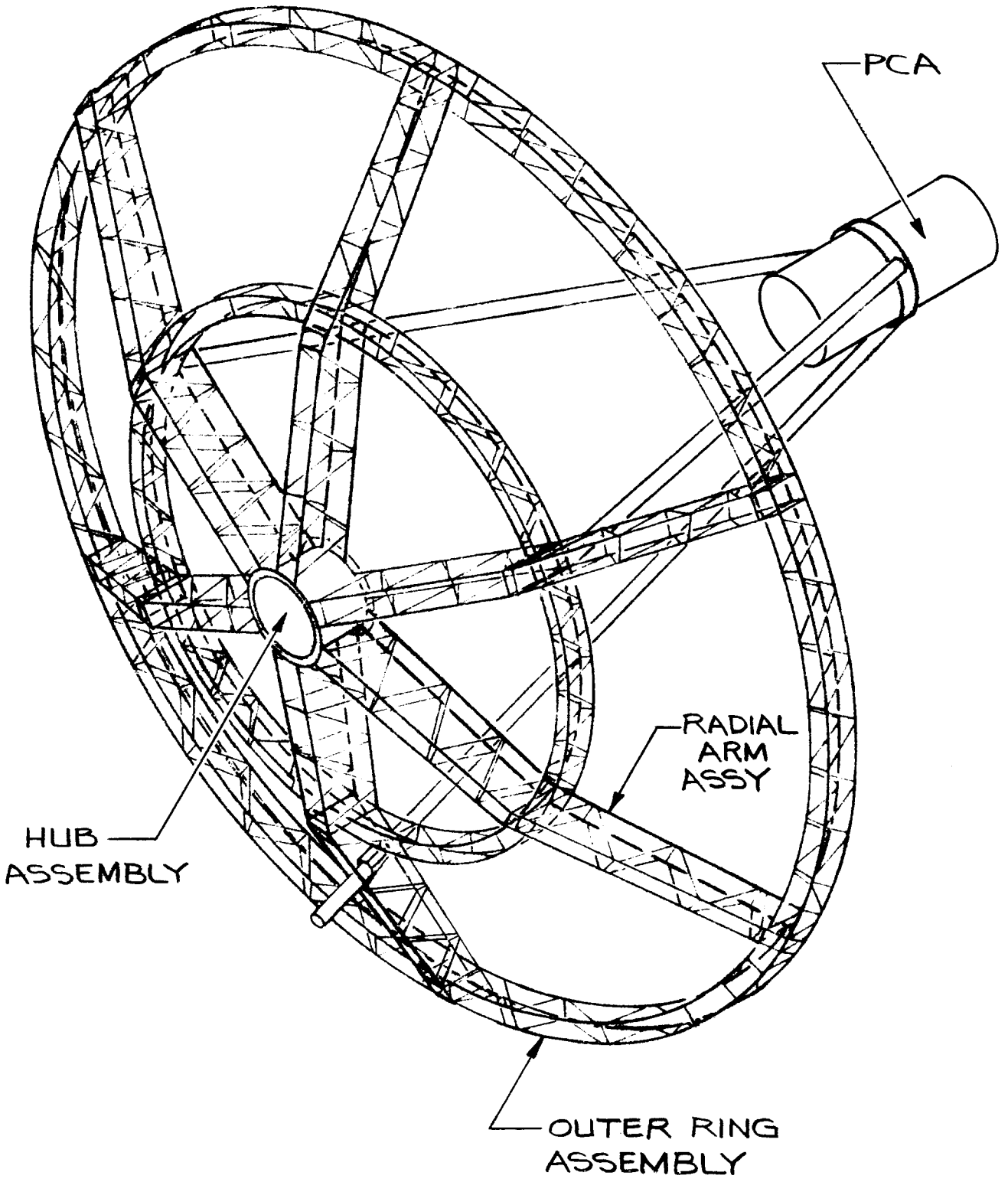

FIG. 1.2 REAR SUPPORT STRUCTURE (OPTICAL PANELS REMOVED FOR CLARITY)

exhibited sandwich panel construction: two skins were separated by a core to create an extremely stiff structure per unit of weight. The ability to carry load without failure tended to decrease with specific stiffness. The open web construction employed in the rear structure could carry large loads per unit of weight. The final design balanced the stiffnesses of the reflector assembly and support structure to distribute the load transfer according to survival ability in the assembly.

Conventional manufacturing processes were defined for optical panel components and the entire rear structure assembly. Critical tolerances in the design were associated with petal assembly only. Optical accuracy was largely divorced from the steel support structure through adjustment provisions during construction. Adjustment was required once. The optical stiffness of the concentrator was imparted after adjustment by bonding each petal to form a continuous optical element.

Prototype development clearly demonstrated the accuracy of petal assemblies designed for this concentrator. Direct profile measurement equipment, developed under this contract, indicated the panel slope error was 1 mrad (one standard deviation, normal distribution).

Optical efficiency was projected at 89 percent, thermal efficiency at 83 percent (800 °C receiver). Concentrator reflector assembly weight was kept below 60 lbs/m^2. Installed costs were predicted at \$75-100/m^2 for an annual production volume of 1,000 to 10,000 concentrators, respectively.

1.2 Recommended Follow-Up Activities

The scope of Phase I effort was limited to the development of a reflective assembly detailed design. The results of this development indicated that a design conventional in presentation, and innovative in detail, could provide high performance at low weight and cost. Based upon the results and projections of this development, Solar Kinetics, Inc. recommends that this contract be continued through a second phase of development.

The second phase in this development effort was defined as a detailed design of all components other than the reflective assembly (Phase I) and the power conversion assembly, followed by a full-scale prototype fabrication and installation at the Distributed Receiver Test Facility in Albuquerque. This work is recommended to complete the development design and demonstrate the projected performance of an integrated concentrator design.

If a cost-effective pedestal, drive, foundation, and control system suitable for the concentrator designed under Phase I is available, a limited path of Phase II development might initially

be pursued. This limited effort would demonstrate performance projections and, ultimately, survivability through the manufacture of a full-scale reflector assembly installed on an existing drive system. This limited scope is recommended as a minimum follow-up effort.

2.0 CONCENTRATOR DESIGN

The optical assembly and support structure were integrally coupled and required design analysis as a unit. These components were parametrically developed in isolation and combined for detailed design. This chapter presents the design development for the optical assembly, support structure, and power conversion assembly (PCA) support. This effort was initiated by the establishment of the design constraints and goals, and proceeded through the development of a baseline and detailed design.

The design basis section presents the assumptions and contract requirements that established the basis for the concentrator design and the impact of these constraints on dish geometry. The development of the baseline concentrator design is presented in the following section. The baseline design served as a foundation for the detailed design. Material selection, truss and ring configuration, and the optical panel concept were developed as part of the baseline. The first step of the detailed design was the rigorous refinement of the baseline assumptions. The optical element and rear structure stiffness were analyzed and defined. Required structural properties of the support structure were established and the components were sized. The last section of this chapter presents the development of a PCA support that provides emergency defocus without an external power source.

2.1 Design Basis

Several design parameters were established early in this development effort to serve as a basis for the concentrator design. These parameters had a significant impact on the value of the final product and warrant examination. The contract defined certain requirements such as thermal production level and wind speeds. These constraints and extensions of contract requirements were used as our basis. Three issues of particular importance are presented here: performance, environmental loading, and production rates.

2.1.1 Performance. The value of any concentrator is directly tied to optical performance. To achieve high optical performance, it is critical that a design balance appropriate concentrator shape and size with realistic optical errors.

The base performance requirements were established by the contract. The required power through the receiver aperture was 100 to 160 kW (kilowatts) with 1000 W/m^2 (Watts/square meter) incident solar energy. The steady state rim flux was required to be less than 100 kW/m^2. These conditions were to be met in a 6.8 m/s wind. A power input of 130 kW was selected as the design basis because it represented a range value. A receiver temperature of 800 °C was chosen for performance analyses. This temperature was chosen to be representative for electric power production in accordance with the DOE Five Year Plan.

A reasonable set of optical criteria was defined to meet these requirements. Dish size and the ratio of focal length to diameter (f/D) were established. Error budgets for slope and tracking, along with reflectivity and shading, were defined based on experience with previous concentrators. These values were convolved with size and shape values to predict performance.

All errors were assumed to have circular normal distributions. This assumption simplified the performance analysis and allowed the use of existing analytical tools. Although this assumption was not strictly accurate, optical performance was dominated by the slope error for which the assumption was representative. All error terms are reported as one standard deviation.

Slope error is defined as any error best described as occurring on incidence and reflection. Its effect is doubled and its impact is significant by comparison to errors that occur in the reflected profile only. There are several sources of slope error: fabrication, installation alignment, and structural deformation under load. The slope error was initially established at 4 mrad and later reduced to 3 mrad based upon the results of prototype facet testing and detailed structural analyses.

Tracking error was arbitrarily established at 2 mrad. This value was not verified in this phase of the contract. Drives and controls were restricted to the second phase and were outside the scope of this effort. The sensitivity of this assumption was minimal.

The sun is not a point source nor is its light collimated, and beam dispersion results. This dispersion was accounted for as "sun shape." It was assumed to have a circular normal distribution of 2.3 mrad. Although this was a rough approximation of the true error, parametric analysis indicated that this selection was not critical.

The specularity and reflectivity corresponded to commerically available reflective film laminated to a substrate. A specularity of 1.25 mrad and a reflectivity of 95 percent were defined.

Blocking was found to be a sensitive assumption. Blocking occurred from film gaps at each seam, receiver shadowing, and struts blocking both incident and concentrated energy. Blocking was strongly influenced by the baseline design, and through successive refinement, the blocking was established at 5.3 percent of the gross aperture area.

Previous work by Jaffe (Ref. 1) has shown the optimum range of f/D for parabolic concentrators to be 0.4 to 0.6. The trade-off is relatively insensitive to error selection. This shape range is virtually always adopted if fabrication does not create cost or technical obstacles. Consequently, the optimum f/D was established at 0.5 without iteration.

The concentrator diameter and receiver aperture were varied to meet the contract requirements for energy input and rim flux, while providing maximum collector efficiency. This analysis was performed on COPS, a ray-trace program (Ref. 2). The optical efficiency as a function of receiver aperture is presented in Figure 2.1. To arrive at the collector efficiency, the optical efficiency must be convolved with the receiver efficiency. The receiver curve is presented in Figure 2.2. This curve represents the heat loss (radiative, convective, and conductive) from the receiver as a function of aperture. Figure 2.3 presents collector efficiency as a function of aperture. Collector efficiency is a product of optical and receiver efficiencies. As shown, the maximum collector efficiency is approximately 84 percent.

The rim flux was found to be 100 kW/m^2 at a radius of 0.18 m, which was also the aperture radius that gave the maximum collector efficiency. This was significant in that the rim flux requirement was not restrictive. The concentrator could be optimized for performance without regard to rim flux.

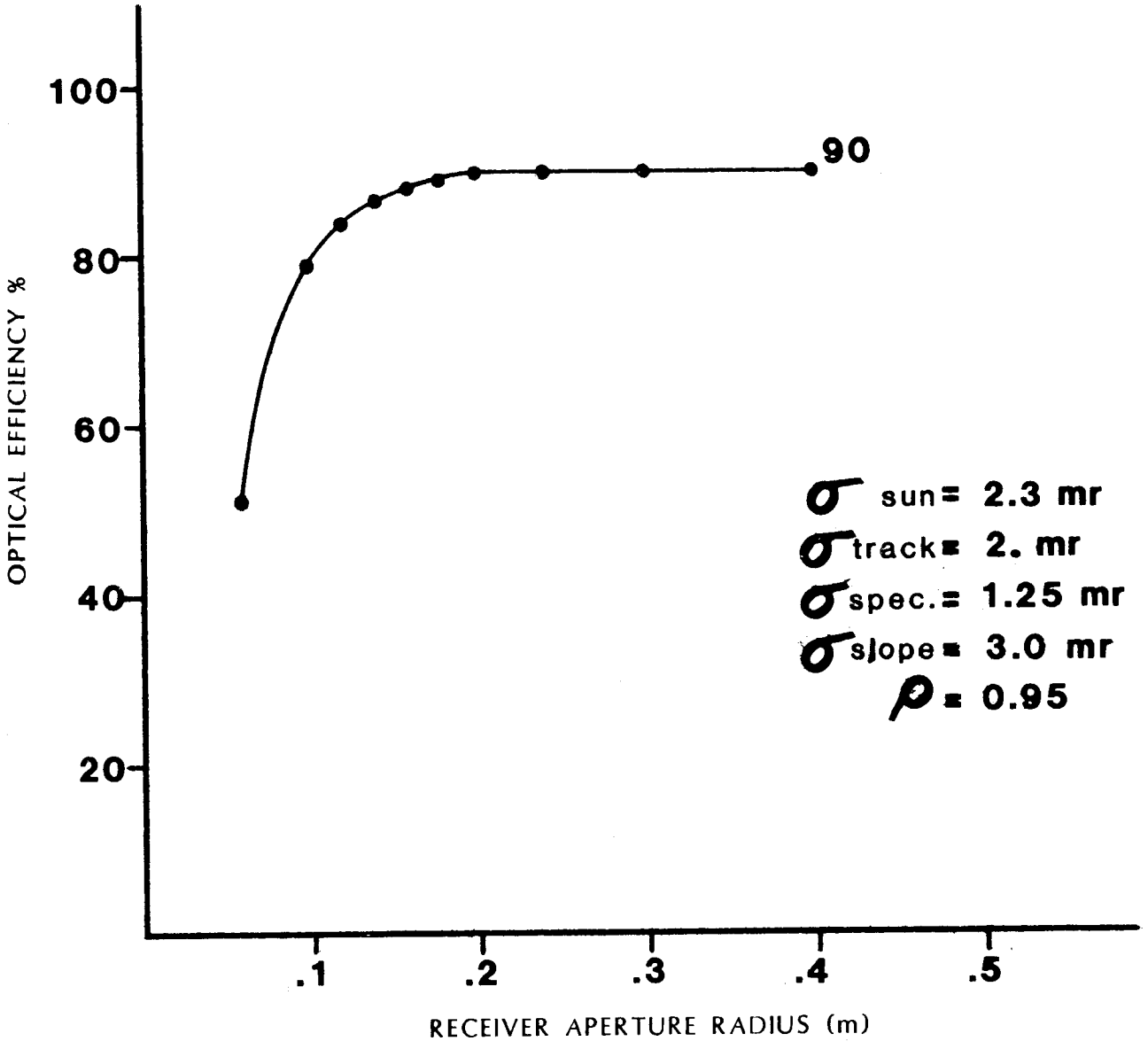

FIG. 2.1 OPTICAL EFFICIENCY VS. RECEIVER APERTURE RADIUS

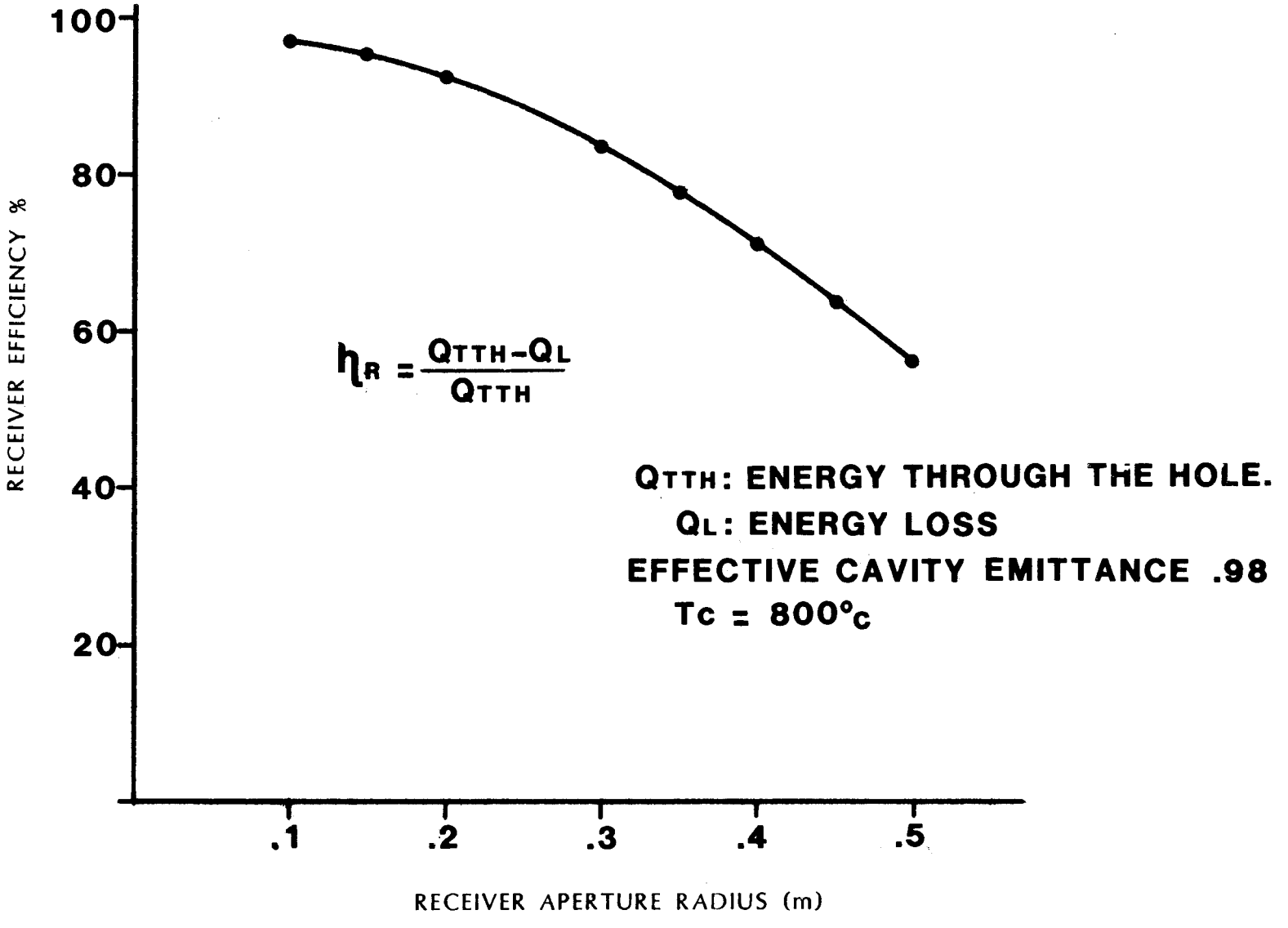

FIG. 2.2 RECEIVER EFFICIENCY VS. RECEIVER APERTURE RADIUS

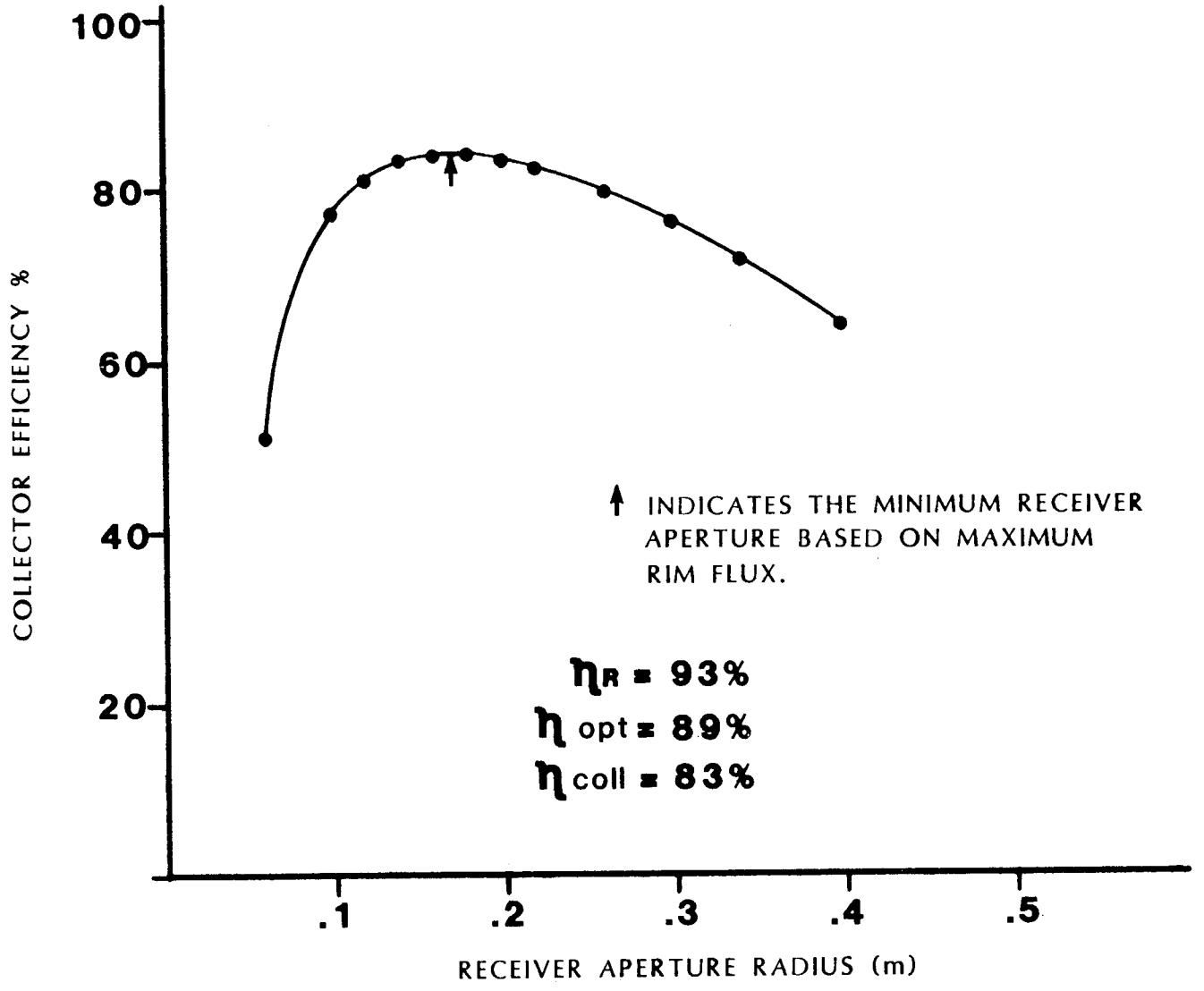

FIG. 2.3 COLLECTOR EFFICIENCY VS. RECEIVER APERTURE RADIUS

The final receiver aperture was established slightly larger than optimum to provide better performance under degraded conditions (e.g., sun shape increase due to atmosphere). The operating aperture was established at 0.20 m.

The summary of inputs and results is shown in Table 2.1.

2.1.2 Environmental Requirements. Environmental requirements were established to ensure that the concentrator would perform properly under normal conditions and survive a relatively harsh loading regime. In so doing, life cycle costs associated with failure and replacement were avoided. The contract defined the following operational and survival constraints:

Temperature:	-26° to +49 °C (-15° to +120 °F)
Wind:	Provide rated output in winds of 6.7 m/s (15 mph) Capable of operation in winds of 13 m/s (30 mph) Survive a 2-second gust in any orientation of 20.7 m/s (46.2 mph) Survive sustained winds while in stow of 36 m/s (80 mph) Survive a 2-second gust while in stow of 42 m/s (95 mph)
Hail:	Resume normal operation after impact from 20-mm (3/4-inch), 0.9 specific gravity hail at velocities of 5 m/s (80 f/s)

The key constraint is the wind loading. Additional loads are described by contract (Ref. 3).

The wind speed was defined; the dynamic pressure was easily determined; but the developed pressure on the concentrator was complex and did not offer a simple solution.

The pressure profile development is a significant assumption in the development of a detailed structural design. The structural weight of a concentrator reflector assembly is as sensitive to the load distribution as it is to the absolute magnitude of forces expressed at some convenient reactive point. Boundary layer, uniform, and aerodynamic profiles were considered in the detailed design development of this concentrator.

The boundary layer profile assumed an exponential profile of wind velocity as a function of distance above grade. This profile was based upon fully developed flow across terrain, and was used to define wind velocities at the concentrator centerline. The profile did not generate the reactive forces at the concentrator vertex developed in wind tunnel research (Ref. 4). Boundary layer assumptions are also unlikely to be a valid representation under gust loadings, as the profile did not have time to fully develop.

TABLE 2.1

OPTICAL CHARACTERISTICS

DIAMETER OF DISH	14 m
GROSS APERTURE AREA	154.0 m^2 •
BLOCKING	5.3%
RIM ANGLE	53.13°
REFLECTIVITY	95%
SLOPE ERROR	3.0 mrad
SPECULARITY ERROR	1.25 mrad
TRACKING ERROR	2.0 mrad
RECEIVER APERTURE RADIUS	.2 m
THERMAL INPUT TO RECEIVER	133 kW
RIM FLUX	52 kW/m^2
OPTICAL EFFICIENCY	89%
COLLECTOR EFFICIENCY	83%

• GORE OUTER EDGE SQUARED

The uniform profile, a constant dynamic pressure over the dish, is a simplified assumption commonly used in concentrator design. This assumption was used in the deflection analysis of this concentrator at operating wind speeds (less than 7 m/s) and as the design case for the survival gust condition (42 m/s). The uniform profile did not generate appropriate moments, a key issue in concentrator design.

The aerodynamic profiles described by Cohen (Ref. 5) were used to generate moment loadings and represented the second survival load case (36 m/s). Under a sustained loading, a pressure profile would develop across the concentrator. The profile was developed from a superposition of a circular flat plate and parabolic airfoil pressure distribution. A third-order polynomial was developed as a function of angle of attack. The development was primarily empirical. The profile is shown in Figure 2.4. The product of the coefficient of pressure (Cp) and effective dynamic pressure (p') produces the pressure loading of a chordal area defined from the leading edge. The dynamic pressure was increased until the third-order polynomial produced moment loadings as described by Roschke (Ref. 4). Drag and lift were slightly under-predicted by this method, but the design to a uniform profile (albeit, noncoincident) was assumed to adequately address lift and drag forces.

2.1.3 Production. The production design provided another essential aspect of the value of the concentrator in that it had a significant influence on cost. Production considerations played an important role in concentrator design and limited potentially costly material scrap losses.

Production rates of both 1,000 and 10,000 units per year are required by the contract. These moderate production levelsrestrict the use of highly automated manufacturing processes associated with mass production. SKI did not assume that all or even a large fraction of the annual production would be installed at a single site. As the solar thermal dish market develops, it is reasonable to assume that many fields will have few dishes. In this respect, the dish construction must require a minimum of site tooling and effort.

Material costs generally represented a higher fraction of the installed cost as production rates rose. Automation and administrative efficiency reduced other expenses at higher volumes. The direct material represented a substantial fraction of the total cost even at moderate levels considered for this concentrator. At annual production rates of 1,000, approximately one-half of the total cost would be material; at 10,000, the ratio would increase to two-thirds. The reflective polymer was the single largest contributor and represents 30 percent of the total material budget.

Emphasis was placed on avoiding large scrap losses for the reflective film, in particular. Scrap losses can vary

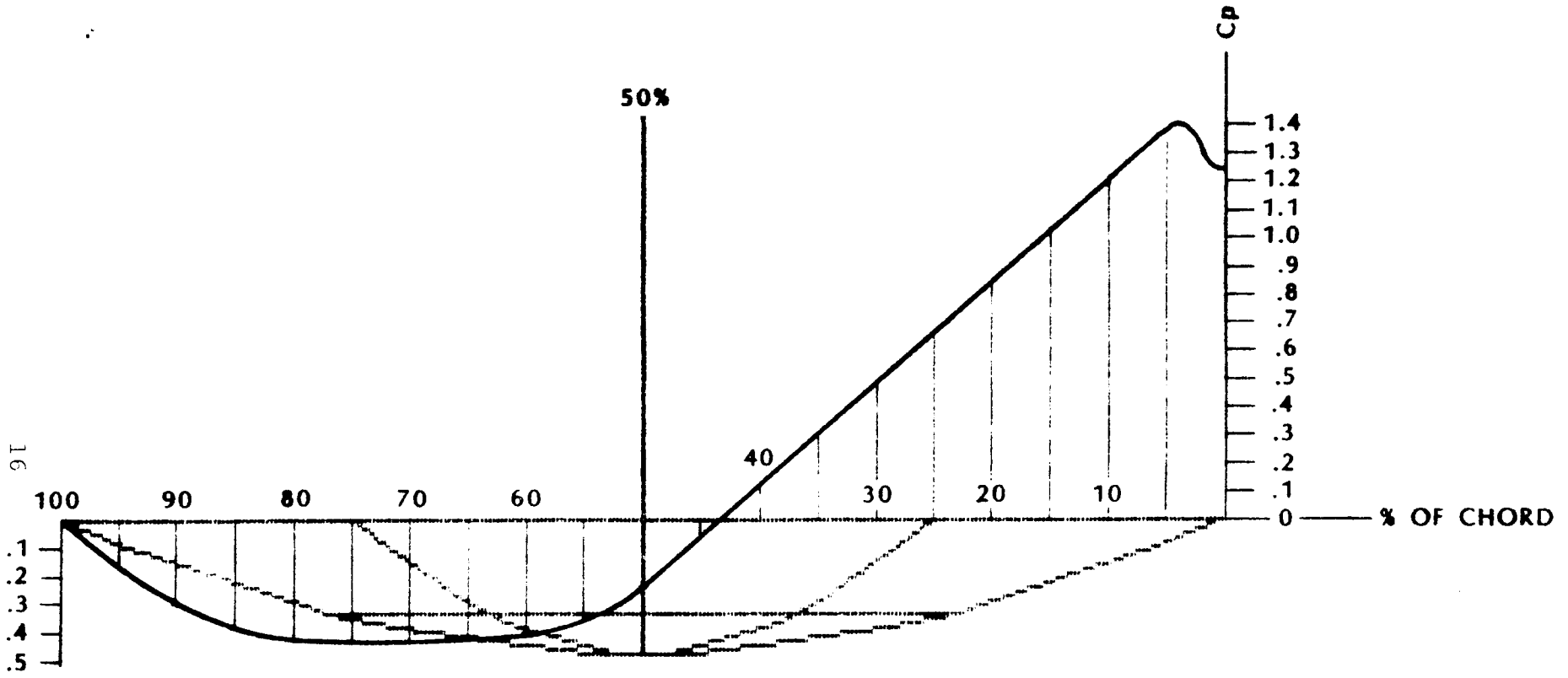

FIG. 2.4 PRESSURE COEFFICIENT VS. PERCENT OF CHORD

FROM: WIND FORCES & PRESSURES
COHEN ET AL ANNALS, NEW YORK
ACADEMY OF SCIENCE
(REF. 4)

substantially according to manufacturing processes and concentrator design. Because of the potential for high scrap loss, material costs were based on the quantity purchased rather than the installed quantity.

The method of fabrication and some aspects of the concentrator design were largely determined by scrap rates. This approach kept scrap loss rate low, at 5 percent.

2.2 Baseline Development

The baseline approach was selected for design of a point-focus concentrator. This baseline design was developed in response to a parametric assessment and application of the concentrator requirements. Modification and optimization are accomplished during a detailed design, but the baseline was retained in essence throughout the development.

2.2.1 Concentrator Configuration. Concentrator design must always accommodate two basic structural criteria: optical accuracy must be provided in the operational regime, and failure must be avoided at the ultimate environmental load condition. Sandwich panel construction, a structure that exhibits a very high specific stiffness (the ratio of stiffness to weight), was selected for the optical petals. This stiffness was further enhanced by joining each panel in a connection capable of load transfer. A reflective surface that acts as a continuous optical element was created as a result of the joint design.

The substantial specific stiffness of the optical element did not imply a large specific strength. If the optical element was forced to act as the load transfer mechanism from the dish perimeter to the drive connection, stress concentration at the root of each panel became large and, ultimately, resulted in buckling failure of the skin. There were 4 basic approaches to improve strength: increase the panel skin thickness, decrease the unsupported skin length, decrease the specific stiffness, or add a secondary load transfer element. The first two options, thickness and length, effectively delayed buckling by increasing the resistance to instability. These options were not pursued due to the basic incompatability of the structural element to accommodate loads close to yield without buckling. Thin flat sheet stock would not provide an efficient material distribution if the structural property required was local section. The third option, reduction in specific stiffness, was not compatible with deflection design. Consequently, a secondary transfer element was defined. Open web beams were selected as the best structural element for a large specific strength.

Coupling between the structures was defined as an issue primarily associated with detailed design. The parametric application of loads and resulting design were accommodated by allocating a portion of the error to each element in the structure. Slope error was assumed to be represented by a linear superposition of panel sag in response to a uniform pressure (6.7 m/s) on an infinitely stiff foundation (Figure 2.5A), and panel sag with a foundation slip and no pressure (Figure 2.5B). This approximation separated the rear structure and optical panel stiffness.

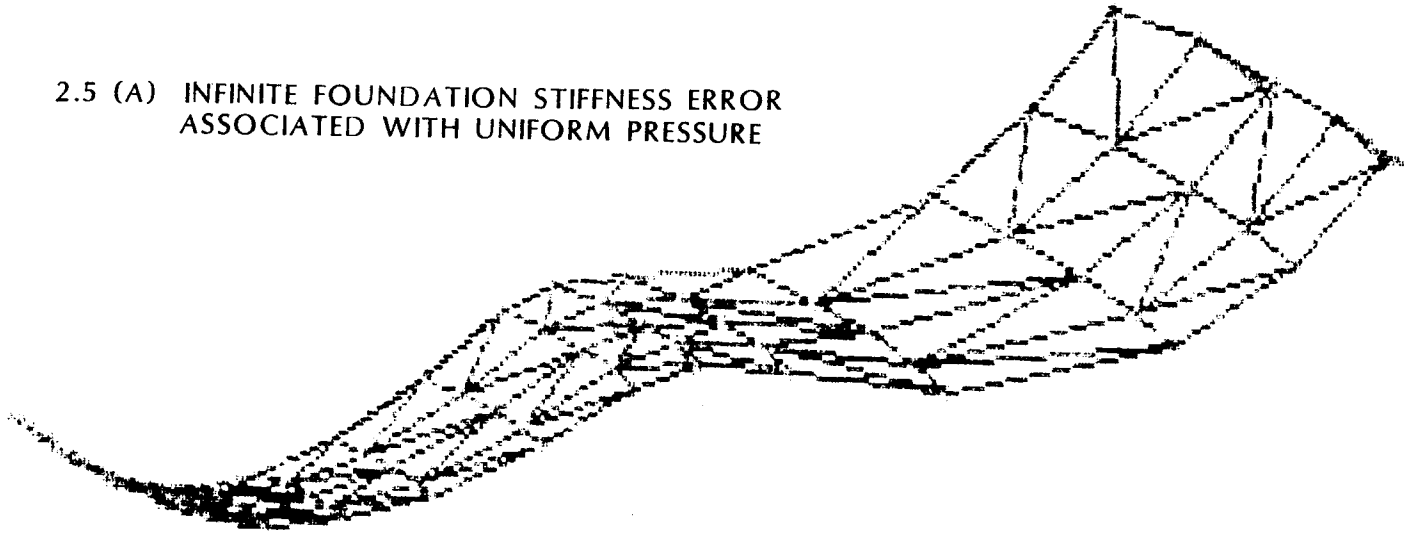

2.5 (A) INFINITE FOUNDATION STIFFNESS ERROR ASSOCIATED WITH UNIFORM PRESSURE

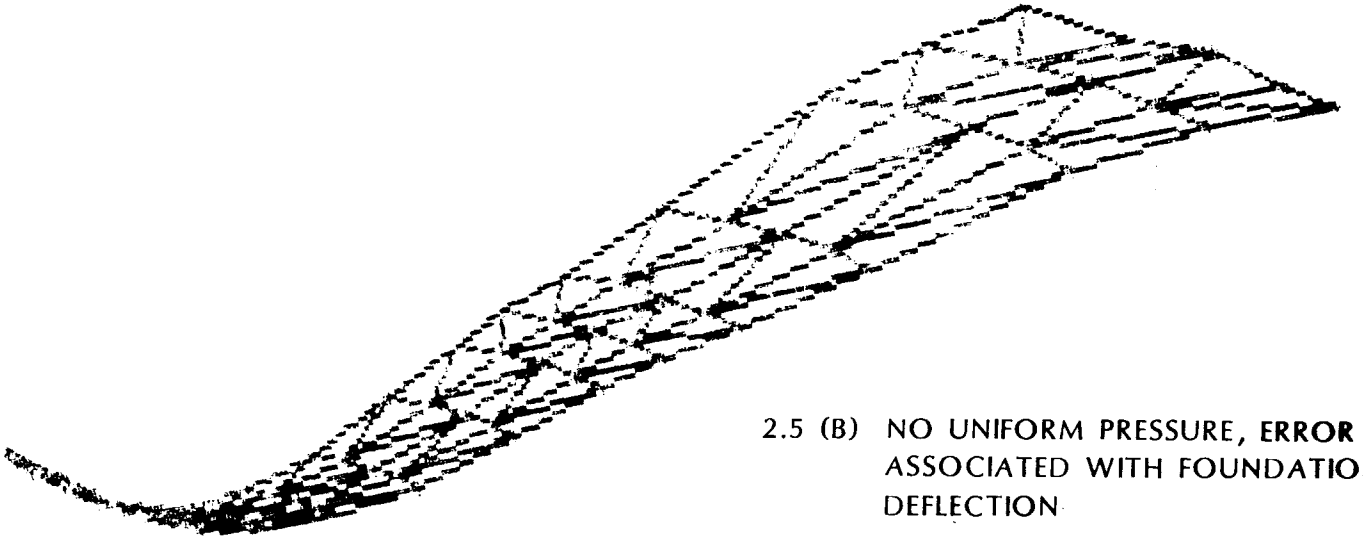

2.5 (B) NO UNIFORM PRESSURE, ERROR ASSOCIATED WITH FOUNDATION DEFLECTION

FIG. 2.5 SLOPE ERROR SUPERPOSITION - PARAMETRIC

A single-tier optical panel, which radiated from the center to the perimeter (see Figure 2.6), was selected for the basic petal design. This approach accommodated the production rate design by reducing scrap loss associated with the outer tier panels. This reduction was important, because the optical element reflective polymer, laminated prior to shear, represented the largest material cost fraction in the concentrator.

Panel width was selected to match the largest sheet stock commerically available.

2.2.2 Parametric Rear Structure Design. The first consideration in parametric rear structure definition was panel span on a rigid foundation (see Figure 2.7A). The figure of merit was the ratio of panel sag slope errors in response to the operational pressure. Equal support span was compared to an equal panel area support (or load). This parametric analysis indicated that the equal span approach to intermediate panel support was superior to constant load. A cursory examination of the circumferential length of the two rings for these cases indicated that the equal span configuration would likely provide the lowest weight. Consequently, an equal span configuration was adopted.

The next step in the parametric configuration analysis was to determine the actual span between intermediate supports. The approach was to assume a discrete number of supports between the concentrator hub and perimeter at equal spacing (see Figure 2.7B). A substantial reduction in error occurred as the number of supports increased. The weight of the rear structure also increased with the number of supports. The absolute magnitude of error was, therefore, used as a figure of merit rather than the ratio of errors. A small panel stiffness was assumed by defining the optical element from a low modulus material (aluminum), 38 mm thick. The results indicated that a slope error of less than 1 mrad occurred with only 2 supports. Consequently, the rear support structure was defined with two rings at equal spans.

The sensitivity of the thickness and modulus assumption was also tested. For panels 25 mm thick, error was doubled; panels 75 mm thick demonstrated errors decreased by a factor of 4. The final panel design fell between the 38-75-mm range and the thickness assumption was assessed to be sensitive, but adequately precise. An increase in modulus (steel panels) also was a sensitive assumption that reinforced the two-ring configuration at all reasonable panel thicknesses.

The final step in parametric rear structure configuration required analysis of the secondary span associated with the circumferential distance between ring support. The number of radial arms defined this distance. Foundation deflection was defined as the figure of merit, and the allowable deflection was

SINGLE TIER APPROACH

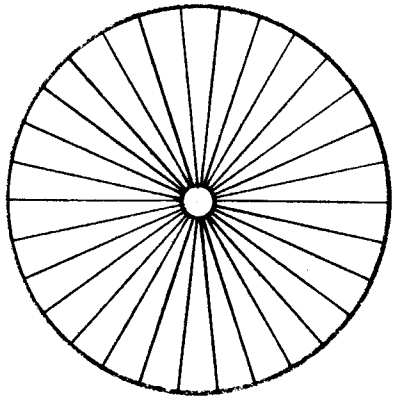

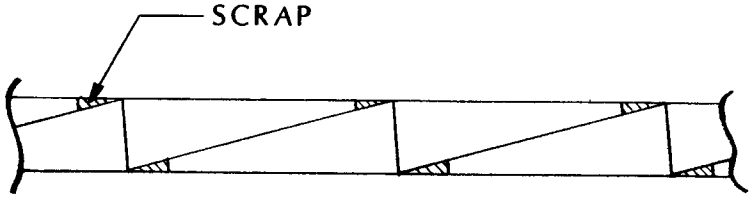

CUTTING PATTERN

5% SCRAP LOSS

TWO TIER APPROACH

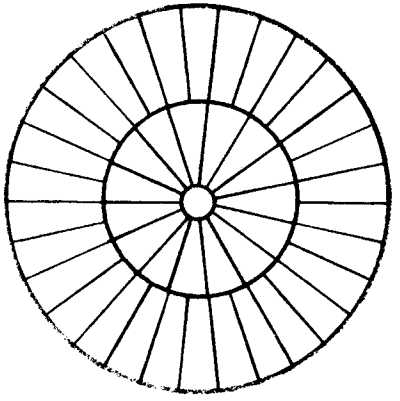

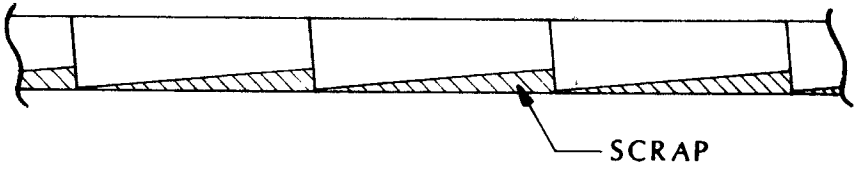

CUTTING PATTERN

20% SCRAP LOSS

FIG. 2.6 SCRAP LOSS COMPARISON

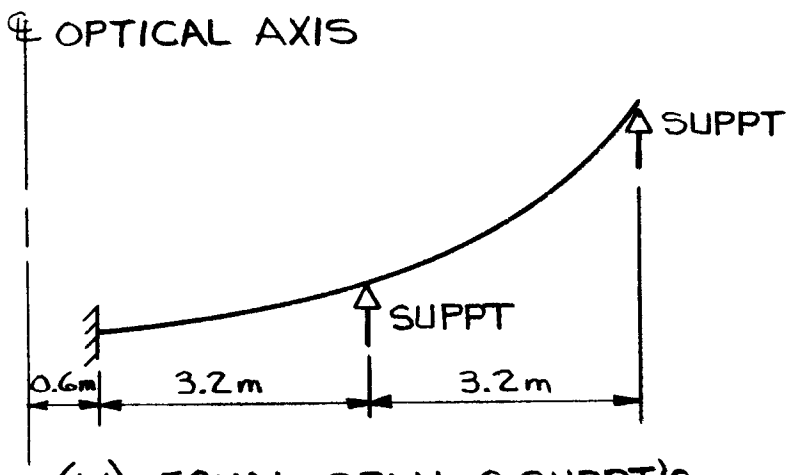

(A1) EQUAL SPAN, 2 SUPPT'S

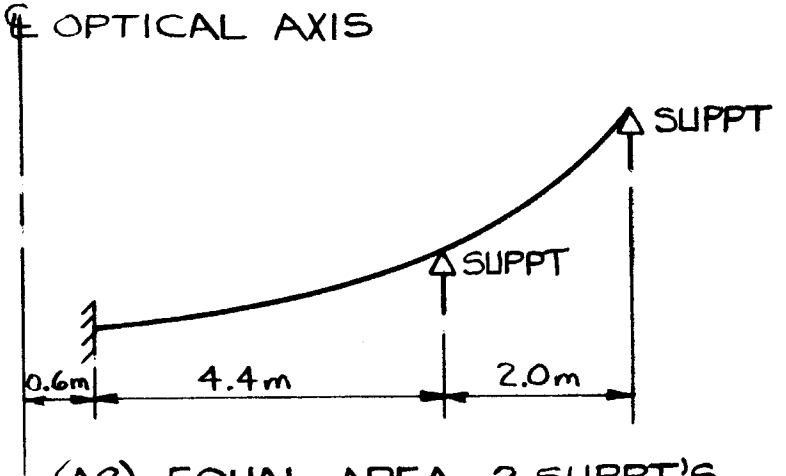

(A2) EQUAL AREA, 2 SUPPT'S

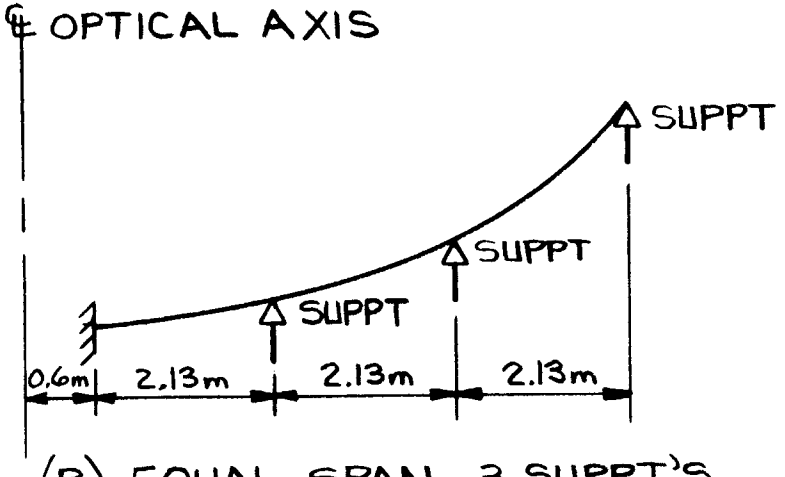

(B) EQUAL SPAN, 3 SUPPT'S

$$\frac{\text{AVG ERROR, EQUAL AREA}}{\text{AVG ERROR, EQUAL SPAN}} = 1.4$$

$$\frac{\text{AVG ERROR, 3 SUPPT'S}}{\text{AVG ERROR, 2 SUPPT'S}} = 3.3$$

SLOPE ERROR, 38 mm AL PANEL

2 SUPPT'S	0.60 mrad
3 SUPPT'S	0.18 mrad

FIG. 2.7 PARAMETRIC ERROR DISTRIBUTION - LOCATION OF SUPPORTS

related to slope error by inducing a fixed deformation in the optical panel with a concentrated load. This allowable deflection was divided into the contribution of arm sag and ring sag in response to a uniform operating load profile. The area moments of ring and radial arms were varied to minimize structural weight. The optical error could not be substantially reduced by increasing ring stiffness (except in the 3 arm case). Panel error induced through arm deflection could be marginally reduced at a fraction of the weight increase required for the same reduction margin in the ring.

The allowable error was defined as 1.25 mrad; 1 mrad of deflection was allowed in the truss, the remainder in the ring. The ring errors were further divided into a radial and tangential component based upon the displacement pattern. Figure 2.8 illustrates the result in specific weight (weight per unit of aperture) for different numbers of radial arm support, the key variable. Six radial arms were selected for the baseline design.

2.2.3 Parametric Panel Design. Parametric panel design required consideration of both error and failure in order to develop a reasonable combination of skin thickness and panel depth. Initially, a panel depth of 66 mm was selected, and the skin thickness was varied to determine the minimum thickness required to resist buckling under a uniform survival dynamic pressure load. The rear structure interaction was neglected by assuming an infinite stiffness. Compressive loads were greatest at the root of the gore. At this point, the unsupported skin had an aspect ratio of 2. The shape configuration was a reasonable approximation of Roark, p. 551, case 26 (Ref. 6) for elastic instability. This approximation was applied to the panel. The result was a skin thickness requirement of 0.6 mm.

Elastic instability was exceptionally sensitive to skin thickness. The allowable or critical stress was proportional to the square of thickness. The actual stress occurred from bending, which was inversely proportional to the square of thickness, and bi-axial or membrane loading, which was inversely proportional to thickness. A fourth-order relationship approximated the relationship for buckling and skin thickness, given a load and panel depth in the range considered.

The panel depth was varied, whereas skin thickness was kept constant at the above value. Two load cases were assumed: uniform survival pressure loads and uniform operating pressure loads. Buckling sensitivity to panel depth was substantially less than sensitivity to changes in skin thickness because the critical load formulation and membrane stresses remained relatively constant. Only the bending stresses increased as panel depth decreased. Consequently, it was not necessary to alter skin thickness in the parametric development for different panel depths. Panel depth design became a function of stiffness

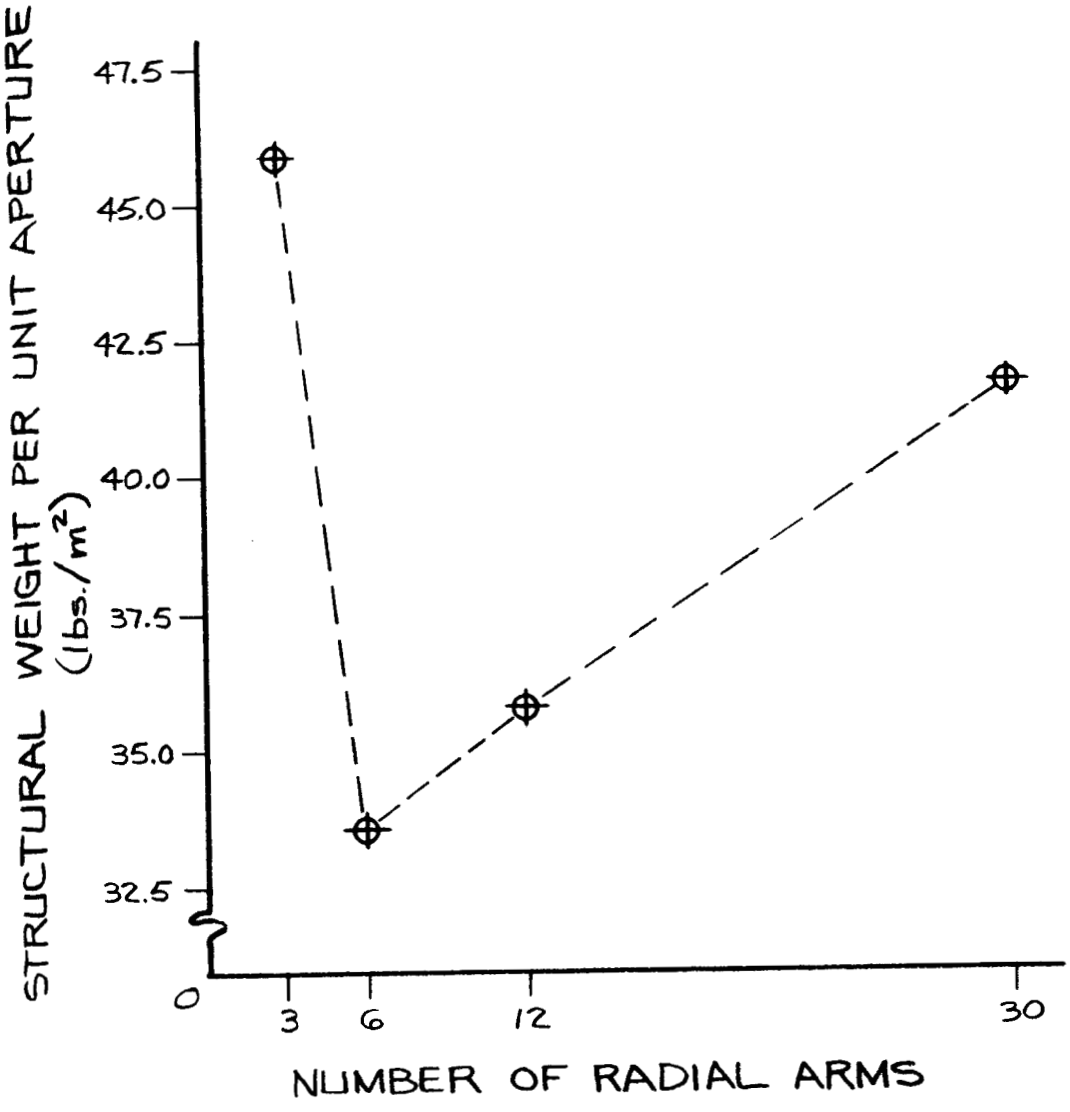

ASSUMPTIONS

1) BEAM WEIGHT/LINEAR FT (lb.) = 0.025 I + 4.7
   WHERE I = AREA MOMENT

2) ALLOWABLE ERRORS
   TRUSS 1.0 mrad
   RING, TANGENTIAL 0.10 mrad
   RING, RADIAL 0.15 mrad

3) OPERATIONAL WIND LOAD (15 mph) SUPERPOSED ON GRAVITY LOAD

4) 2.5 INCH SANDWICH PANEL OPTICAL ELEMENT

5) TWO EQUAL SPAN OPTICAL ELEMENT SUPPORTS

FIG. 2.8 REAR STRUCTURE SPECIFIC WEIGHT VS. NUMBER OF RADIAL ARMS - PARAMETRIC

only. The parametric development indicated a panel depth of 60 to 70 mm which was adequate for slope errors of less than 1 mrad.

The parametric development of panel thickness and skin thickness presented to this point assumed material properties associated with aluminum. The final step required a trade-off between steel and aluminum. Decreases in skin thickness were difficult to accommodate, even when the material modulus increased, because of the buckling sensitivity. Consequently, the only approach for material reduction was to decrease panel depth to accommodate a stiffer material with an equivalent error design.

Approximately 40 percent of the panel material volume was associated with depth (this percentage included corrugated panel, vertical sections, and edge channels), the remaining fraction with skin thickness. Parametric design indicated that 38-mm steel panel depths corresponded in stiffness to an aluminum panel depth of 64 mm. If the 40 percent volume were reduced by the height ratio, the net reduction in steel panel material volume was determined to be 16 percent. The cost of aluminum and steel (assumed at \$0.90/lb and \$0.39/lb, respectively) was converted to a volumetric basis and applied to the material reduction. The result indicated that steel actually cost more than the aluminum on a specific area basis, though the difference was marginal.

Given a relatively equal cost footing, aluminum was selected for optical panel design to decrease the weight loads imparted to the support structure and provide a base material that was insensitive to the corrosive environment.

2.3 Detailed Design Development

The detailed development presented in this section represents the modification and optimization of the baseline design. The analysis reviews sensitive assumptions defined from parametric application of the design requirements and applies requirements in a more rigorous fashion. The reaction of the concentrator to the operational and survival load environment was accomplished primarily through application of linear, finite element analysis. The results of the linear analysis were subsequently reviewed for buckling by definition of the individual element reactions and the application of analytical or empirical approximations.

The load applied to the structure was discussed in previous sections. Three separate cases were used: a uniform pressure at operating wind speeds (6.7 m/s) was used for deflection analysis; a nonuniform profile described by Cohen, (Ref. 5) and a uniform pressure profile associated with survival wind speeds (36 m/s steady, 42 m/s gust) were used for failure analysis. All loading was assumed to be quasi-static. A major departure from the baseline analysis was the consideration of the entire structure with appropriate coupling, rather than an approximated division between the optical element and the secondary load transfer structure. The nonuniform profile and analysis based upon an integrated structure essentially forced the finite element design approach.

2.3.1 Baseline Assumption Refinement. The baseline development, major assumptions, and refinement of sensitive assumptions defined the starting point for the detailed design. These assumptions were divided into three major sections: geometric configuration, rear structure, and optical panel design.

The baseline geometric configuration of the concentrator assumed a basic shape. Gores or petals radiated from the hub to the perimeter in one continuous panel to reduce scrap. The optical panel was defined as a sandwich plate on the basic specific stiffness performance of the shape. This stiffness was subsequently enhanced by attaching petals through a load bearing joint to force the optical element to act as a continuous plate. A secondary rear structure was added to transfer survival loads to the drive. These assumptions were critical to the baseline and were considered in the detailed development.

The approach to model development was iterative, effectively assuming the final shape to determine the appropriate component relationships. The approach of baseline development was exploited to full advantage. The entire concentrator was modeled as a 180° segment, with appropriate boundary conditions. This model could accommodate the nonuniform profile, which has a

single axis of symmetry. Loads were applied to the optical element and rear structure to determine the effective spring stiffness of each component. The optical and support components could then be separated, and the interaction could be modeled with springs. In order to model the impact of rear structure changes on the optical panel, the ratio of spring constants was assumed to remain constant, while the values changed. This assumption essentially tied the relative stiffness of the rear structure to its span. Subsequent development work with the complete model indicated that the exact ratio of spring constants at the middle and outer ring was not particularly sensitive to the final development.

A fraction of the baseline optical assembly was modeled and the rear structure was simulated at the attachment points with springs, rather than an infinitely stiff foundation. The ratio of critical and actual panel compressive stress (safety factor, buckling) was plotted as a function of rear stiffness for a uniform survival load in Figure 2.9. The relationship indicated that at zero attachment stiffness, corresponding to no rear structure, failure would occur because of the enormous load concentration at the root of the panel.

This stress concentration cannot be effectively eliminated with sandwich panel construction. The stress from the entire concentrator aperture is ultimately concentrated at a radius of less than 1 m. Effective load transfer would require order of magnitude increases in panel depth and introduce secondary instability problems in the core. The highly concentrated load would also require substantially greater skin thicknesses to avoid localized buckling. No weight-effective options were available to reduce this failure mechanism other than the addition of supplemental load take-off points.

Two similar optical assembly models were constructed, with boundary conditions modified to represent a continuous optical element and 30 discrete panel elements. The rear structure was again simulated with inner and outer springs of constant ratio, and a uniform operating pressure load was applied. The results are presented in Figure 2.1 as an area weighted slope error versus the support structure stiffness.

The constant slope error essentially indicated that the major error contribution occurred from the sag between supports. The rear support structure simply forced the error to zero near the gore midpoint. The figure had an important corollary: the optical panel stiffness determined the concentrator accuracy. Slope error was not sensitive to foundation deflection, so long as some foundation was provided. This result represented a substantial departure from the baseline design. Two major conclusions were drawn. First, sandwich panel construction was appropriate for this point-focus concentrator because bending stiffness in the optical element ultimately determined accuracy. Second, rear structure design was based upon survival

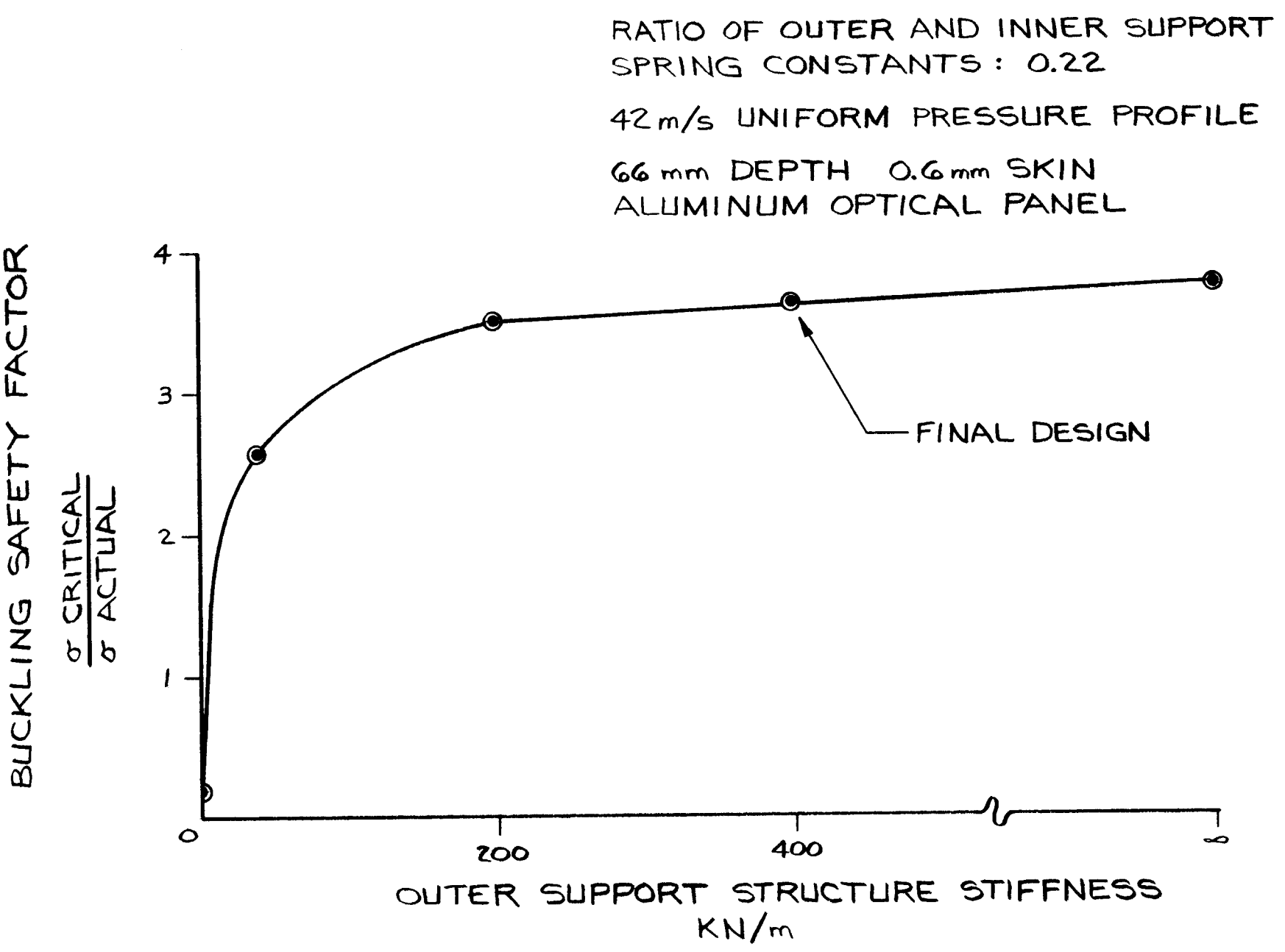

FIG. 2.9 BUCKLING AND SUPPORT STRUCTURE STIFFNESS

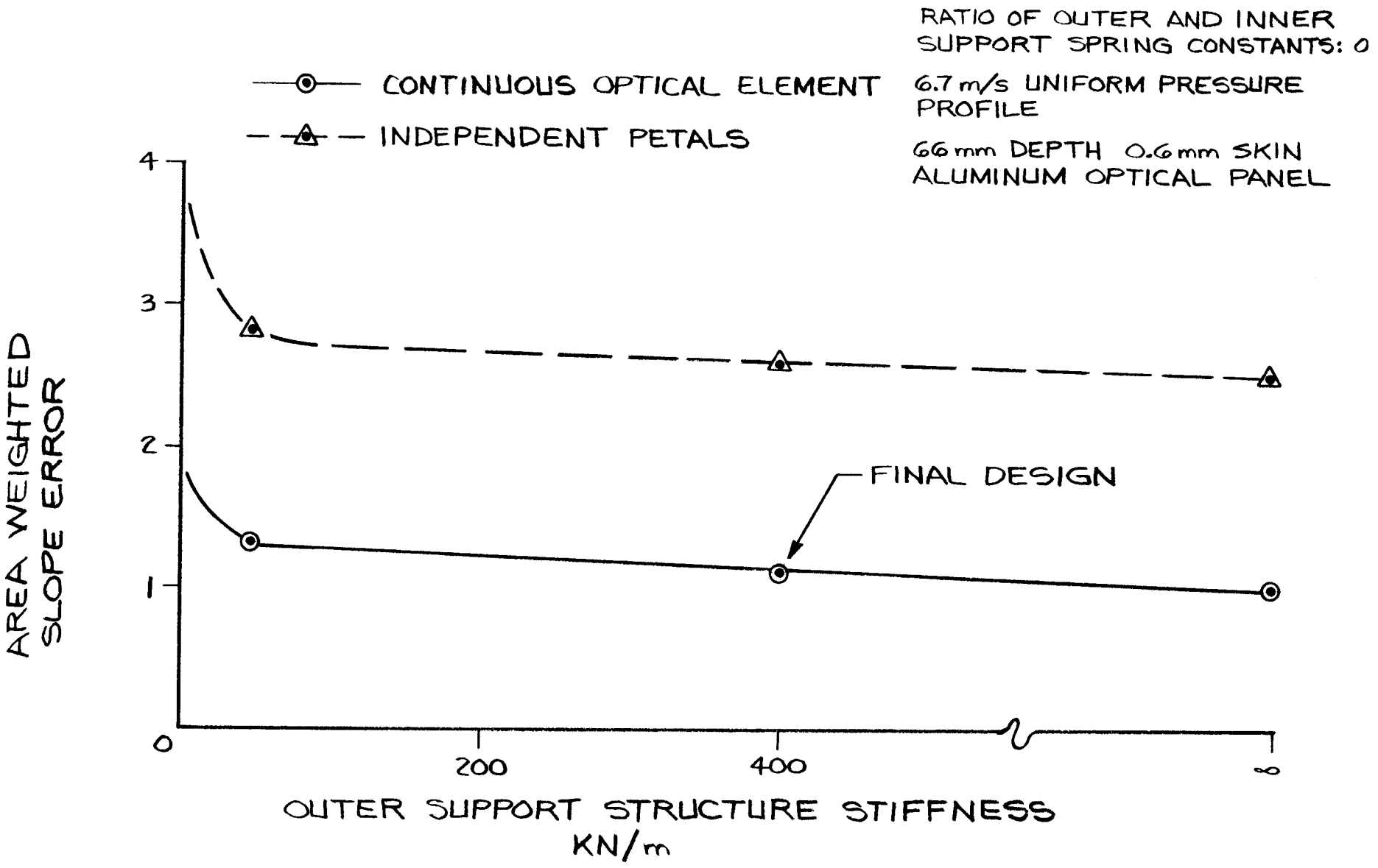

FIG. 2.10 SLOPE ERROR AND SUPPORT STIFFNESS FOR A CONTINUOUS AND DISCONTINUOUS OPTICAL ELEMENT

considerations only; stiffness was required only to prevent optical panel failure and did not substantially influence performance.

Optical accuracy is substantially different for continuous and discontinuous reflective assemblies. The slope error was already defined as a function of optical element bending stiffness. This stiffness would obviously be increased if each petal were connected with a load transfer joint. For the final design, the area weighted slope error in the continuous panel was 1.2 mrad in an operational wind. The slope error would increase to 2.7 mrad in a discontinuous assembly. Consequently, the baseline design assumption of a continuous optical panel was adopted.

The rear structure was defined as six radial arms with two load take off points or rings. Final design development did not attempt to modify or optimize this assumption, because the assumption was not particularly sensitive. The final rear structural weight (5800 lbs less 900 lbs for PCA supports, 4900 lbs) was compared to the weights developed at parametric application (see Figure 2.8, previous section). The parametric assumption was within 5 percent of the final design development.

The panel design developed in the parametric analysis was defined from aluminum with a depth of 66 mm and a skin thickness of 0.6 mm. The panel depth was not a sensitive assumption and was not modified in the final design development. Skin thickness, however, was very sensitive to panel weight and buckling failure. A model approach, similar to those described previously, was defined: a small fraction of the concentrator was modeled with rear structure interaction defined by constant ratio springs at the load take-off points. A uniform survival pressure load was applied, and skin thickness was varied. The result of the analysis is plotted in Figure 2.11. The parametirc assumption for skin thickness, 0.6 mm, represented a critical-to-allowable stress ratio of approximately four. Later applications of nonuniform profiles reduced the safety factor to three. Parametric assumptions regarding panel skin thickness were adopted for detailed design.

The selection of optical panel material was not sensitive in parametric development, though the selection does seem paramount to final design. The major concern was over potential softening of the rear structure due to the hinge connection between optical and structural elements. Consequently, the design was altered to remove the hinged connection and replace it with a solid connection to test the assumption. The result of this test indicated that rear structure stress was marginally reduced by providing the hinged connection. This result is typical in any structure designed to stress rather than to deflection criteria: as the number of restraints decreases, stress will decrease and deflection will increase. The hinge was judged to have a minimal impact upon the structural weight design.

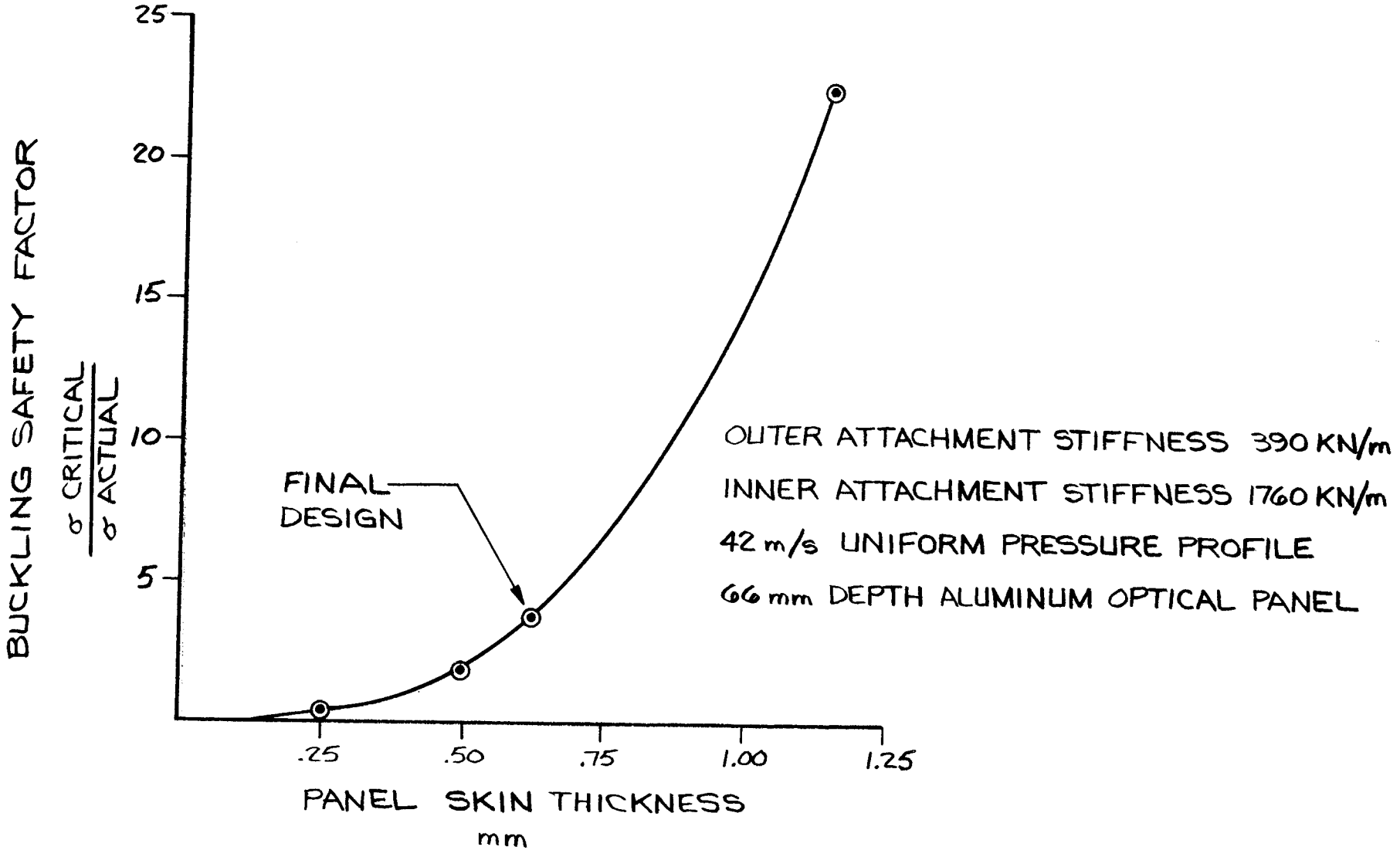

FIG. 2.11 BUCKLING AND PANEL SKIN THICKNESS

2.3.2 Final Model Development. The final model development included a 180° model of the optical panels and rear structure. This dish fraction was selected as the nonuniform profile because the nonuniform profile demonstrated a single line of symmetry. Connection between the two structural components was implemented through a hinge. The two survival load conditions were imposed, and the properties of the rear structure components were defined in response to the bending moments. Receiver strut analysis was performed in a separate modeling effort (see Section 2.4); the reactions from this model were imposed as concentrated loads at the connection point. The deflected pattern is shown in representative form in Figure 2.12.

The radial arms were subject to moment loadings both in and out of plane. The out-of-plane loading was most severe. The in plane loadings were actually caused by the resistance to rigid body motion of the concentrator itself. The nonuniform profile was essentially attempting to push the concentrator downstream. Resistance to the motion was developed in the arms that ran parallel to the wind direction. The nonuniform profile was the worst load case for the truss in both directions. In the out-of-plane direction, the windward truss saw a greater load than any other truss in the structure.

The rings were also subject to moment loadings in both directions. Out-of-plane moments were defined by truss deflection at the point of connection and the normal component of the wind load imparted through the hinge connection. The nonuniform pressure profile created the most severe loading condition in the out-of-plane direction on the windward side of the concentrator. The planar loading was created primarily by the truss deflection. This load is intuitively described by the deflection pattern shown in Figure 2.12. As the truss deflected, the ring had to assume a new circumferential length. Consequently, careful attention was given to the balance of stiffness in the two elements to avoid introduction of ring stress without a compensatory stress reduction in some other structural component.

The final step was to consider the restraint in the nonhinged direction of the optical-to-structural joint. This connection was softened in the lateral direction to avoid imparting a large moment loading into the concentrator surface and at a localized point in the ring itself.

The result of the design analysis was definition of supports that were able to carry the out-of-plane and in-plane loadings by providing area moment properties in two directions. The box truss was selected to achieve this purpose. The moments of inertia provided in each section are listed below:

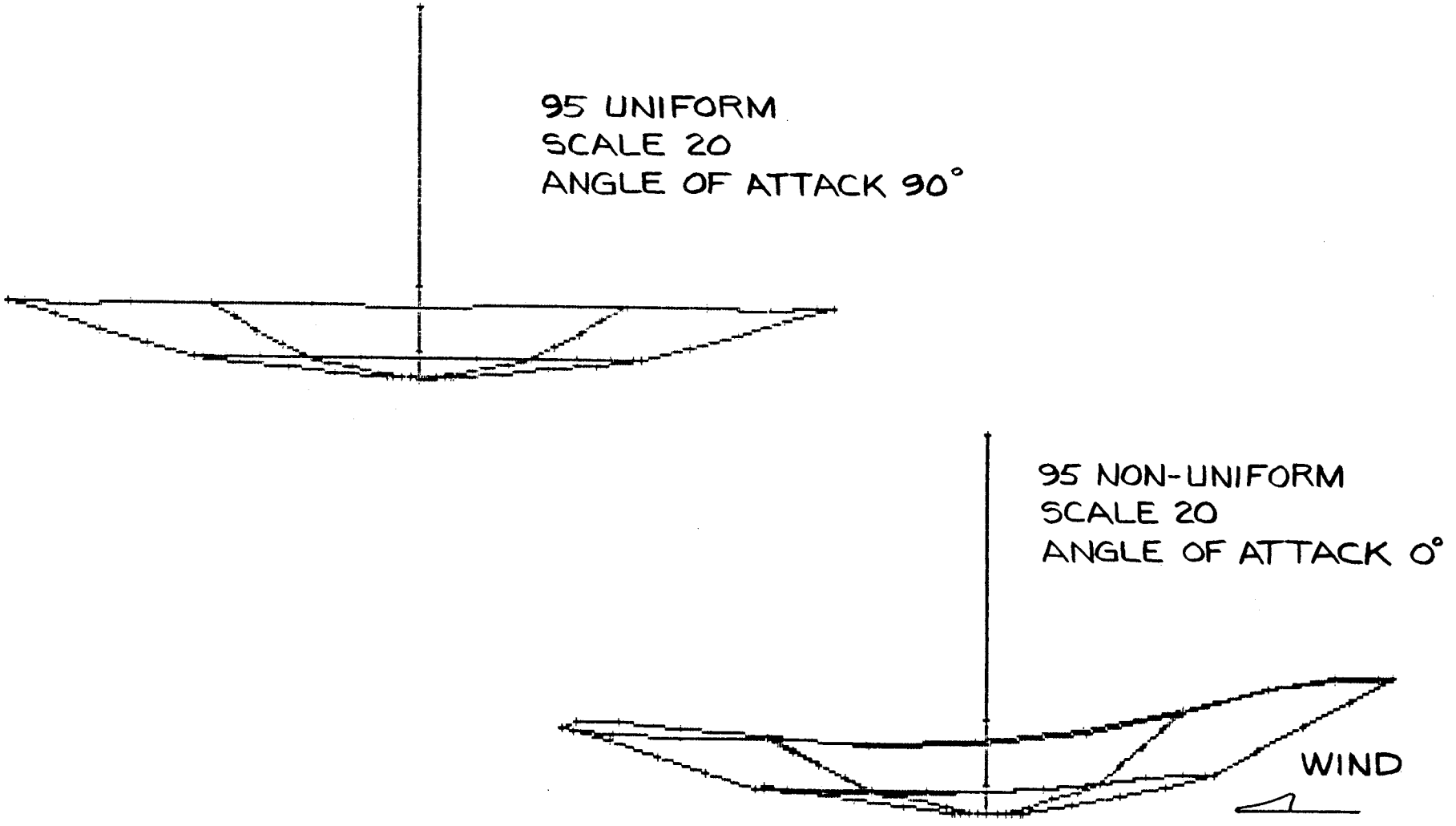

FIG. 2.12A WIND LOAD DEFLECTIONS UNIFORM AND NON-UNIFORM PROFILES SIDE VIEW

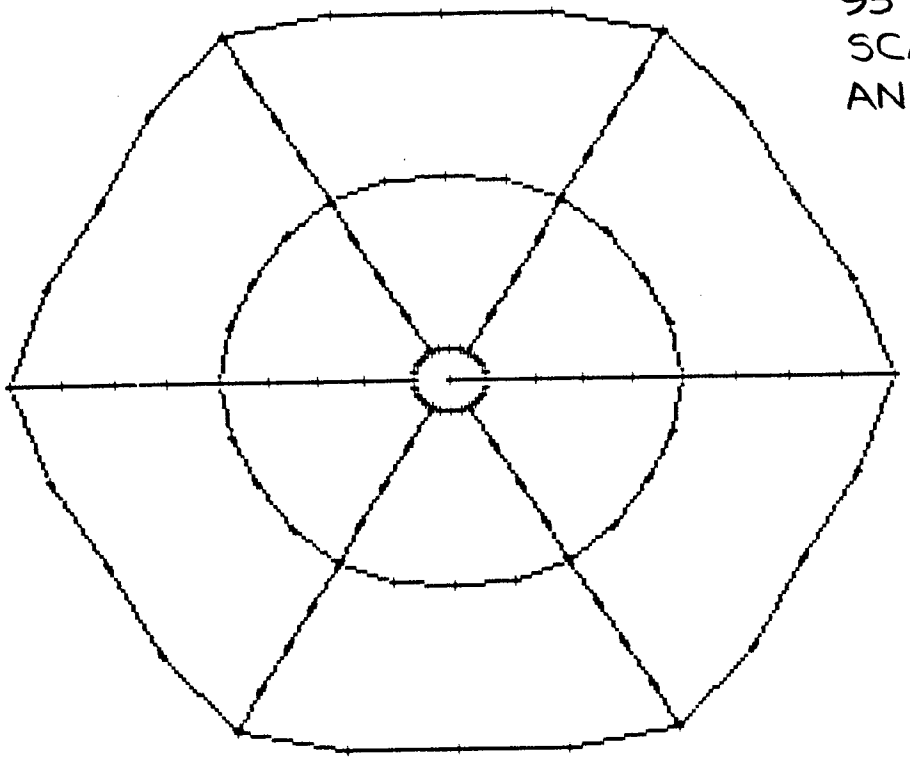

95 UNIFORM
SCALE 100
ANGLE OF ATTACK 90°

95 NON-UNIF.
SCALE 100
ANGLE OF
ATTACK 0°

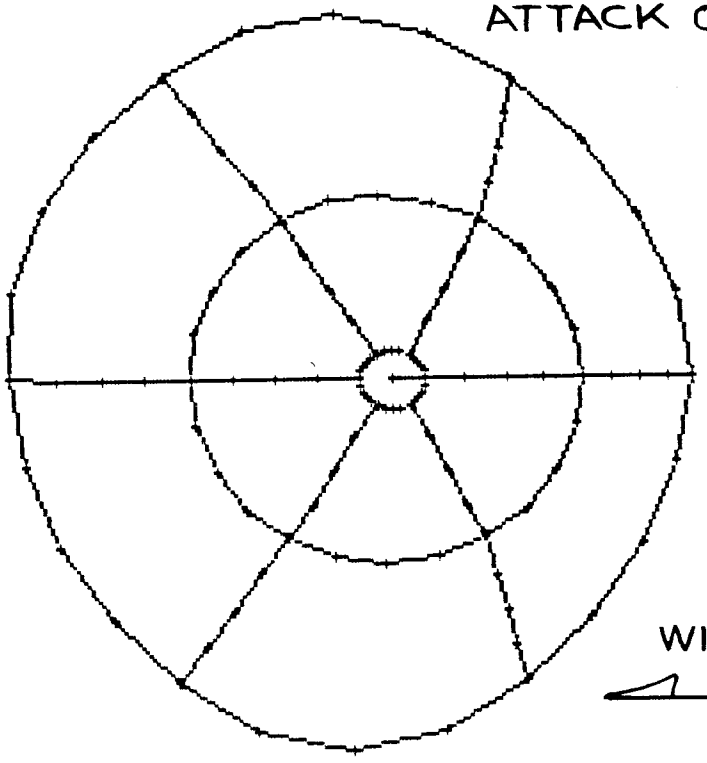

WIND

FIG. 2.12B WIND LOAD DEFLECTIONS UNIFORM AND NON-UNIFORM PROFILES TOP VIEW

Radial arm, out-of-plane moment of inertia	2.01E-4 m^4
In-plane	4.23E-5 m^4
Middle ring, out-of-plane	1.87E-5 m^4
In-plane	1.01E-5 m^4
Outer ring, out-of-plane	3.01E-5 m^4
In-plane	1.87E-5 m^4

The structural weight of the rear structure was determined to be approximately 4900 lbs, including all elements required for load transmission, except the PCA support assembly defined in the following section. The optical element weight was determined to be 3000 lbs. Subsequent development of the PCA supports defined weight at 900 lbs, bringing the total concentrator weight to 8800 lbs.

2.4 Retractable Support for the Power Conversion Assembly

The power conversion assembly (PCA) is a costly component of a concentrator and is susceptible to damage from concentrated solar flux. It can quickly overheat in the event of loss of power or other failure that stops fluid flow. Conventional protection schemes require actively cooled shutters to block the solar energy or auxiliary power units with quick response to drive the dish off-axis. SKI developed a protection system as part of the concentrator structure that was passive. It did not require an external energy source for pumps or drives.

The system used the potential energy of the PCA weight to drive it out of focus. Upon command, or the loss of power, the PCA support retracted and the PCA moved away from the concentrated flux. This retractable system could also be used to lower the PCA for easy maintenance access. This section describes the operation and design of this system.

2.4.1 Description of the Support for the PCA. The PCA support consisted of three struts and a circular mounting ring. The ring provided a structural interface between the PCA and the struts. The three struts were attached to the ring on equal spacing and radiated down to the concentrator support structure. They were attached to the trusses close to the connection between the truss and the intermediate ring. The system retracted by allowing one strut to slide through its attachment at the truss. The two passive struts were hinged at their bases to allow the PCA to pivot away from the focus (Figure 2.13). During normal operation, the retractable strut was fully extended. Loss of power would release the strut and allow the PCA weight to force retraction. In this mode, the strut would retract only enough to move the PCA safely away from the focus. An operator could lower it beyond this point for PCA maintenance.

The passive struts were pinned about a common axis at their base and rigidly attached to the mounting ring at the top. The retractable strut was pinned at the ring and attached to the truss through a sleeve unit (Figure 2.14). This sleeve guided the strut as it was lowered and pivoted to accommodate the resulting rotation.

Compressive loads were carried from the strut through a rack-and-pinion system. The pinion was connected to a motor and brake unit as shown in Figure 2.15. This system had three functions. First, it held the PCA rigidly in place during normal operation and released it when power was lost. The motion during emergency defocus was slowed and dampened by a shock absorber mounted in the sleeve assembly. Second, the motor unit was back-driven when the PCA was lowered for maintenance to slow the rate of descent.

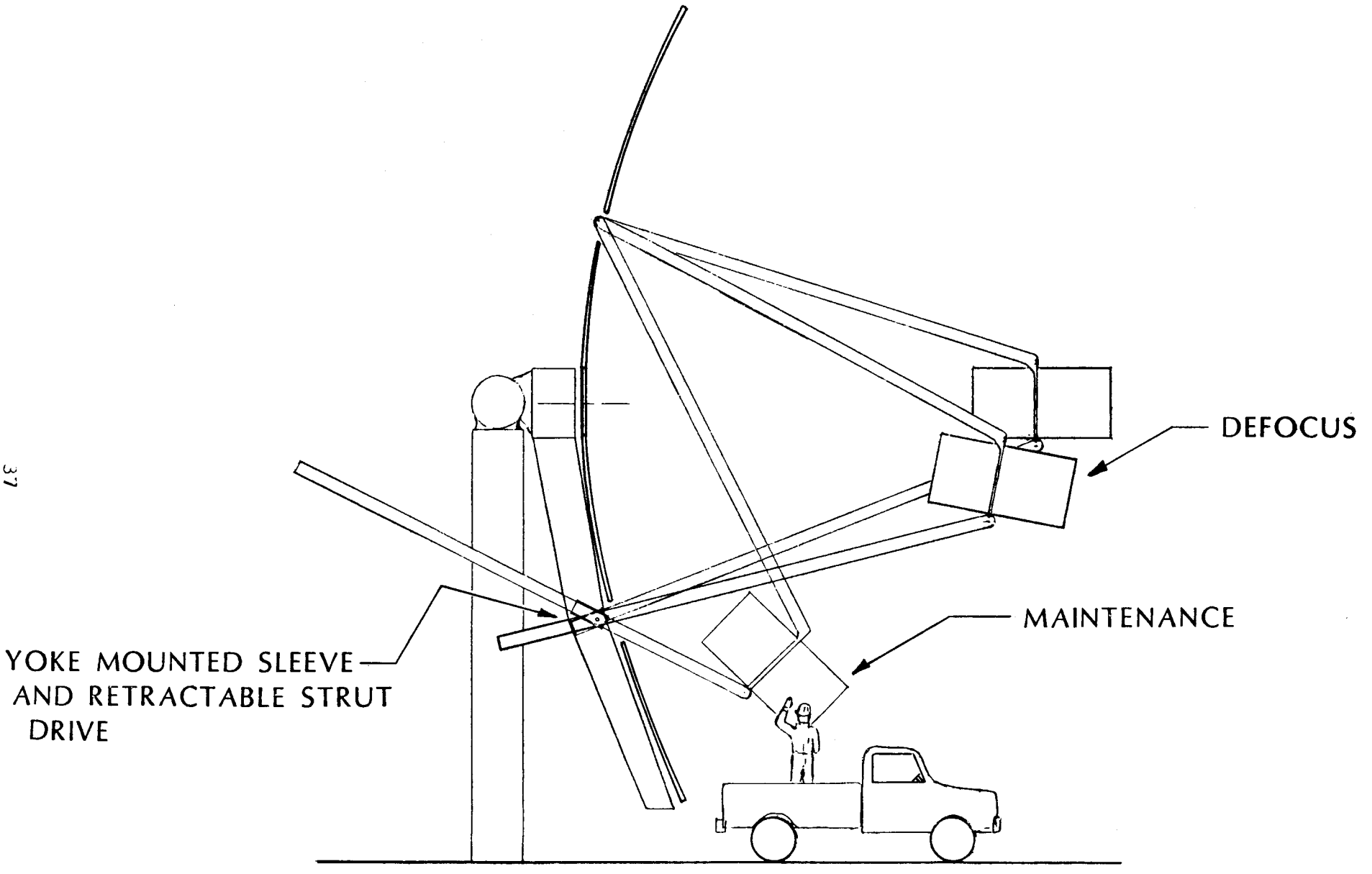

FIG. 2.13 RETRACTABLE PCA SUPPORT

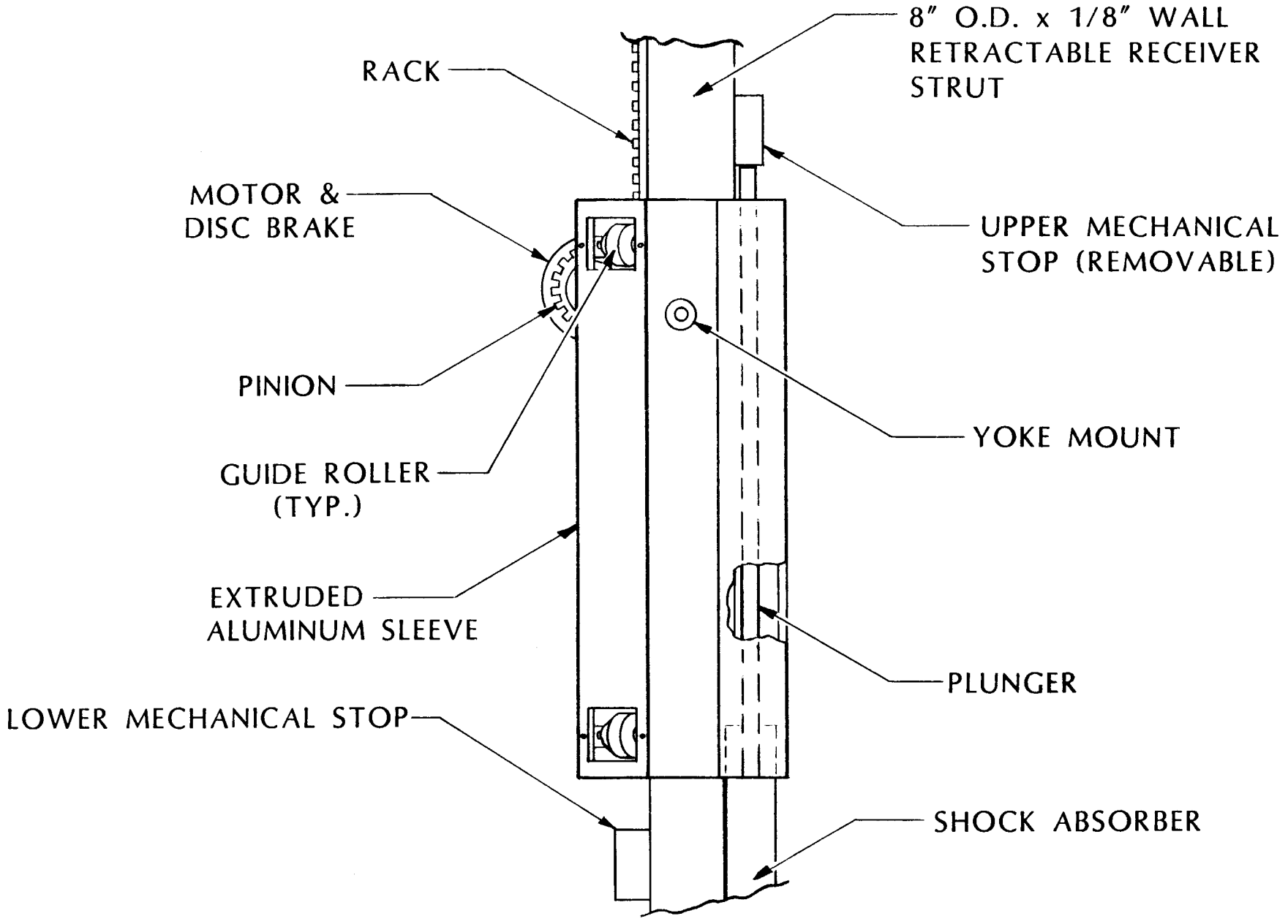

FIG. 2.14 RETRACTABLE STRUT SLEEVE SIDE VIEW

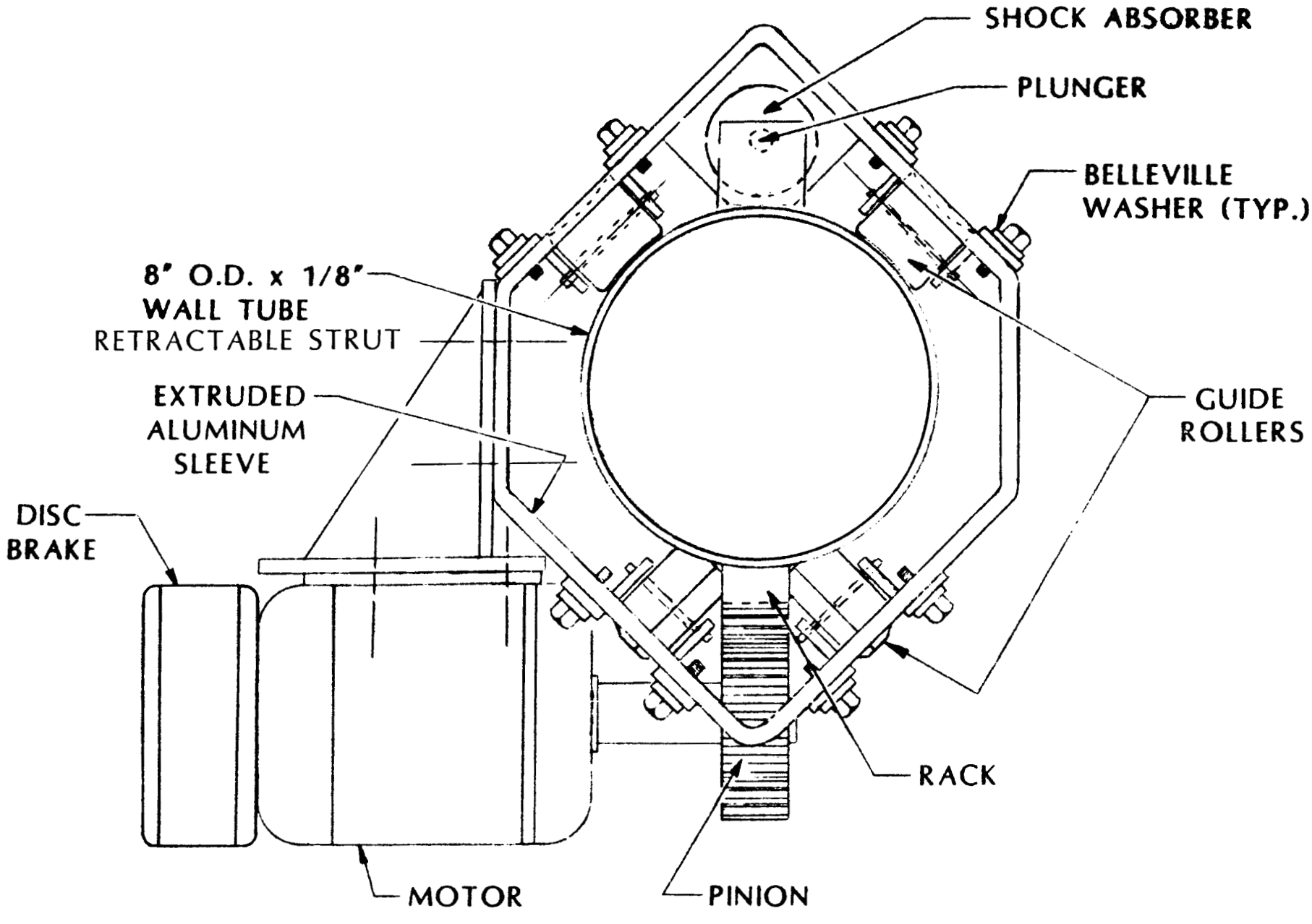

FIG. 2.15 RETRACTABLE STRUT SLEEVE TOP VIEW

Third it drove the strut back to the operational position. The drive rate was much slower than the emergency drop rate and was not intended for walk-on purposes. An excessively large drive would be required to achieve walk-on speeds.

The PCA was placed in the defocus position when the concentrator was stowed to avoid damaging the unit with concentrated sunlight. The PCA could intercept concentrated light if the dish remained stowed on a sunny day with the PCA at the target. When the sun approached the zenith, a hot spot, or area of concentrated energy, approached the target and could have damaged the outer portion of the PCA. The PCA was moved away from the path of the hot spot by moving it toward the south. For dishes located at latitudes well below the declination, it may be appropriate to increase this effect by stowing the concentrator canted slightly to the north.

2.4.2. Stow Orientation. The PCA imparted a significant weight load on the struts and the dish, and influenced the stow orientation. The design load supplied for the receiver was 2000 lbs, roughly 20 percent of the concentrator weight. Its weight was more significant than that of the concentrator because of the high moment that was created due to its distance from other components.

The PCA induced moment load was removed by stowing the dish facing the zenith. The weight was near center above the supports and the struts shared the compressive loads. Wind loading of the structure in a zenith stow imposed a large nonuniform pressure profile across the dish and induced large moments in the structure.

By stowing toward the horizon, the wind load profile differed but there remained a large overturning moment. In some orientations, this load would sum with the moment created by the PCA. The wind loadings of these two cases were roughly equal in that they induced similar maximum loads in the structure. The addition of the large PCA moment in the horizon stow made this approach less desirable. On this basis, the stow position was defined to be toward the zenith.

2.4.3 Support Analysis for the PCA. Shock loading the PCA during emergency defocus was avoided by contouring its acceleration curve. Initial acceleration was due to gravity and resulted in a smooth increase in speed. This motion was unrestricted for a third of its travel. The velocity continued to increase until contact with the shock absorber. The resistance from the shock absorber was proportional to the square of the velocity. This resistance opposed and overcame the force of gravity and decelerated the PCA for the remainder of its

travel until it came to rest on mechanical stops. Shock loadings upon impact with the shock absorber and impact with the stops were avoided by mechanical cushioning. Springs provided this cushioning by isolating the damping mechanism from the structure.

The retractable strut had to be in compression in all dish orientations in order for the gravitational potential energy to provide emergency power. An azimuth/elevation drive (for which this concentrator was adaptable) could ensure large compressive loads in the retractable strut for most orientations by keeping the strut on the lower side of the dish. The compressive load was reduced when the concentrator was pointed toward the zenith. The compressive load was further reduced in the over-the-shoulder orientation. This lowered the rate of defocus but it remained acceptable. The defocus travel time for the extreme case of Hawaii on the summer soltice would be 4 seconds. The quickest defocus occurred when pointed at the horizon which was 2.5 seconds.

The PCA support structure was sized through finite element and analytical analysis. The finite element analysis resolved the stresses from the applied loads. Buckling stability was then defined analytically. Two cases were considered to represent the worst loading environment for this structure: a 42 m/s stow case in which the receiver wind loads were substantial, but the weight loads were evenly distributed, and a 21 m/s case while facing the horizon in which the wind loads were moderate and the weight loads were high.

The struts acted as long, slender columns and would buckle before their material limits were reached. The analytical approach to define buckling safety considered eccentric loading. Wind and weight loads were imposed on a finite element model of the struts and support ring. The reactions at the strut tips were established. These moments and forces were used to establish the required strut properties.

The buckling limit is a strong function of modulus of elasticity and area moment of inertia. High values for both of these variables is desirable. Steel was chosen as the material of choice because of its high modulus, three times that of aluminum. A circular tube was chosen to maximize the moment of inertia in any direction. The columns tended to buckle about the axis with the lowest moment of inertia and required equal properties about the two transverse axes. A 200-mm diameter steel tube with a 4-mm wall was defined as the best candidate to meet the buckling requirements.

The PCA support structure was not extremely stiff and had a relatively low natural frequency. The finite element model was used to define the natural frequency to determine if the wind would excite the structure. The model assumed the receiver to be a lumped mass and the struts were modeled as a series of masses. Two dominant vibration modes were found. The bending mode had

the lowest natural frequency. This mode caused the struts to bend to accommodate the rocking of the PCA. The natural frequency was 2 Hz. Twisting of the entire structure had a frequency of 3 Hz. This mode caused the PCA to twist about the dish axis. These frequencies were above the dominant natural frequency of the wind and were not expected to be excited by the wind.

2.5 CONCLUSION

The concentrator developed in Phase I was based upon requirements defined to improve performance and reduce life-cycle costs for point-focus technology. The performance design was defined within the limitations of available materials. Optical errors, a particularly sensitive performance issue, were constantly reviewed during the development process. Production rate limitations were essentially imposed upon the design by consideration of the purchased material weight and, in the case of reflective film, the area. The load environment is a very sensitive definition on the final material cost of a concentrator and was the focus of parametric and detailed design efforts. Wind is the dominant load in concentrator design. Wind velocities suitable for operation and survival were specified; the application of these wind loads to the concentrator was defined within the development effort.

A baseline design was developed through parametric application of the design requirements. This approach required definition of a design that was subsequently modified to determine the sensitivity of assumptions. The detailed design development relied upon an iterative approach: the baseline design was modeled to determine the fundamental relationship of components in the overall design; the assumptions associated with configuration or component design were tested; and the baseline design was modified to reflect the results of the analysis. Component relationship was defined again, and the process was repeated until no major changes in the basic design occurred.

The final design was developed based upon a combined finite element analysis model, which incorporated the optical element and supporting structure to allow for coupling within the two structures. Several key features of the design were

* Accuracy was primarily dependent upon the stiffness of the optical panel. The rear structure was required for accuracy, though structural stiffness was not defined by deflection requirements.

* Slope error could be reduced by a factor of 2 or more by forcing the optical element to act as a continuous section.

* The rear structure was required to eliminate panel failure in survival conditions. The rear structure design was largely based upon its own stress condition.

* The stress in all elements could be reduced by eliminating restraints that were not required for optical accuracy.

An innovative technique for PCA protection was also defined in the design development. The receiver struts were hinged. In an emergency, one strut would partially collapse, bringing the PCA out of focal point. The strut could be manually driven to a point that allowed engine maintenance near ground level.

The design development of this concentrator projected a high performance (89 percent optical, 83 percent thermal, 800 °C) in a structurally efficient package (59 lb/m^2 reflective assembly weight).

3.0 MANUFACTURING, CONSTRUCTION AND COSTS

This section presents the manufacturing process, on-site construction, and concentrator cost for producing the point-focus concentrator. This task was completed under Phase I of Sandia National Laboratories' Point-Focus Concentrator contract. The objective of the contract was the development of the reflector assembly and support structure and did not include the balance of the dish(pedestal, drive, controls, etc.). For this reason, the balance of dish has not been addressed.

Manufacturing all the components was done at a central plant. On-site activities were restricted to assembly and alignment, and the use of complex tooling in the field was avoided. The concentrator could be effectively installed in small or large quantities per site.

Reflector assembly costs were estimated to be $\$77.68/m^2$ at 10,000 units per year and $\$107.78/m^2$ at 1,000 units per year.

3.1 Manufacturing

Manufacturing concerns played important roles in the concentrator design. Scrap loss, tooling cost, labor requirements, and production rates influenced the final design and cost development. Each step of the design included a review of manufacturing processes in an effort to use common industrial techniques where practical and develop new techniques where necessary. These efforts are described in this section.

3.1.1 Optical Element Components. The optical element components included those parts required to fabricate a petal or gore. Each petal was fabricated from three basic parts: skins, core, and edge channels. The relationship of these parts is shown in Figure 3.1.

Coil line processes were identified as appropriate technology for the production rates associated with this design. These line processes are widely used in the sheet metal industry because they efficiently accommodate the raw material stock. All optical element components were fabricated from flat sheet stock on a continuous coil line.

Figure 3.2 illustrates the line required for fabrication of the reflective skin. The 0.6-mm by 1.5-m aluminum sheet was initially leveled and cleaned. A reflective polymer was laminated to this base stock, and the material was cut with a numerically controlled laser to the petal shape. The polymer reflector and aluminum base stock had different coefficients of thermal and hygroscopic expansion. Consequently, free edges had

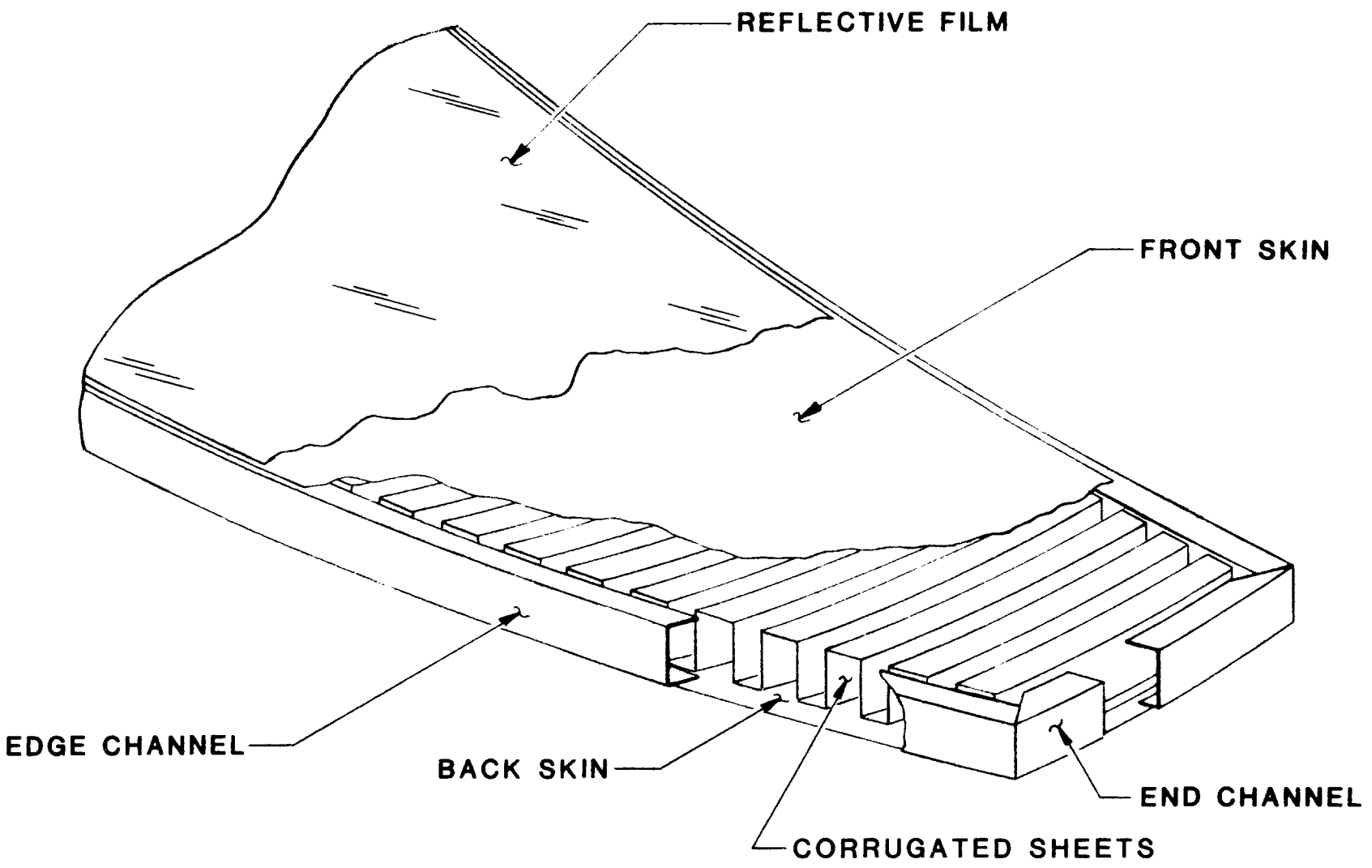

FIG. 3.1 COMMERCIAL OPTICAL FACET

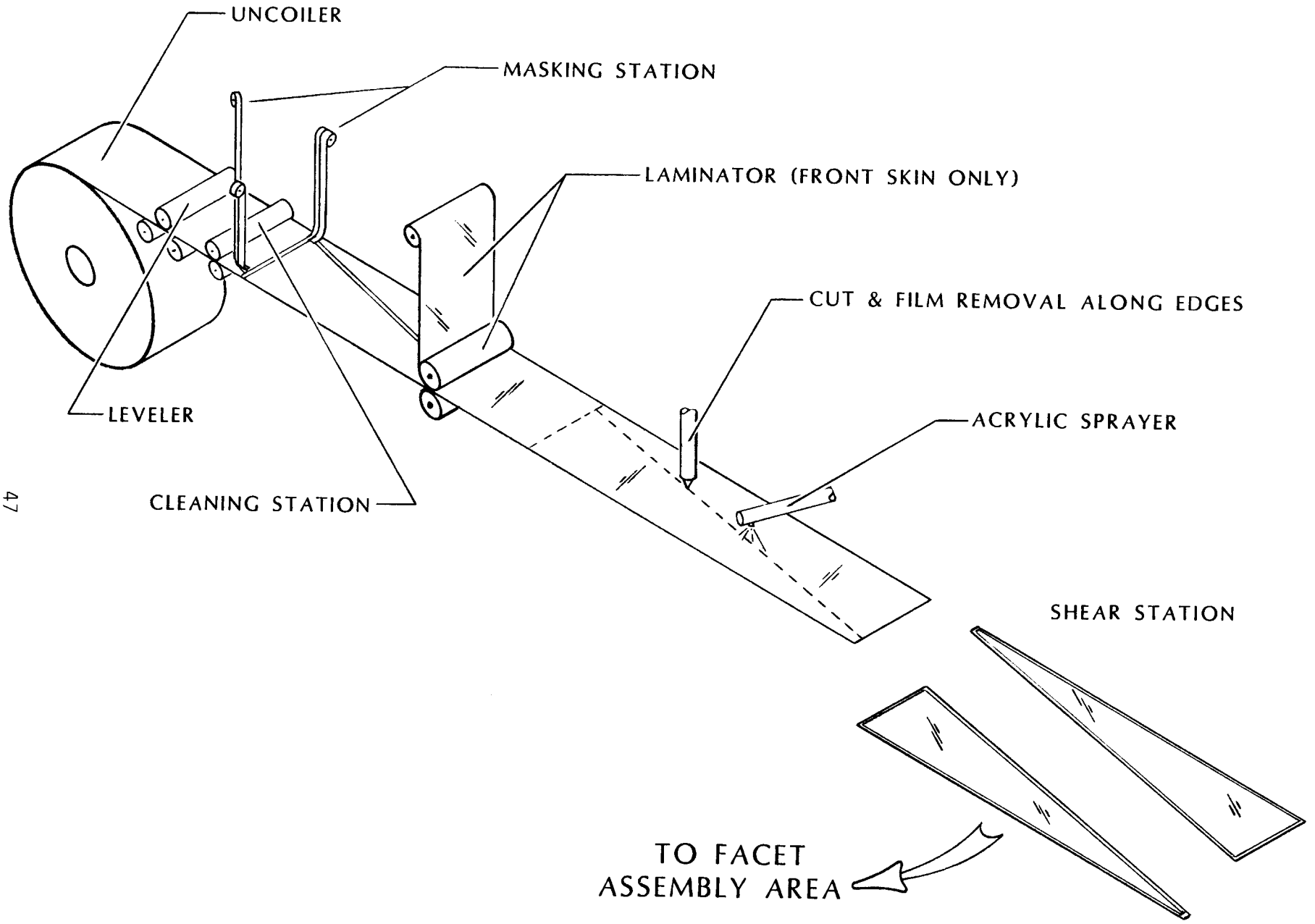

FIG. 3.2 COMMERCIAL OPTICAL ASSEMBLY FRONT AND BACK SKIN PRODUCTION

to be provided within the boundaries of the petal to allow relative motion between the two materials. This requirement was accommodated through application of a disposable tape along the petal cut lines prior to lamination. The free edge was created when the tape was removed. The final process in component fabrication required an acrylic sealant to be applied to the newly formed edge to prevent lateral corrosion through the metalized polymer. The rear skin was fabricated by a similar process, but reflective material was not required.

The corrugated panels that separated the skin and prevented buckling were fabricated by the coil line shown in Figure 3.3. The 0.6-mm by 1.5-m aluminum sheet was leveled, cleaned, and the cross-section was created with a roll forming process. Roll forming is a common coil line process that develops sections through a progressive bending applied by several roll stations. The final stages of the bend serve to impart a radius to the part rather than continued section development. The corrugated sheet had adequate flexibility to conform to the contoured lay-up tool; forming about a second axis was not required.

The edge channels were made with a similar set of forming processes, as shown in Figure 3.4. The coil stock was leveled, cleaned, roll formed, and roll bent. The edge channel had to traverse the radial length of the petal and, consequently, required a parabolic contour to avoid imparting surface error in the facet. The second-order curve was created by actively controlling the position of the top roll during the bending process.

The baseline optical panel design required that the skins be formed to a parabolic contour prior to panel assembly. This requirement was initially imposed to reduce the fabrication stresses associated with forcing a flat sheet into a compound curve: effectively, a great circle problem. The requirement was subsequently dropped after prototype sample fabrication indicated that the forming was not required. One forming approach, termed "three dimensional roll bending" was explored. This process was not used in the final design and, therefore, is explained in Appendix B.

The fabrication of all components for the optical assembly did not require substantial labor or expensive equipment, yet the processes defined will easily operate at the required production volume and produce repeatable parts. Components were produced in a continuous fashion, with no material transfer or intermediate processing steps that require fabrication buffers. These components were transferred to a staging area for assembly.

3.1.2 Optical Element Assembly. Experience has taught the solar industry that metal forming processes (e.g., stamping & bending) cannot, by themselves, produce optically accurate shapes. Optical components must be fixtured to achieve accuracy. For

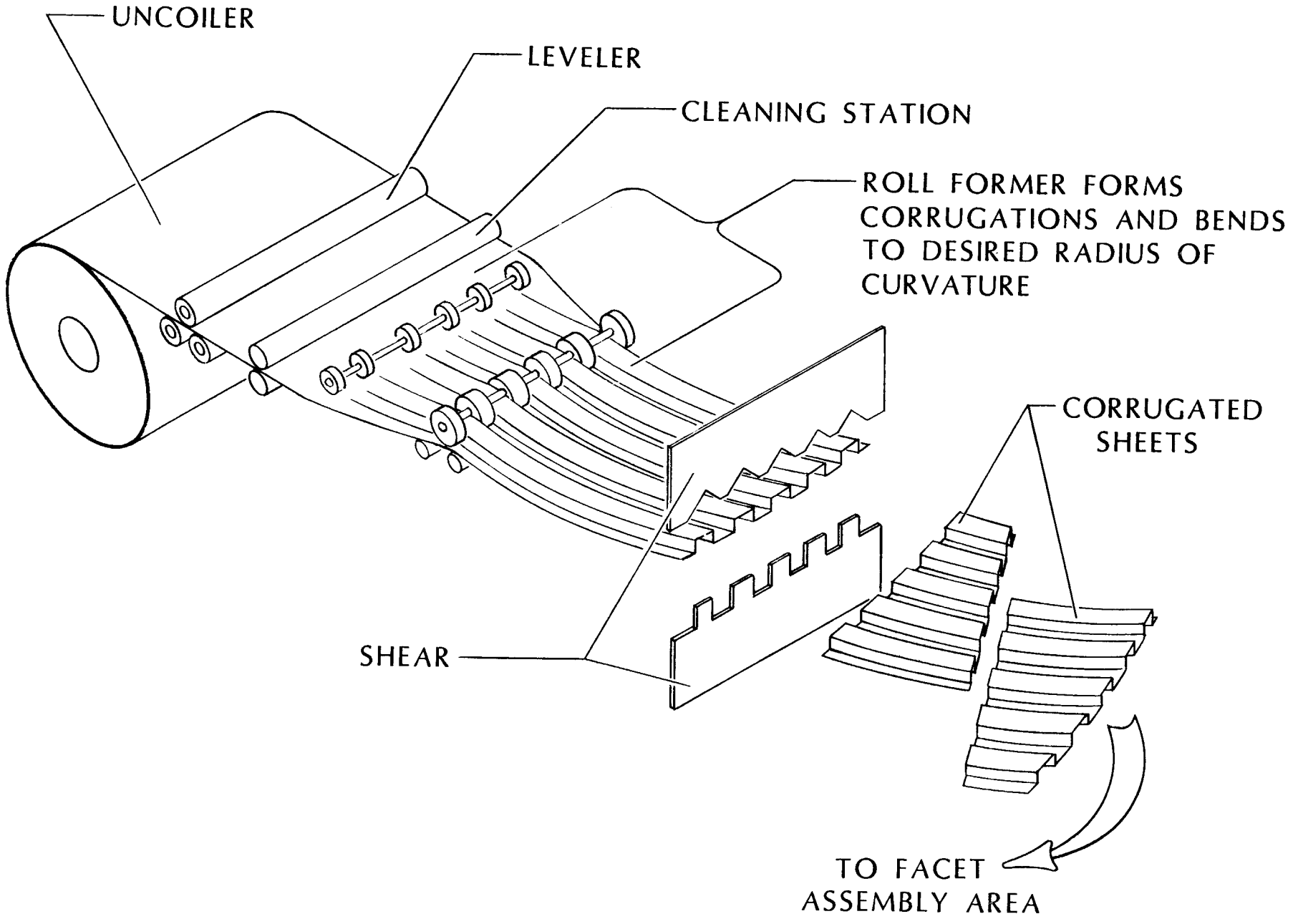

FIG. 3.3 COMMERCIAL OPTICAL ASSEMBLY CORRUGATED SHEET PRODUCTION

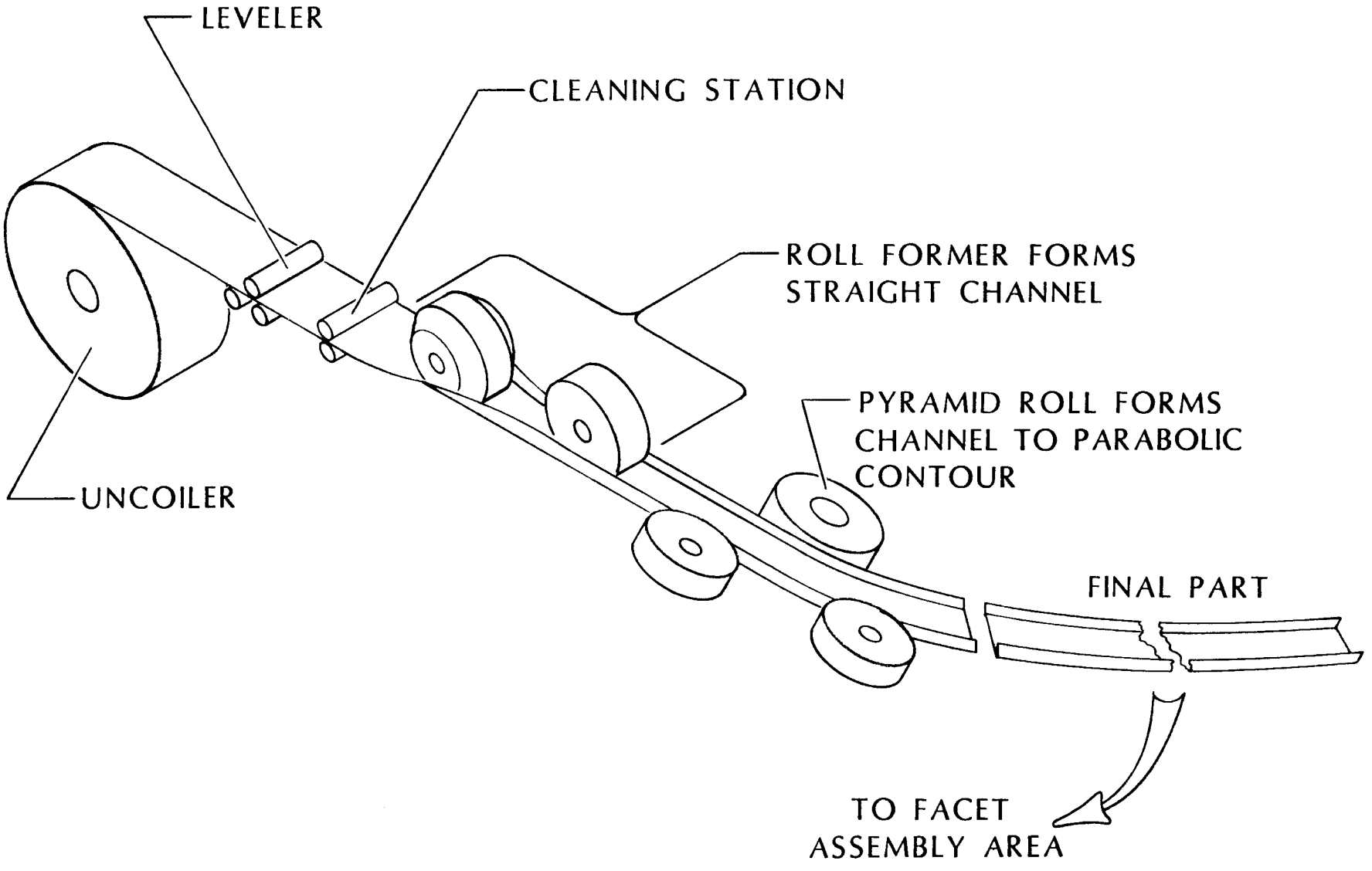

FIG. 3.4 COMMERCIAL OPTICAL ASSEMBLY SIDE AND END CHANNEL PRODUCTION

optical facets, the reflective surface must be held on an accurate, contoured tool while the facet is assembled.

Conventional technology for contoured tool or mold fabrication was explored and resulted in the definition of two basic approaches: Fiberglas "lay-up" and machined tools. Fiberglas technology is used extensively by the antenna industry to make similarly shaped components. A master mold is created by rotating a machined template through wet plaster. Fiberglas impressions are then taken from the master to create the actual working tool. Exploration of this approach in this contract indicated two problems: accuracy would be unacceptably compromised on a second generation tool, and tool stability in a variable environment would create optical error. The approach was subsequently abandoned.

Contoured tools can also be machined from solid stock with large, numerically controlled mills. This approach was identifed as producing acceptable accuracies, but was rejected on the basis of expense.

The contoured tool selected for assembly work represented a departure from conventional technology An adjustable mold was created through the compound deformation of an initially flat plate.

A precise coordinate data measurement (CDM) machine was developed to provide feedback during adjustment. The design of the CDM and its required accuracy are discussed in Appendix A. The complete assembly is shown in Figure 3.5.

Figure 3.6 shows some detail of the mold surface and support structure. As shown, the surface of the mold is routed with vacuum grooves. These grooves provided a continuous vacuum between the front skin and mold. With this system, the front skin was held to the exact contour of the mold during assembly of the facet. Facet accuracy was dominated only by the accuracy of the mold.

Each fastener was designed to minimize local distortion of the aluminum plate. This was accomplished by having ball joints at each end of the fastener and by placing the fasteners normal to the mold surface. This arrangement prevented moments from being induced into the plate.

The front skin was placed on this accurately contoured tool and held in intimate contact with the mold by evacuating the surface. The resin component of a two-part adhesive system was screened onto the back side of the front skin. The activator was applied to both sides of the corrugated panels and edge channels. These components were then positioned on the mold. Finally, the resin component was screened onto the back skin, and the skin was laid in place. Force had to be applied to the assembly to maintain bond line thickness. The vacuum chuck principle was extended to

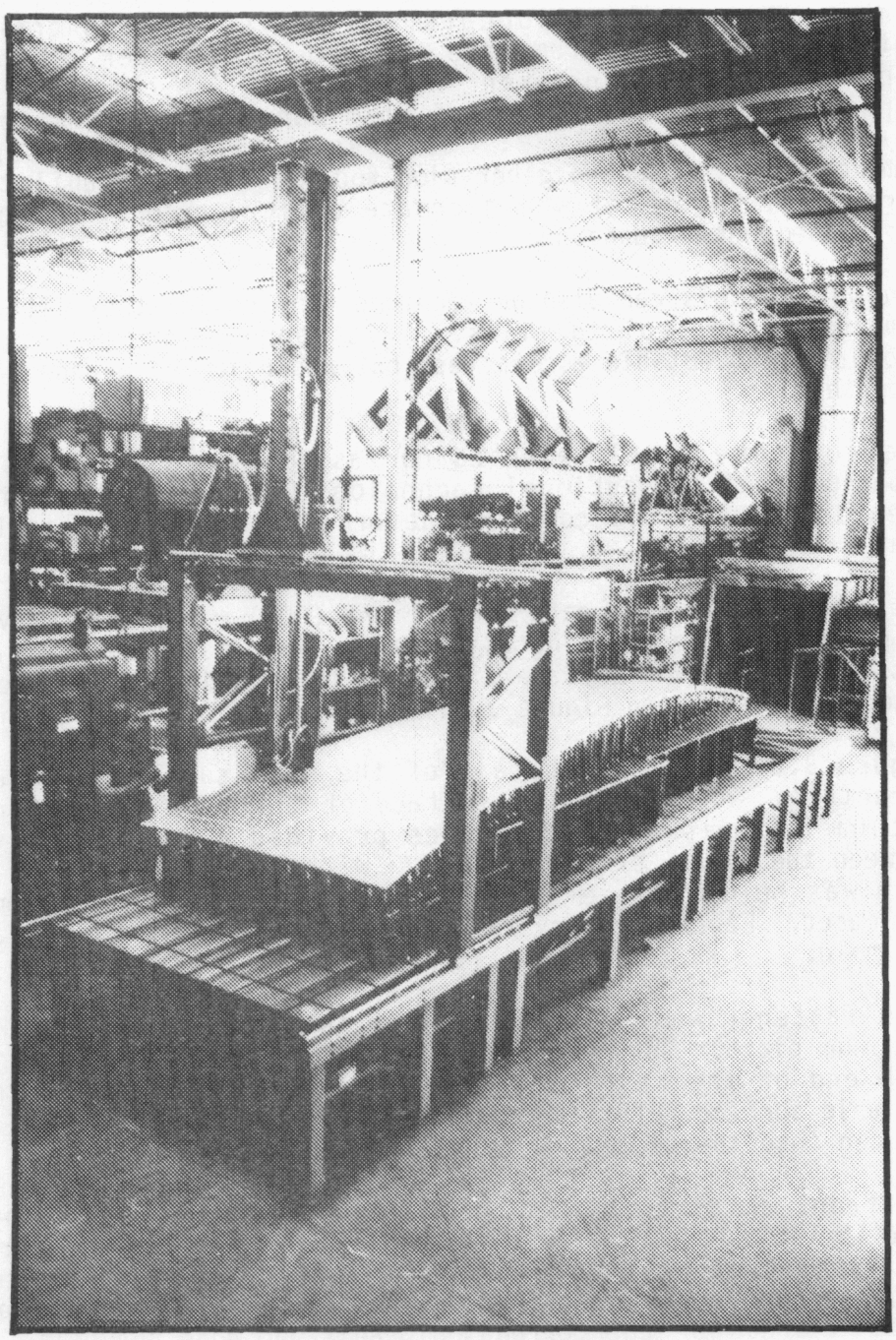

FIG. 3.5 THE ADJUSTABLE MOLD

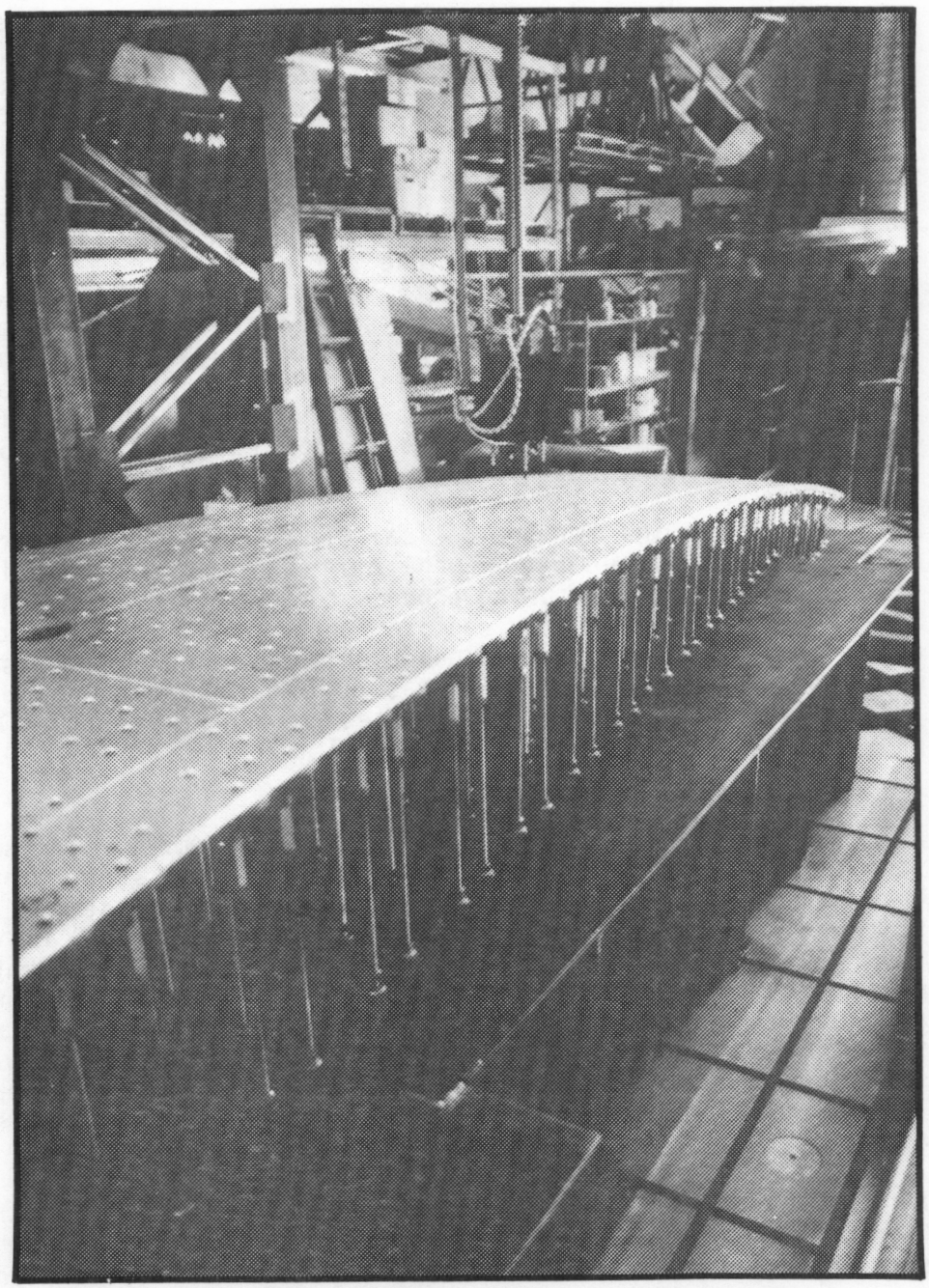

FIG. 3.6 ADJUSTABLE MOLD SURFACE

provide this uniform force by placing a bag over the entire assembly and applying a partial vacuum. Figure 3.7 shows a cross-sectional view of the assembly method.

Several adhesives were initially considered for bonding the optical assembly; acrylic and epoxides were selected as the only reasonable candidates for the final design. The key parameter in adhesive selection was cure time, as both systems had similar specific material costs. Acrylic adhesives provided a cure time of approximately 1 hour versus 4 hours for the epoxides (accelerated curing through heated platens or autoclaves was not considered, because the reflective films would have degraded in these environments). The cure time cost was initially simplified by determining the number of contoured lay-up tools required to satisfy production rates for the different systems. The cure time cost of molds alone served to identify acrylic as the best selection. The acrylic offered several property advantages as well, including a higher shear strength, peel strength, and better durability in a stressed and water-soaked environment. Consequently, the acrylic two-part adhesive system was selected for the final design. Figure 3.8 depicts the costs associated with the adhesive selection.

Make/buy decisions for the optical element were not required for major components because of the performance sensitivity to tolerance and manufacturing process control. All components and assemblies were defined for captive fabrication. Automation for components is a natural by-product of the coil line process. The major batch assembly process was gore fabrication, and some automation was defined for adhesive application, relative position control of parts, and material transfer.

3.1.3 Support Structure Components and Assembly. The support structure included the radial arms, intermediate support rings, hinges, brackets, and the power conversion assembly (PCA) supports. The support structure component and assembly manufactuirng processes were entirely conventional. Conventional processes could be used for this assembly because the optical accuracy of the concentrator is not reliant upon demanding tolerances in structural fabrication. The panel mounting structure was reasonably independent from the panel shape and location. The connection between the two elements was accomplished with independently adjustable hinges.

Two major structural elements were open web beams and trusses fabricated from hot rolled steel base stock. The primary and secondary members of the trusses and rings were fabricated from only two base shapes to reduce the types of raw materials required for concentrator fabrication. Materials for these trusses were furnished as straight, random lengths that required conventional processing steps: shear to length, punch, notch and, in some instances, roll bend. These components were

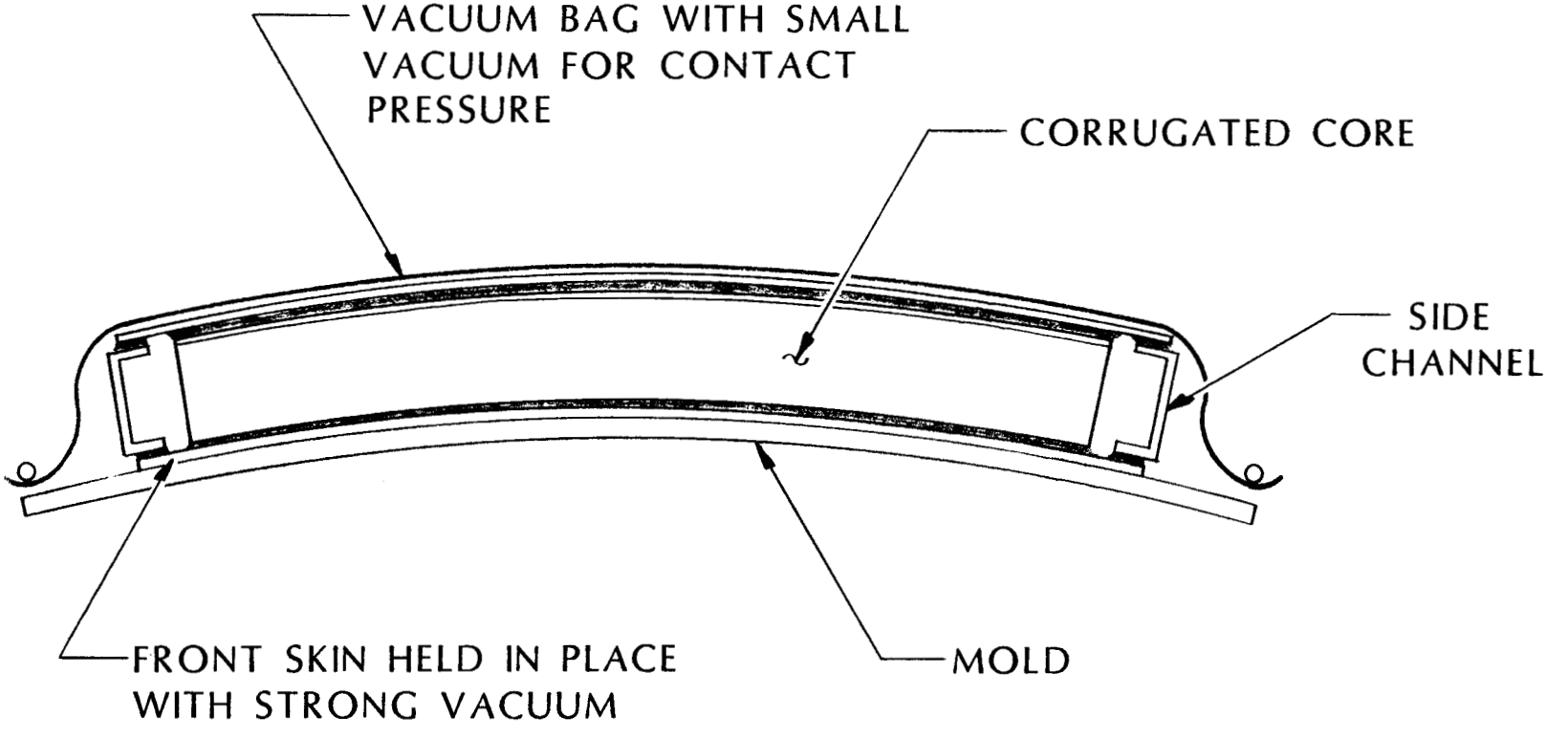

FIG. 3.7 ASSEMBLY METHOD

- ADHESIVE

	COST		
	$/GAL.	$/DISH	$/m^2
EPOXIDE	∽27	∽621	∽4.14
ACRYLIC	∽28	∽644	∽4.29

- MOLD TIME

	MOLD TIME	1,000 MOLDS	1,000 COST•	10,000 MOLDS	10,000 COSTS•
EPOXIDE	4 HRS.	34	1.63/m^2	334	1.42/m^2
ACRYLIC	1 HR.	9	0.48/m^2	84	0.38/m^2

- TOTAL EPOXY $ 5.56-5.77/m^2 ACRYLIC $ 4.67-4.77/m^2

• BASED ON 10 YR. SERVICE LIFE, 80,000/MOLD BASE PRICE, 10% DISCOUNT AT 10-50, 15% DISCOUNT AT 50-100, 20% DISCOUNT ABOVE 100.

FIG. 3.8 PARAMETRIC ADHESIVE CURE COST.

fixtured, welded, cleaned and painted during the assembly process.

These components were assembled in a captive facility rather than purchased from outside vendors. The relatively few raw material components, combined with the quantity of identical parts even for the smaller production rate defined in this design, provided a significant return on investment in automated equipment. The processes that were clearly appropriate for automation are welding, painting, and material handling. Semiautomatic processes were defined for the cut, notch, punch, and bend stations. The degree of automation for these components and assemblies was made through parametric trade-off between labor and capital cost.

The third major structural element was the hub, fabricated as a rolled plate girder beam with plate web stiffeners. The hub was fabricated from hot rolled steel. Three base stock materials were required, including two plate thicknesses and flat bar stock. The plate girder was selected rather than an open web, because element supported very large and concentrated loads at the drive attachment. This structure had to serve as the rigid body for truss attachment, and had to provide substantial stiffness. The optical accuracy of the dish was largely separated from fabrication tolerance by providing a secondary element for the gore/hub attachment assembly. Inaccuracies in the arm mount were multiplied by the radial distance traveled, and a spot-milled surface at this attachment was considered prudent in spite of the isolation of truss and optical error through the adjustable hinge.

The make/buy selection on this component was a relatively even proposition at the 1,000-parts-per-year production rate; at 10,000-parts-per-year, the part would be manufactured in a captive facility. Consequently, the captive fabrication approach was selected for ease in cost comparison. A relatively simple automated welding and milling station would be adaptable to this part manufacture. Shear and bend operations were defined as manually controlled.

Secondary components, such as brackets, hinges, and PCA support component and assembly were relatively insensitive to the overall cost. They were defined as purchased components, with final assembly at the captive central facility.

3.2 Construction Processes

The parabolic dish defined in this development effort must be assembled at the site. Several construction options were considered in the parametric design of the concentrator. The key issues defined were

* The construction methods should be suitable for a limited number of concentrators per site.
* Facet alignment should not rely upon the accuracy of the support structure.
* Facet alignment should be required during erection only.

These assumptions had a substantial impact upon the construction process and the concentrator joint design. They were selected to accommodate a broad market, high performance, and low life-cycle cost.

The first of these assumptions required the dish to be manufactured at a central facility. Site construction facilities were defined for final assembly of parts that could not be shipped complete. These facilities were limited, and truck based. The major components assembled at the site were 6 radial truss arms, 6 middle ring segments, 6 outer ring segments, 30 optical petals, and the PCA support tripod. Structural joints were achieved with bolted connections. Optical assembly joints required adhesive and mechanical fasteners. The optical-to-structural joints were bolted connections.

Facet alignment was defined as insensitive to structural accuracy to reduce the cost of the rear supporting structure. The tolerance requirements for a parabolic dish of this aperture were not conducive to standard fabrication methods for open web beams or plate girders. Concentrator adjustment was undesirable if the fluctuating load environment could have altered the initial alignment. The stiffness of the optical element, after each gore was bonded to create a continuous surface, was substantial, even by comparison to its supporting structure. The concentrator was specifically designed to incorporate this stiffness to provide optical accuracy and load distribution. Therefore, field adjustment was deemed acceptable for this design.

3.2.1 Joint Adjustment. Adjustment was provided at each attachment between the optical element and the rear supporting structure. The support rings attached to the optical element through a series of hinges, allowing adjustment freedom parallel to the optical axis and in the circumferential direction (Figure 3.9). The circumferential adjustment was primarily allowed for ease in fabrication and avoidance of localized moment loads transferred through the rigid direction of the hinge to the optical element. It was accomplished through use of a 4-inch wide hinge placed between vertical standards that tolerated

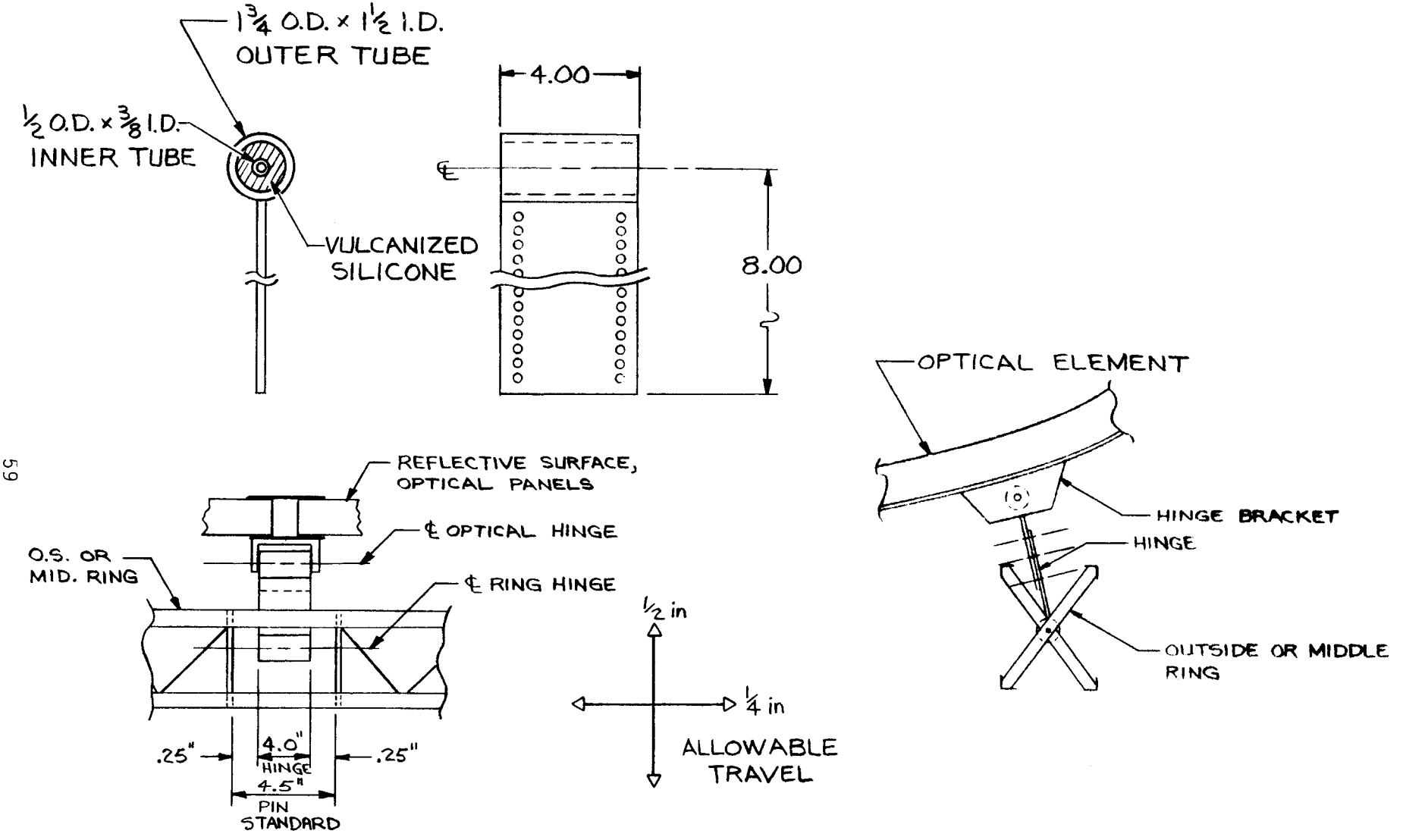

FIG. 3.9 PANEL ADJUSTMENT AT SUPPORT RINGS

+/-1/4 inch of circumferential travel. The backlash was removed by slipping brass washers over the ring hinge pin during assembly. Vertical adjustment was accommodated through the of 2 overlapping hinge plates. The hinge plates had a hole pattern punched so that 2 holes would always be in alignment for any discrete vertical adjustment of 0.03 inch over a +/- 1/2 inch. The 2 aligned holes provided a convenient bolted connection. After all hinge plates were adjusted, the backlash was removed by drilling/reaming or punching 2 additional holes, which were subsequently pinned.

The petal-to-hub connection provided adjustment along the optical axis for all petals, though the adjustment was not independent for each petal (see Figure 3.10). Petal independence was provided for all connections away from the vertex and, consequently, was not required at the center. The global translation of all petals was accomplished at the bolted connection between an intermediate or "secondary" element and the hub by virture of a slotted hole. Limited independent planar translation and tangential rotation was provided by the flexibility of the joint. The "secondary" element was also slotted between each facet to decrease its hoop stiffness. Each slotted section of the secondary hoop element acted as a cantilever and torsional spring. The objective of the joint adjustment was to eliminate any potential to form a cusp at the center of the parabola and to accommodate inevitable fabrication error without inducing localized moment loadings.

3.2.2 Joint Restraint. The joints between the optical element and rear structure accommodated radial translation. The objective of this additional degree of freedom was to accommodate relative thermal expansion between the optical element (aluminum) and the rear structure (steel). The hinge was actually normal to the concentrator surface at an intermediate temperature. The hinge swing radius was adequate to impart very little loading into the concentrator at temperature extremes, because its tip motion was effectively rectilinear over the small angles required to tolerate the temperature environment. The inherent flexibility of the hub attachment also allowed some radial motion.

The X-brace that formed the pin standard for hinge connection was fabricated from flat stock. The lack of section in the lateral direction reduced transfer of localized moment loadings in the nonhinged direction from the structure to the optical element. Finally, the load from hinge pin to body was transferred through a vulcanized silicone. This type of joint provided a small amount of structural damping and reduced the stiffness of the connection.

The joints between optical panels, on the other hand, represented a radial and circumferential fix. This joint is shown in Figure 3.11. Shear and axial stresses were transferred continuously

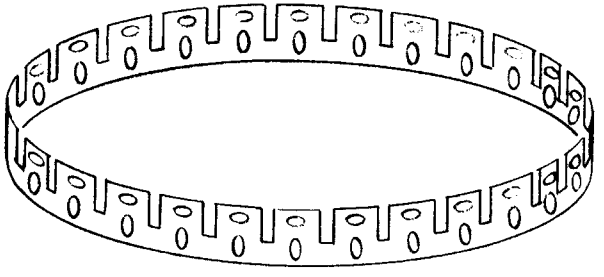

DT'L OF SECONDARY HOOP

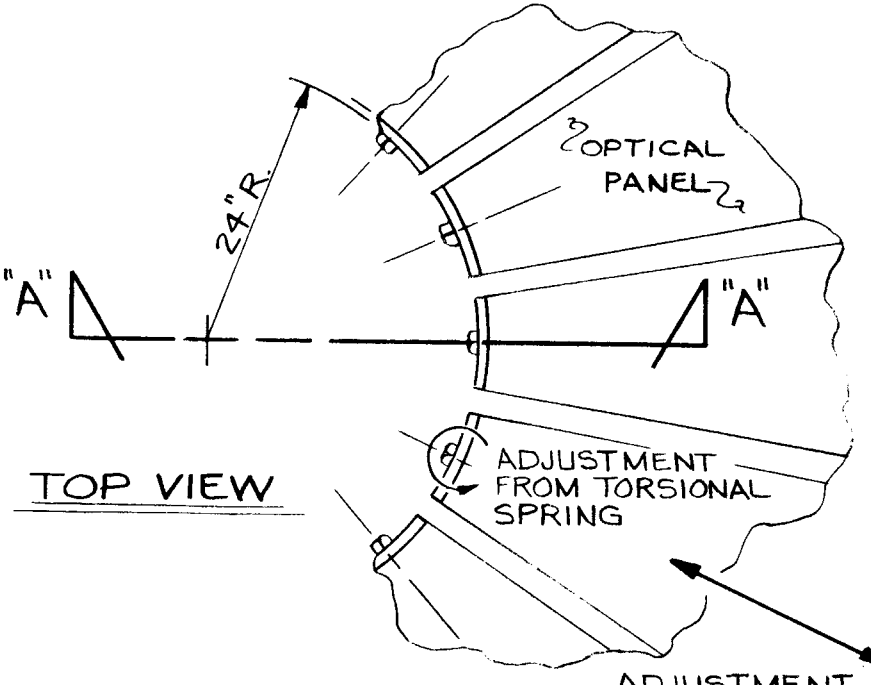

TOP VIEW

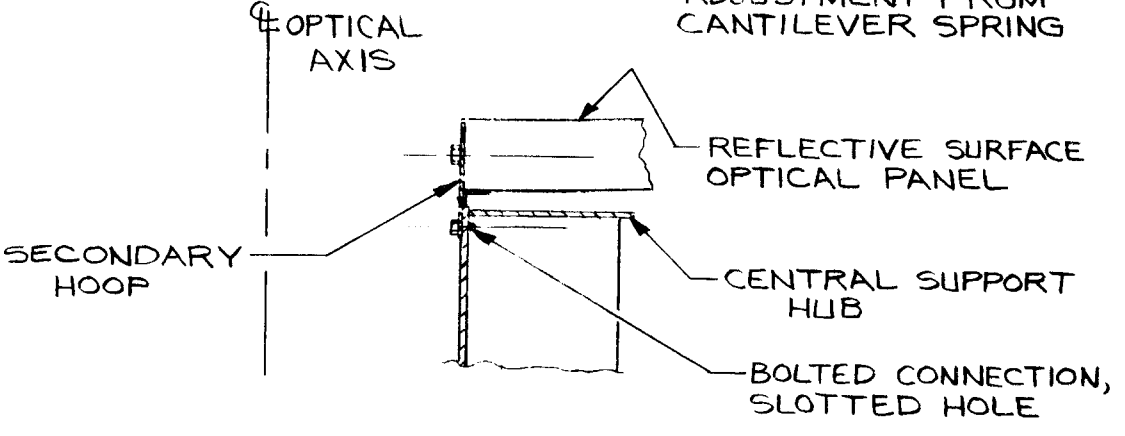

SECTION "A-A"

FIG. 3.10 PANEL ADJUSTMENT AT HUB

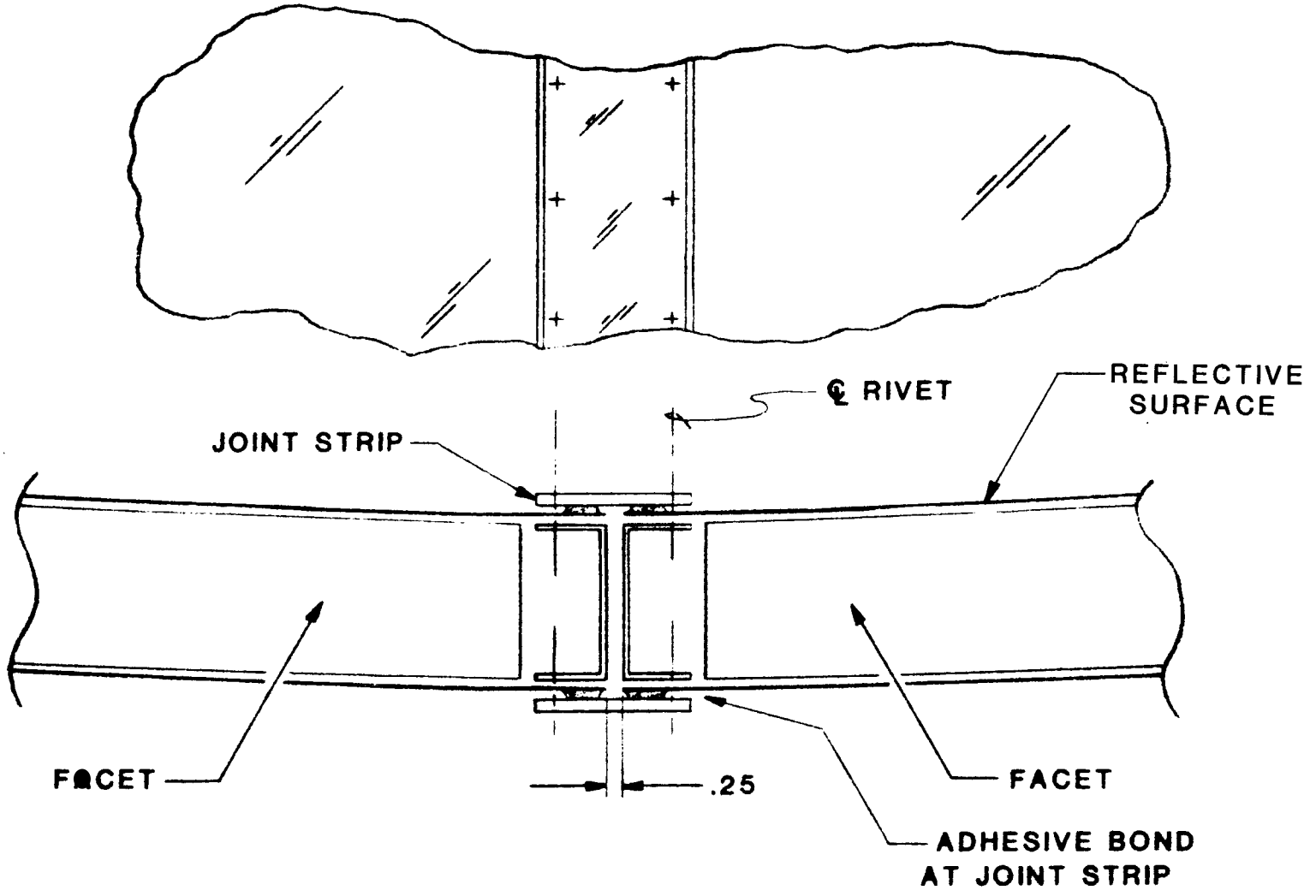

FIG. 3.11 OPTICAL FACET JOINT

across the joint through an adhesive bond. Bending stresses were accommodated without localized distortion due to the area section formed by edge channels and the joint strip. The 1/4 inch gap between optical facets accommodated a reasonable panel width tolerance and the tendency for any width error to be progressive.

3.2.3 Concentrator Adjustment. The concentrator had several degrees of freedom during the construction process: optical panels could be adjusted along the optical axis as a group at the hub and individually at mid-span and perimeter; the gores could be moved circumferentially through hinge adjustment and optical panel gap variance; and the hinges coupled to the cantilever spring/slotted hoop had limited adjustment in the radial direction. The rear structure was bolted together; each bolted joint was provided with a hole slotted in at least one direction to accommodate manufacturing tolerance. This wide variety of motion was critical to ease assembly and tolerance. Careful attention had to then be given to the method of implementing adjustments for optical accuracy to be obtained.

The construction process outlined for this design began with complete rear structure assembly on a truck-mounted turntable. A large post with attached arm was inserted into the turntable at the dish vertex, as shown in Figure 3.12. This post and arm assembly effectively formed a large cylindrical coordinate measurement system that was accurate, simple, and durable. Dial indicators were mounted at the hinged radius to provide the optical axis (Z) measurement. A vernier, similar to that mounted on a transit or theodolite, was mounted at the vertex to provide the rotational (theta) coordinate. The radial (r) coordinate was not required except at the discrete location defined by the dial indicator position. Adjustment was primarily provided with the overlapping hinge described in a previous section.

Adhesive was applied to the joining strips of the first petal; the panel was laid in and temporarily bolted to the hinges without regard to final accuracy. The "R-Theta" alignment tool was rotated and the panel was aligned. Each subsequent panel (Figure 3.13) was inserted following the same sequence; adhesive application, lay-up, and adjustment, proceeding around the dish. The gap between panels, placement measurement, and adjustment freedoms prevented tolerance stack-up from being an inordinate problem. The resin-to-activator ratio of the adhesive system was designed for a 24-hour cure to allow minor subsequent adjustments after each panel was laid in place. Contact between the joint strip and panel was maintained with blind fasteners. The fastening tool was designed to translate along the alignment arm, drill through holes punched in the joint strip, and rivet (see Figure 3.14). The alignment tool was removed, the PCA support assembly bolted into place, and the entire dish was hoisted into place through attachment at the hub assembly (see Figure 3.15).

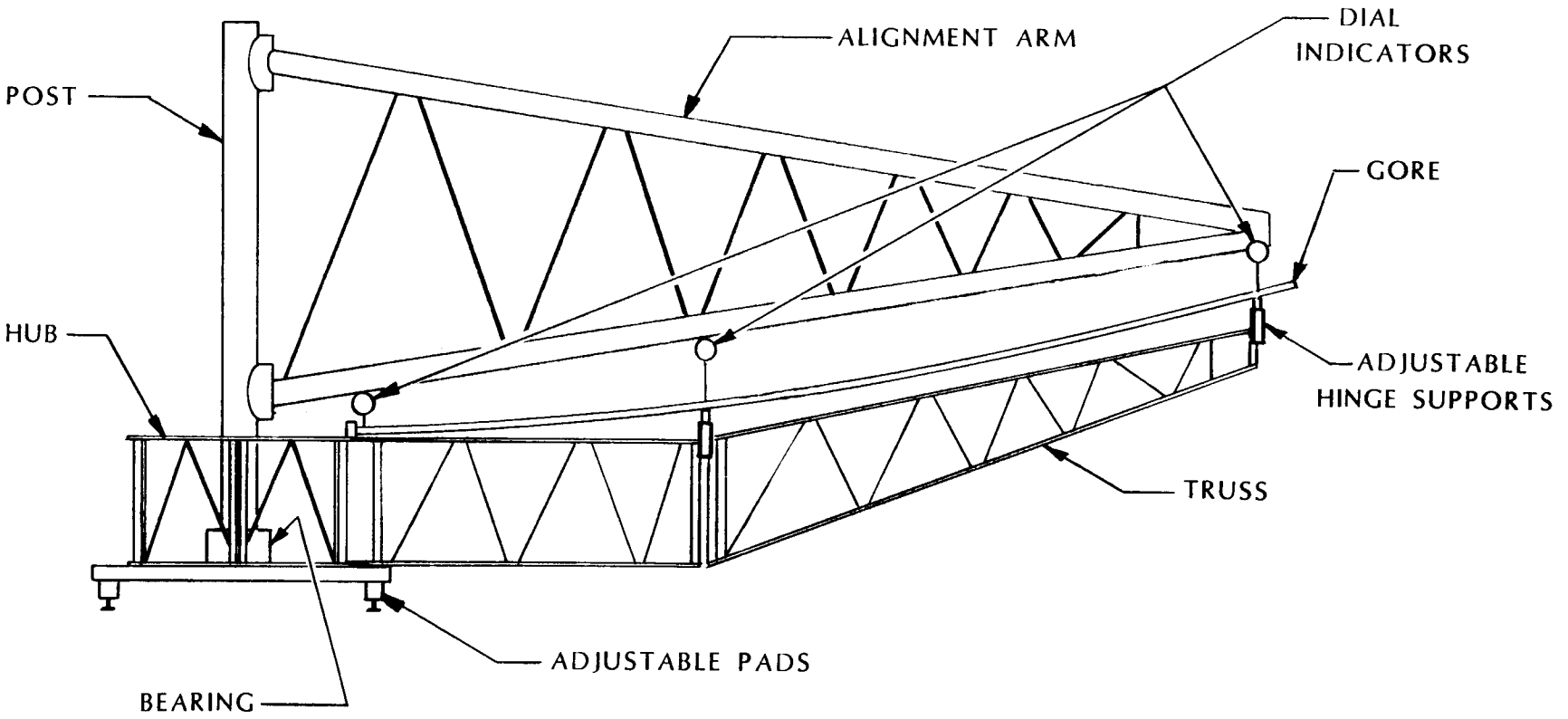

FIG. 3.12 R-THETA ALIGNMENT TOOL

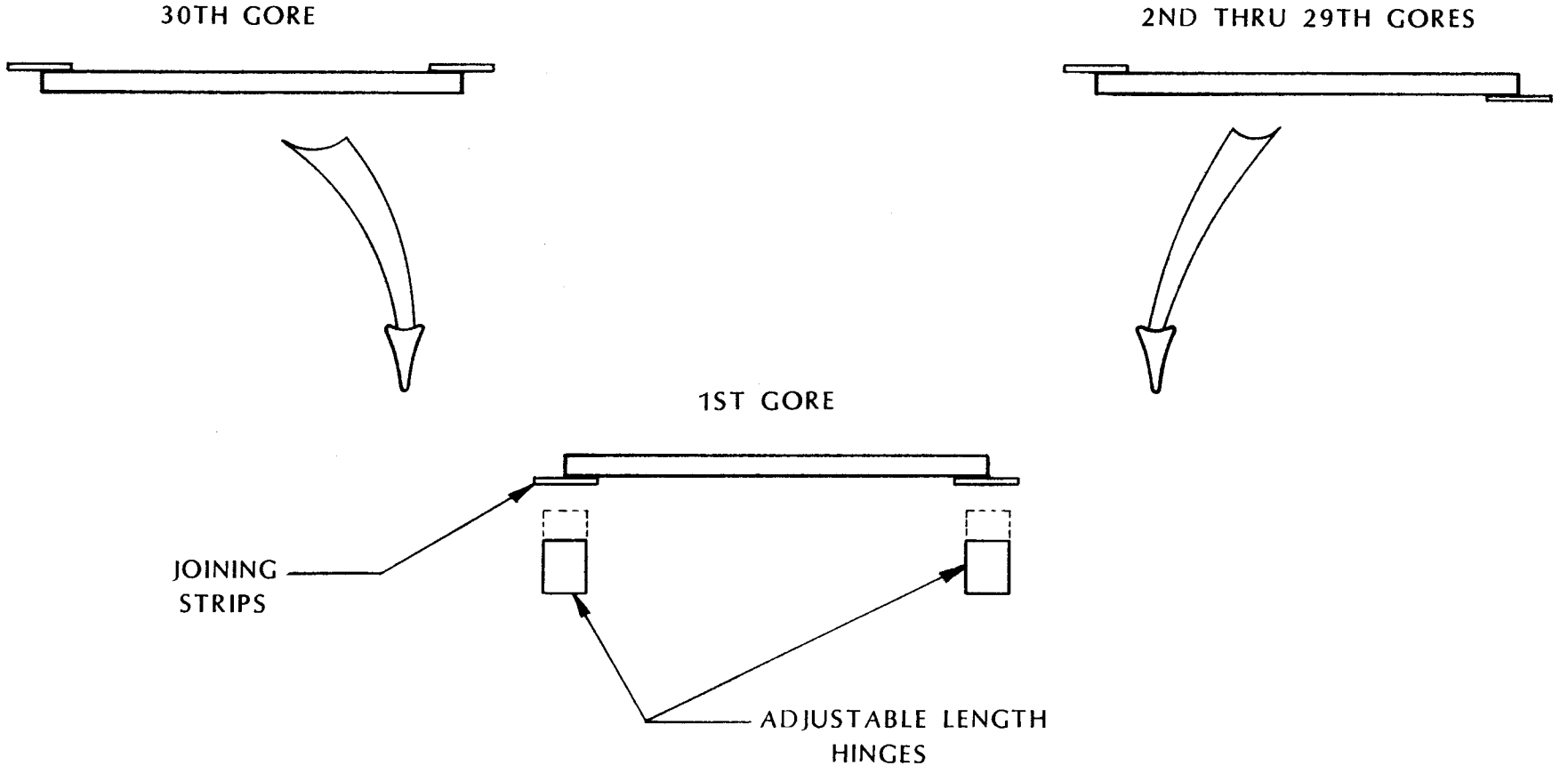

FIG. 3.13 GORE LAY-UP SEQUENCE

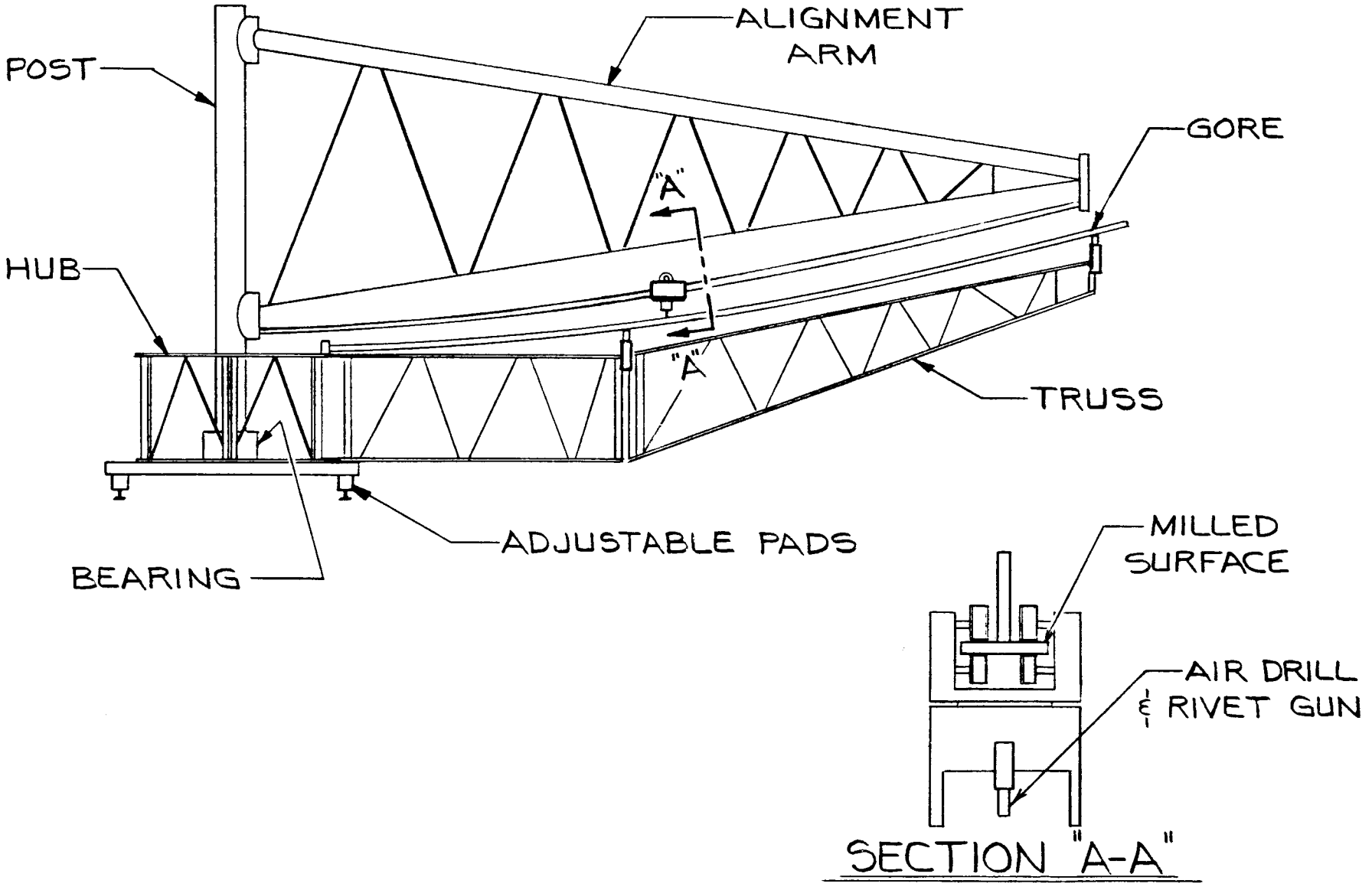

FIG. 3.14 FASTENING TOOL

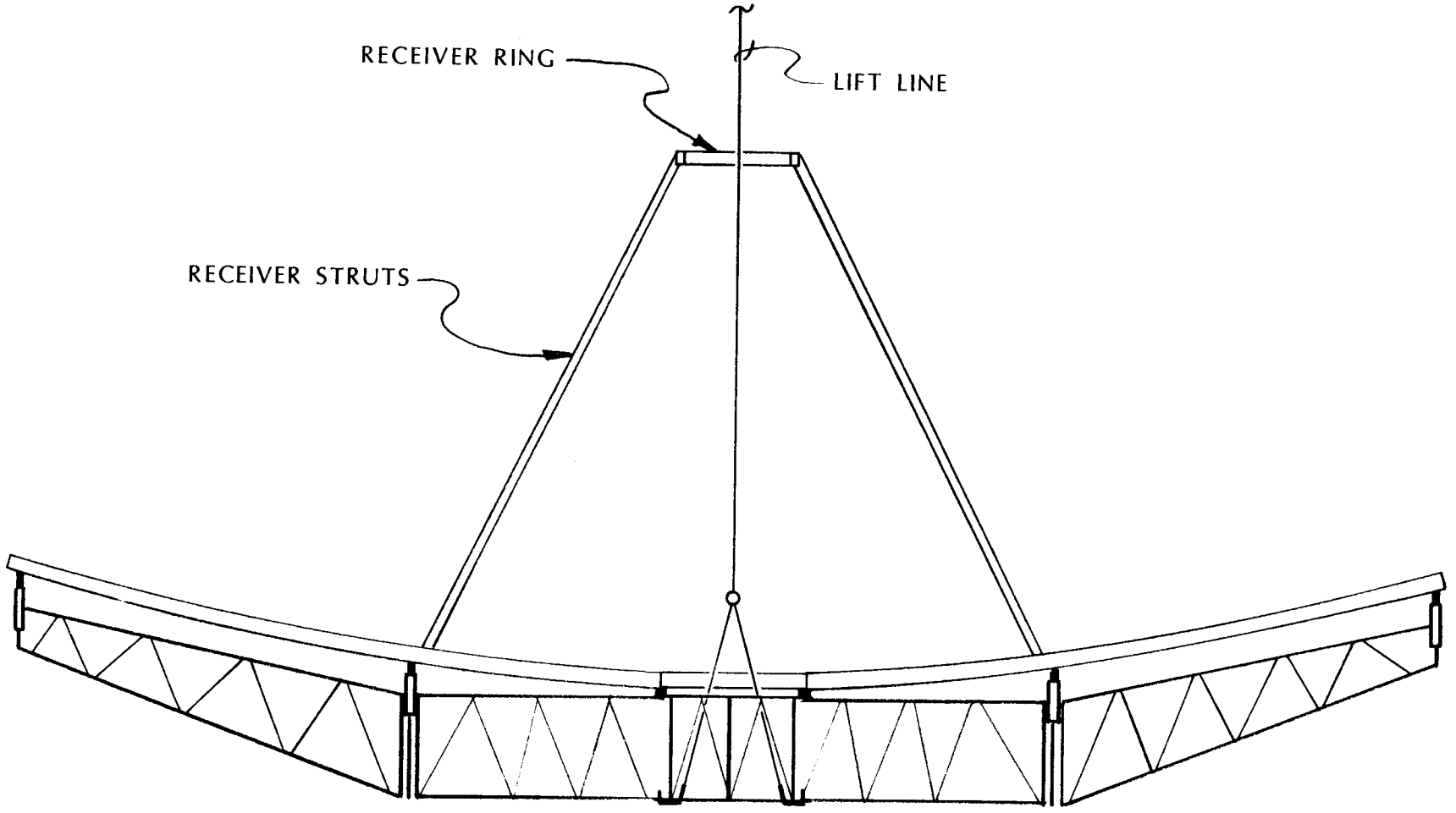

FIG. 3.15 LIFT ATTACHMENT

3.3 Reflective Assembly Cost

Production costs for the reflective assembly were developed for rates of 1,000 and 10,000 reflective assemblies per year. The reflective assembly consisted of three major subassemblies: the optical element, the supporting structure, and the PCA support. The manufacture and installation of the reflective assembly were completely isolated from the fabrication and installation of the foundation, pedestal, drive, field wiring and PCA.

Additional assumptions applying to the cost analysis were

* Costs reported in September 1986 dollars.
* A relatively stable product design occurs over the equipment life cyle.
* Minimal marketing expense required to obtain and maintain a stable sales volume.

3.3.1 Capital Costs. Capital costs were divided into the categories of equipment costs, building costs, and land costs.

3.3.1.1 Equipment. The equipment costs required to produce the reflective assemblies are presented in Table 3.1. Costs are presented for production rates of 10,000 and 1,000 reflective assemblies per year. The equipment costs are further itemized in Table 3.2.

3.3.1.2 Building. The building requirements for the fabrication of the reflective assembly components are presented in Table 3.3. Manufacturing area was estimated at $43 per square foot of floor space, and administrative space was estimated at $57 per square foot. Based on the two production rates, building cost would be $4,550,000 and $3,460,000, respectively.

3.3.1.3 Land. Land costs for the central manufacturing facility were based on an improved land cost of $20,000 per acre. On this basis, the land expenses were $120,000 and $80,000, respectively.

The initial capital investment is summarized in Table 3.4. The depreciation of these expenses is presented in Table 3.5. The depreciation (capital replacement cost) represents $1.34/$m^2$ of aperture at 10,000 per year and $5.07/$m^2$ at 1,000 per year.

3.3.2 Direct Materials. The direct material costs are given in Table 3.6. Costs for raw material were based on vendor estimates at the appropriate volumes. These costs were $.90 per lb of aluminum, $.33 per lb of hot rolled structural steel, and $28.00 per gallon of adhesive. For these items, no significant price

TABLE 3.1

EQUIPMENT CAPITAL COST

ACTIVITY	CAPITAL 10,000/year	COST 1,000/year
Gores	$ 9,129,000	$2,779,000
Hub	235,000	235,000
Trusses	892,000	465,000
Ring	1,724,000	870,000
General	6,150,000	1,665,000
Total	$18,130,000	$6,010,000

TABLE 3.2
EQUIPMENT COSTS

Description	Cost ($1,000)	Qty.*	Ext.* ($1,000)
Front & Back Gore Skins			
Upender	21	2/2	42/42
Uncoiler	23	2/2	46/46
Leveler	33	2/2	66/66
Cleaner	22	2/2	44/44
Template System	25	1/1	25/25
Laminator	32	1/1	32/32
Film Shears	30	1/1	30/30
Aluminum Shears	30	2/2	60/60
Acrylic Sealers	40	1/1	40/40
Corrugation			
Uncoiler	23	2/1	46/23
Leveler	33	2/1	66/33
Roll Former	60	2/1	120/60
Pyramid Roller	50	2/1	100/50
Shear	25	2/1	50/25
			767 / 576

* Quantity or price at 10,000 units per year are shown left of the slash (/) mark and 1,000 units per year are shown right of the slash (/) mark.

TABLE 3.2 (cont.)
EQUIPMENT COSTS

Description	Cost ($1,000)	Qty.	Ext. ($1,000)
Edge Channel			
Uncoiler	15	2/1	30/15
Leveler	33	2/1	66/33
Roll Former	50	2/1	100/50
Pyramid Roller	50	2/1	100/50
Shear	10	2/1	20/10
Joining Strips			
Uncoiler	15	2/1	30/15
Leveler	15	2/1	30/15
Punch/Shear	40	2/1	80/40
Gore Fabrication			
Molds	64/80	84/17	5376/1360
Vacuum Pumps	10	10/2	100/20
Assembly Fixtures	5	21/4	105/20
Adhesive applicators	25	21/4	525/100
Drilling/Riveting Machine	50	21/4	1050/200
Transfer Equipment	25	10/1	250/25
Q. C. Fixture	250	2/1	500/250
			8362 / 2203

TABLE 3.2 (cont.)
EQUIPMENT COSTS

Description	Cost ($1,000)	Qty.	Ext. ($1,000)
Trusses			
Primary Punch & Shear	30	1/1	30/30
Secondary Bender	15	2/1	30/15
Secondary Transfer System	4	2/1	8/4
Assembly Fixture	8	2/1	16/8
Automated welder	400	2/1	800/400
Transfer Equipment	8	1/1	8/8
Rings			
Secondary Bender	15	4/2	60/30
Secondary Transfer System	4	4/2	16/8
Assembly Fixture	8	4/2	32/16
Automated Welder	400	4/2	1600/800
Transfer Equipment	8	2/2	16/16
Hub			
Plate Shear	25	1/1	25/25
Plate Pyramid Roller	40	1/1	40/40
Flange Pyramid Roller	40	1/1	40/40
Automated Welder	80	1/1	80/80
Automated Spot Mill & Drill	50	1/1	50/50
			2851 / 1570

TABLE 3.2 (cont.)
EQUIPMENT COSTS

Description	Cost ($1,000)	Qty.	Ext. ($1,000)
Brackets			
Automated Drill Press	15	10/1	150/15
General Plant Equipment			
Paint Line		lot	2000/250
Maintenance Equipment		lot	500/250
Miscellaneous		lot	500/150
Dish Assembly			
Assembly Machine	150/250	20/4	3000/1000
			6150/1665
Total		$18,130,000 /	$6,010,000

TABLE 3.3
BUILDING COSTS

Activity	Floor area (sq. ft.) 10,000 per year	1,000 per year
Gore fabrication & Assembly	36,900	10,800
Support Structure	17,400	29,000
Paint	8,000	12,000
Storage & Aisle	31,150	20,500
Administrative	9,345	6,150
Total Area	102,795 ft^2	78,450 ft^2
Cost @ \$43/ft^2 manufacturing	\$4,018,350	3,108,900
\$57/ft^2 office	532,665	350,550
Total Cost	\$4,550,000	\$3,460,000

TABLE 3.4
CAPITAL COST SUMMARY

	10,000 Reflectors per year	1,000 Reflectors per year
Equipment	$18,130,000	$6,010,000
Building	4,550,000	3,460,000
Land	120,000	80,000
Total	$22,800,000	$9,550,000

TABLE 3.5
CAPITAL REPLACEMENT

	Initial Cost	Life (Years)	Specific Depreciation Cost Dollars per sq. meter of aperture
Equipment	$18,130,000 / $6,010,000	10	1.19 / 3.94
Building	$ 4,550,000 / $3,460,000	20	.15 / 1.13
Land	$ 120,000 / $ 80,000		- / -
			1.34 / 5.07

Based on: 10,000 units per year/1,000 units per year.
No salvage value.
Straight line depreciation.
September 1986 dollars.

TABLE 3.6
DIRECT MATERIAL COSTS

Item	Cost ($/Dish)
Film	2,538.00 / 2,538.00
.025 Al gore skins	1,061.21
Gore Corrugation	1,128.60
Edge Channel	451.23
Joining Strips	162.93
Adhesive	644.00
Hub	135.30
Trusses	634.50
Ring	574.20
Brackets	261.00
Misc. Hardware	69.00 / 114.00
Paint	27.00
Struts	300.00
Retractable Strut drive & controls	600.00
	$8,595.97 / $8,640.97

Total = $56.26/m^2 at 10,000 per year
$56.55/m^2 at 1,000 per year

Based on 10,000 units per year/1,000 units per year September 86 Dollars

variation existed between the two production rates. The reflective film was chosen to be $\$16.60/m^2$, driving the material cost to $\$56.26/m^2$ at 10,000 units per year. The actual price of the film, especially at the higher production rate, could fall substantially below this figure. If the reflective film were available at $\$3.19/m^2$, the material costs would fall by \$2030.40. This is equivalent to a $\$13.54/m^2$ drop in the reflector assembly cost.

3.3.3 Labor Costs. Labor was defined as the workers who directly participate in the manufacture and installation of the reflective assembly and its parts. This included most workers at the central manufacturing facility and the site installation crews.

The labor requirements for the reflective assembly are presented in Table 3.7. At 10,000 reflective assemblies per year, 140 workers would be required at the central manufacturing facility and 135 workers at the sites. At 1,000 reflective assemblies per year, 31 workers would be required at the central manufacturing facility and 20 at the site.

The cost of this labor included a base wage of \$8.45 and \$3.80 in fringes. The fringe included such costs as Social Security payments, unemployment insurance, Workmen's Compensation, insurance policies, pension funds, vacations, holidays, and premiums. The cost was based on the actual number of hours spent on a task. The total labor cost at 10,000 reflective assemblies per year would be $\$4.41/m^2$ and $\$8.22/m^2$ at 1,000 reflective assemblies per year. These labor rates were based upon past experience at Solar Kinetics with assembly labor.

3.3.4 Additional Costs. The additional expenses involved in the manufacture and installation of the reflective assemblies were divided into three general categories: Indirects and Consumables; G & A, Taxes and Profits; and Transportation.

3.3.4.1 Indirects and Consumables. Indirect costs included all costs (labor and supplies) incurred by plant maintenance, engineering, receiving, shipping, clerical, drafting, purchasing, inspecting, first line supervision, and other employees not involved in direct fabrication, management, or marketing. Part of the indirect cost was directly associated with production, such as first line supervision, receiving, and inspection. Indirect labor was estimated at 30 percent of the direct labor rate at 10,000 units per year and 50 percent at 1,000 units per year. Engineering, clerical, and drafting support was estimated at 30 percent of the direct labor cost at 10,000 units per year and 55 percent at 1,000 units per year.

TABLE 3.7
LABOR REQUIREMENTS

HOURS PER REFLECTIVE ASSEMBLY

	10,000/Year	1,000/Year
Gores	20.0	30.0
Hub	1.6	4.0
Trusses	1.8	6.0
Rings	2.8	8.0
Paint	1.6	14.0
Site Assembly	27.0	40.5
Total	55.0 hrs.	102.5 hrs.

All materials and supplies that were necessary during production but did not appear in the final product were considered consumables. Consumables included all material waste, operating and processing supplies, nondurable tooling and equipment, and utilities. Consumables were estimated to be 6 percent of the material cost at 10,000 units per year and 10 percent of the material cost at 1,000 units per year.

The total cost of indirects and consumables was $6.15/m^2$ at 10,000 reflective assemblies per year and $14.70/m^2$ at 1,000 reflective assemblies per year.

3.3.4.2 General & Administrative, Taxes and Profits. General and administrative costs (G&A) were leveraged on the combination of all direct labor and indirect labor. The rates assumed for this study were 25 percent on both production volumes. These percentages were also derived from rates in effect at SKI during a time of major collector production, though research and development costs were deleted. The result of this assumption was a G&A cost of $2.60/m^2$ and $5.61/m^2$ for production rates of 10,000 and 1,000, respectively.

Profit and taxes were leveraged on capital investment income. The profits were established as a 15 percent internal rate of return with a 10-year life. The capital basis included all equipment, leasehold improvements, and transportation equipment. The result of this rate of return was $3.67/m^2$ and $13.16/m^2$, respectively, for 10,000 and 1,000 unit production. For convenience, taxes were also based upon capital and established at 2.50 percent of initial investment per annum. These costs were $0.37/m^2$ and $1.59/m^2$.

3.3.4.3 Transportation Cost. Transportation costs were computed based on a tractor purchase price of $77,000 each and a trailer purchase price of $14,000. With a packing factor of 0.54 loads per dish, the required number of tractors was expected to be 45. For storage purposes, it was expected that three trailers would be required for each tractor. Based on these assumptions, transportation capital cost was $.20 per mile.

Other transportation costs were based on those reported in Arco (Ref. 7) and adjusted for inflation based on the consumer price index. The cost per mile was then:

	Cost Per Mile
Depreciation	$ .20
Fuel	.26
Tires	.13
Maintenance	.21

Insurance, Taxes, etc.	.26
Driver	.47
	$1.53

The cost per square meter of reflective aperture was based on an average round trip distance of 533 miles. This resulted in a cost of $2.88/m^2.

3.3.5 Total Cost. The total cost of the reflective assembly is contained in Table 3.8. For 10,000 reflective assemblies per year, the cost/m^2 is $77.68. For volumes of 1,000 reflective assemblies per year, the cost/m^2 is $107.78.

TABLE 3.8
REFLECTOR ASSEMBLY COSTS

Cost by Component of Required Revenue
(Dollars Per Square Meter)

	10,000 Reflectors per year	1,000 Reflectors per year
Direct Material	$56.26	$56.55
Labor	4.41	8.22
Indirects & Consumables	6.15	14.70
G & A, Taxes & Profits	6.64	20.36
Capital Replacement	1.34	5.07
Transportation	2.88	2.88
Total	$77.68	$107.78

* Based on September 1986 dollars

3.4 Conclusion

Manufacturing and construction activities received careful consideration in the development of a final design. Conventional manufacturing processes were used whenever possible and all techniques were kept simple. This approach kept manufacturing and installation costs low and resulted in a concentrator cost that was driven primarily by material costs.

The rear support system exhibited common structural tolerances and conventional fabrication techniques. Optical element components were also fabricated conventionally. All sheet metal parts were produced continuously with repeatable processes. No special requirements were placed upon raw material for either concentrator component.

The optical panel assembly accuracy was atypical and required special techniques to be achieved. Assembly of the panels on a compound curved vacuum platen provided the high accuracies. This process was demonstrated in prototype fabrication.

To ensure overall dish accuracy, each facet could be aligned during dish construction. The attachment between the optical element and the support structure was adjustable, thereby freeing the optical elements from the inaccuracies of the rear structure. Alignment of the facets was required only once. Facets were adhesively bonded together to form an extremely stiff unit during the construction process.

These manufacturing plans were used to define portions of the overall concentrator costs. Neglecting the balance of dish components (drive, pedestal, controls, etc.) the installed cost of the concentrator was $\$77.68/m^2$ at quantities of 10,000 per year. At a lower production volume, overhead rates would be higher and the cost would rise. At a rate of 1,000 per year, the cost would be $\$107.78/m^2$.

4.0 PROTOTYPE TESTING

Key elements of the facet design were verified by testing small-scale sample facets. A full-scale prototype facet was also built and tested. This section describes the development and testing of these facets. Several basic issues concerning the panel design were resolved early in the contract by testing small facets. The feasibility of the concept was proven over the full range of curvatures. The desirability of core rigidity and the need for edge restraints were established. Different core configurations were tested and the viability of the adjustable mold was proven. These results influenced the commercial facet, and a full-scale prototype facet was developed to demonstrate the design. This prototype facet was accurate and closely followed the contour of the assembly tooling.

4.1 Prototype Sample Testing

A limited testing program was conducted after the development of a baseline concentrator to verify key elements of the design and fabrication concept. Several $1 m^2$ facets were built and tested for this purpose. The baseline facet construction is shown in Figure 4.1, and the fabrication matrix in Table 4.1. The primary variations in facet construction were adhesive compliance, core shape, core alignment, and radius of curvature.

Compliance was considered a key issue in adhesive selection for the final design. A two-part silicone, similar to the adhesive used for panel fabrication on heliostats, represented the compliant adhesive. A standard, 24-hour, structural grade epoxy was chosen for a noncompliant adhesive. The test method was to scan the reflective surface, as shown in Figure 4.2. The sample panel was adjusted with a three-point mount to minimize slope error. The laser was rotated on a gimbal at the focal point, and the reflected beam position was compared to the ideal position. The ratio of translational error of the beam centroid to focal length was defined as absolute slope error. These data points were fitted to a normal distribution to define the standard deviation of slope error.

The test on samples 1, 2, 5, and 6 was conducted immediately following construction and again in 14 days. Panels with epoxy adhesive tested the same. Samples 1 and 2, bonded with compliant adhesive, degraded by 125 percent and 25 percent respectively, after 14 days. The difference in degradation was tentatively assigned to core rigidity. The results of the basic test indicated that compliant adhesives were not a good selection for optical panel construction.

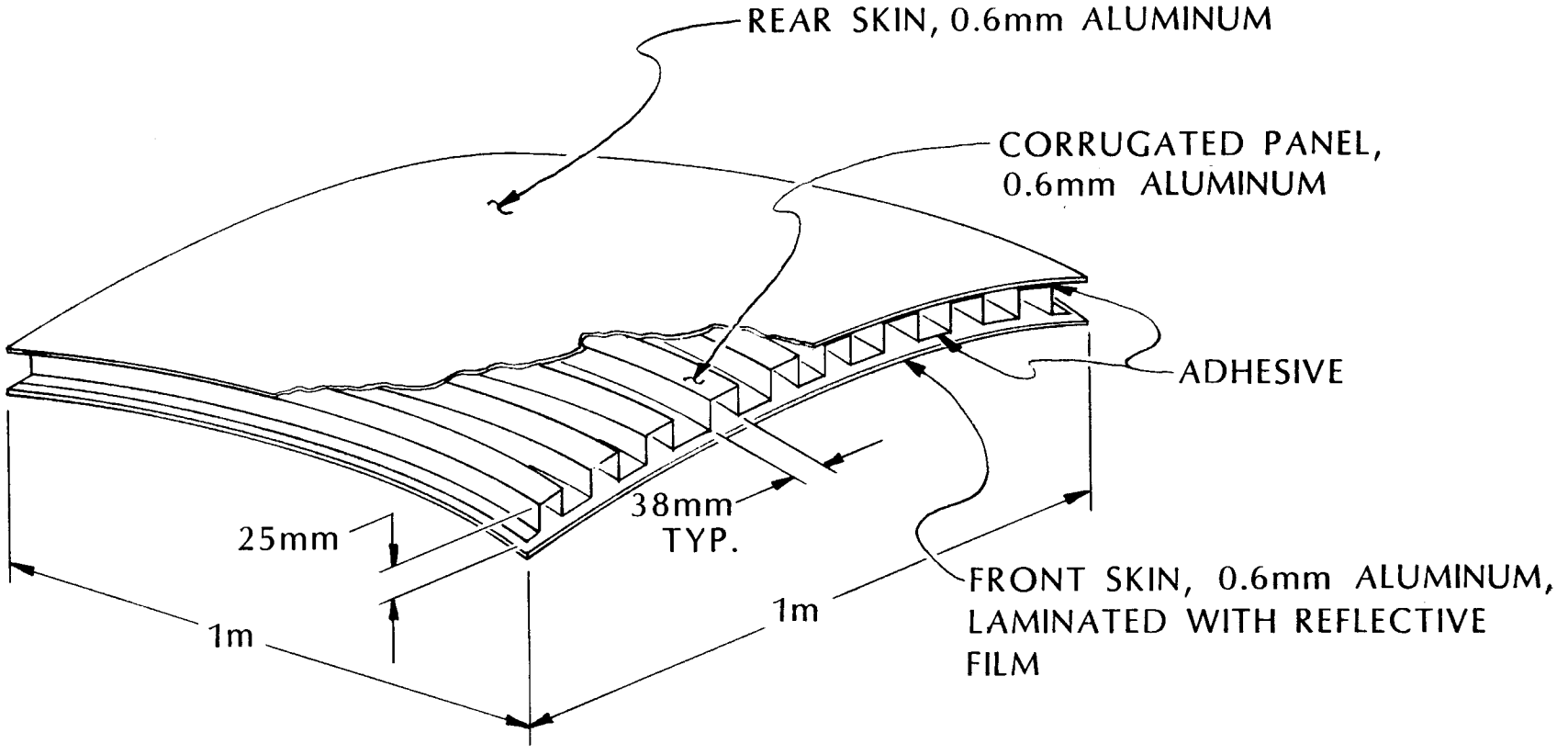

FIG. 4.1 BASELINE TEST FACET CONSTRUCTION

TABLE 4.1 SAMPLE FACET MATRIX

FACET	ADHESIVE	CORE	BOUNDARY	RADIUS OF CURVATURE (m)	INITIAL SLOPE ERROR (milliradians)
1	Silicone	Panel	Free	35	4
2	Silicone	Panel	Free	35	13
3	Silicone	Panel	Free	11	3
4	Silicone	Panel	Free	11	*
5	Epoxy	Panel	Free	11	8
6	Epoxy	Panel	Free	11	4
7	Epoxy	Hat	Restrained	11	1
8	Epoxy	Hat	Restrained	11	1
9	Epoxy	Hat	Restrained	35	1
10	Epoxy	Panel	Free	11	4
11	Epoxy	Panel	Restrained	11	1
12	Epoxy	Hat	Free	11	4
13	Epoxy	Hat	Restrained	23	1

* Error visually judged to be substantial. Testing was not conducted as fabrication process was not controlled and results could not be processed.

Two core construction techniques were investigated with these sample facets: corrugated panels and individual hat trusses. The test method for determining optical accuracy is again illustrated in Figure 4.2. Initial optical quality was the figure of merit. Samples 10 through 13 represented the best comparison of this design feature.

The comparison between corrugated panels and hats was conducted because the baseline manufacturing process for panels indicated that forming would occur about a single axis. The second axis would depend upon panel flexibility. Concern over facet chording between supports led to the test. There was no difference between the optical error of the two forming methods. The test did show some chordal facet error in all panels. This error was apparently associated with the abrupt transition in stiffness from the core turndown, rather than skin support.

Optical error in sample panel fabrication was clearly associated with the free edges parallel to the secondary axis (see Figure 4.3). Distortion in the reflective skin occurred at the free edge under the compressive load induced in fabrication. This edge was restrained by adding a single hat truss element parallel to the edge. The test method is shown in Figure 4.2; initial optical quality was defined as the figure of merit. Samples 10 through 13 again demonstrated the importance of restrained edges in the secondary axis.

The relationship of curvature and error was also explored. Each sample panel was fabricated at a single radius of curvature to simplify the testing regimen. Panels 7, 8, 9, and 13 indicated the validity of this assumption: radius and error were demonstrated to be independent. This series of tests provided two additional conclusions. The consistency of optical performance indicated the fabrication process was repeatable. This consistency was demonstrated on 2 completely separate molds. All samples at the 11-m radius were built upon a machined mold; samples at 23 and 35m were fabricated on an adjustable mold. Consequently, the viability of an adjustable mold was demonstrated.

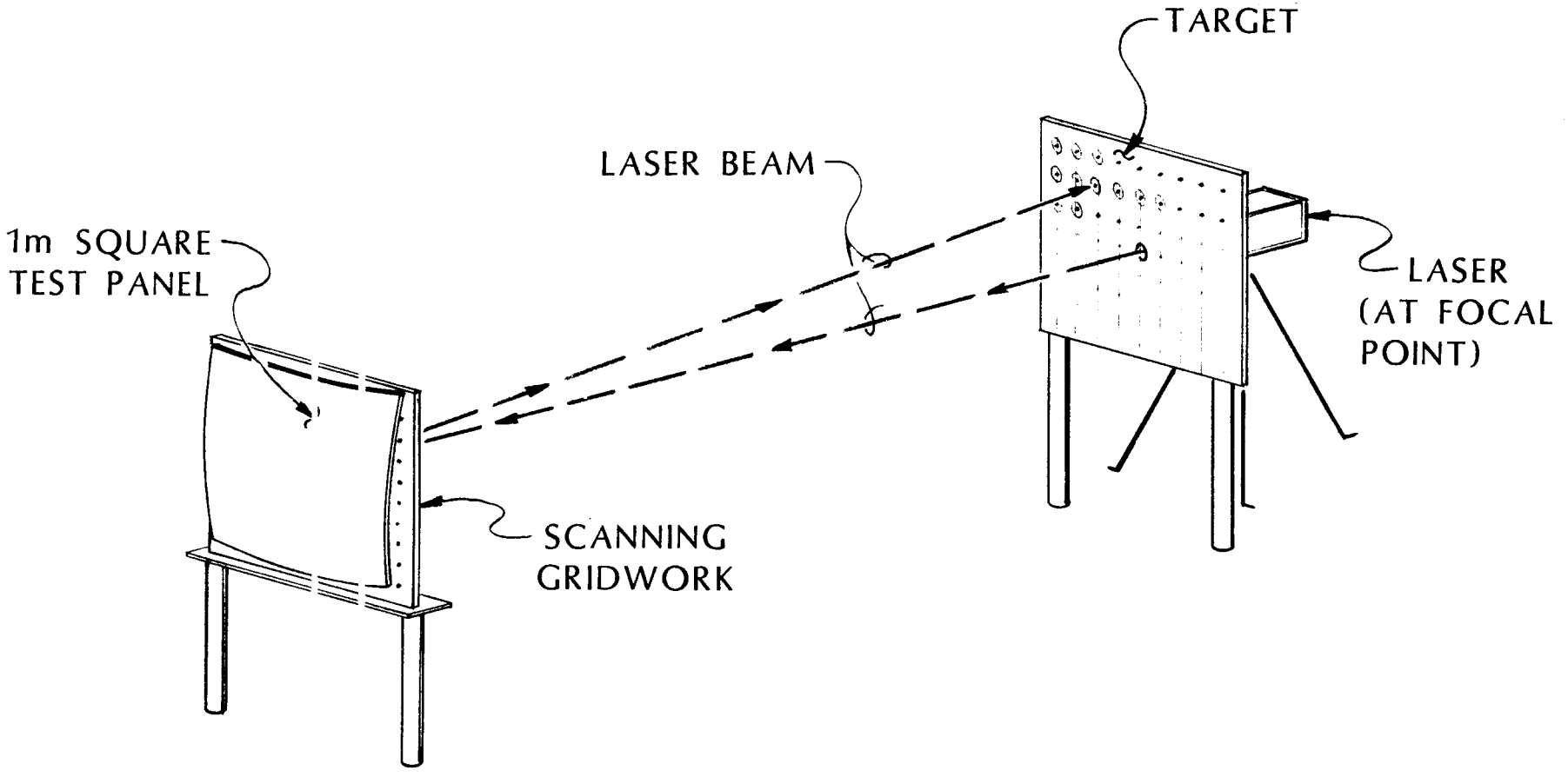

FIG. 4.2 TEST PANEL SCANNING SET-UP

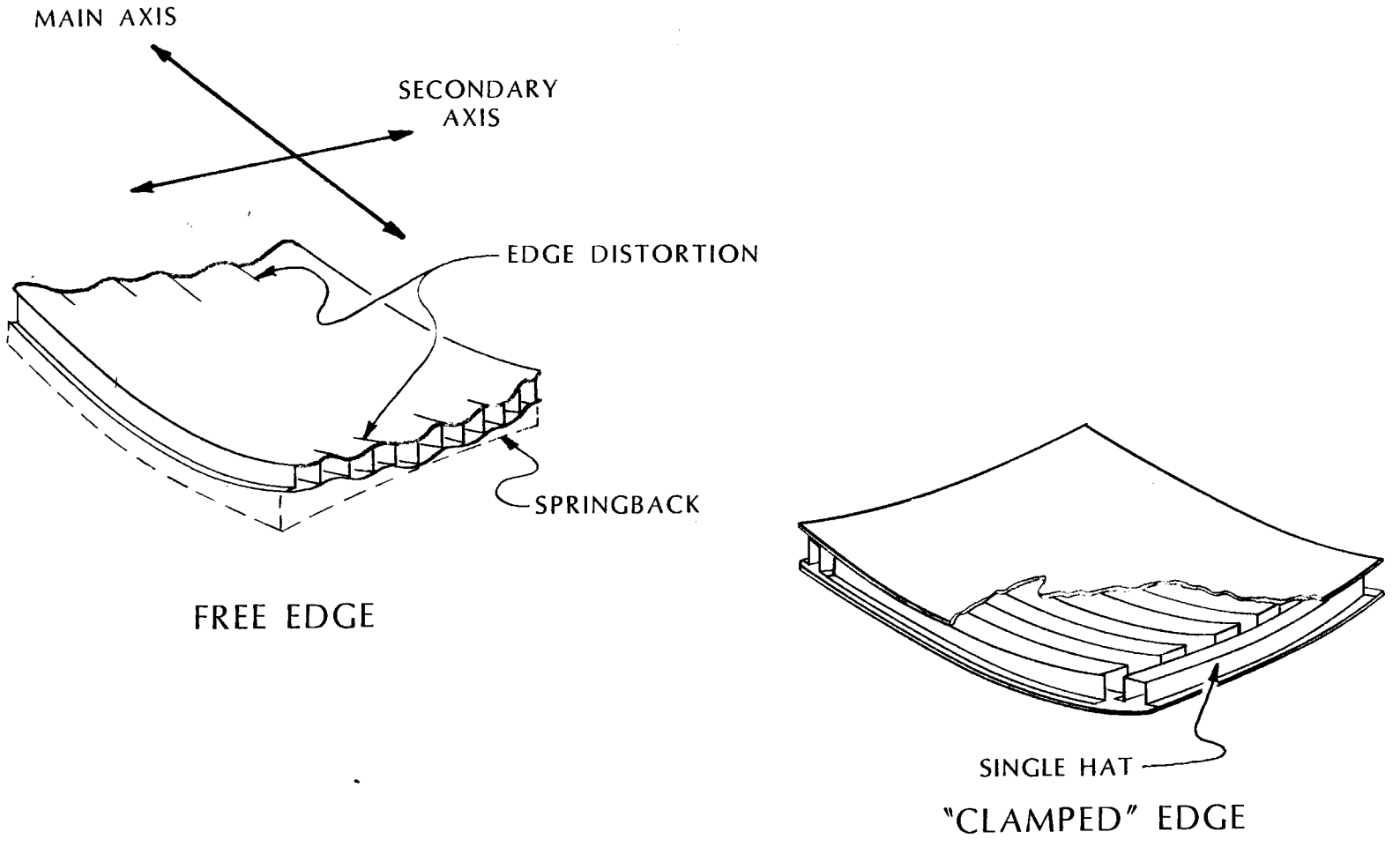

FIG. 4.3 EDGE DISTORTION AND RESTRAINT

4.2 Prototype Panel Testing

A full-sized prototype panel was fabricated following the detailed design effort. The test program was designated as a process of demonstration for all key fabrication techniques and performance issues associated with a single facet. The test required adjustment of the contoured tool, component fabrication, petal assembly, and shape verification.

The key tools used for this test included coordinate data measurement equipment optimized to determine surface slope and software for data reduction. Measurement equipment description, uncertainty, and analysis are presented in Appendix B.

4.2.1 Contour Tooling. The requirement for an accurate, contoured tool for panel assembly was discussed in a previous section. An adjustable tool or mold was developed for prototypical research to keep development costs low and increase flexiblity. Figures 3.5 and 3.6 show overall views of the tool used for this prototypical development.

A flat aluminum tooling plate was forced to assume the compound parabolic shape through 500 independently adjustable fasteners. Bending resistance was provided by attaching the fasteners to a large steel substructure with substantial sectional properties. The substructure was, in turn, fixed to a steel surface plate, 150 mm thick.

Finite element analysis indicated that a surface of acceptable quality could only be achieved if no moments were applied at the fastener. A spherical ball joint was consequently provided on both ends of each connection to avoid localized moments. This release at each connection also allowed the load to be introduced normal to the plate surface.

The technique for adjustment required a displacement probe placed at or near the fastener. The actual height was available to the operator, the theoretical height was known, and a turnbuckle was turned to match the displacements (see Figure 4.4). A fraction (150) of the fasteners was selected for initial passes. Adjustment proceeded from center to edge in 20 percent increments. The remaining fasteners were adjusted to eliminate local distortion. Adjustment was subsequently fixed with jam nuts.

Slope data were taken after the mold adjustment; this information is presented graphically in Figure 4.5. The graphic presentation was accomplished through superimposition of the error file on a perfect shape. This approach was selected to allow the error to be amplified and hence, visible.

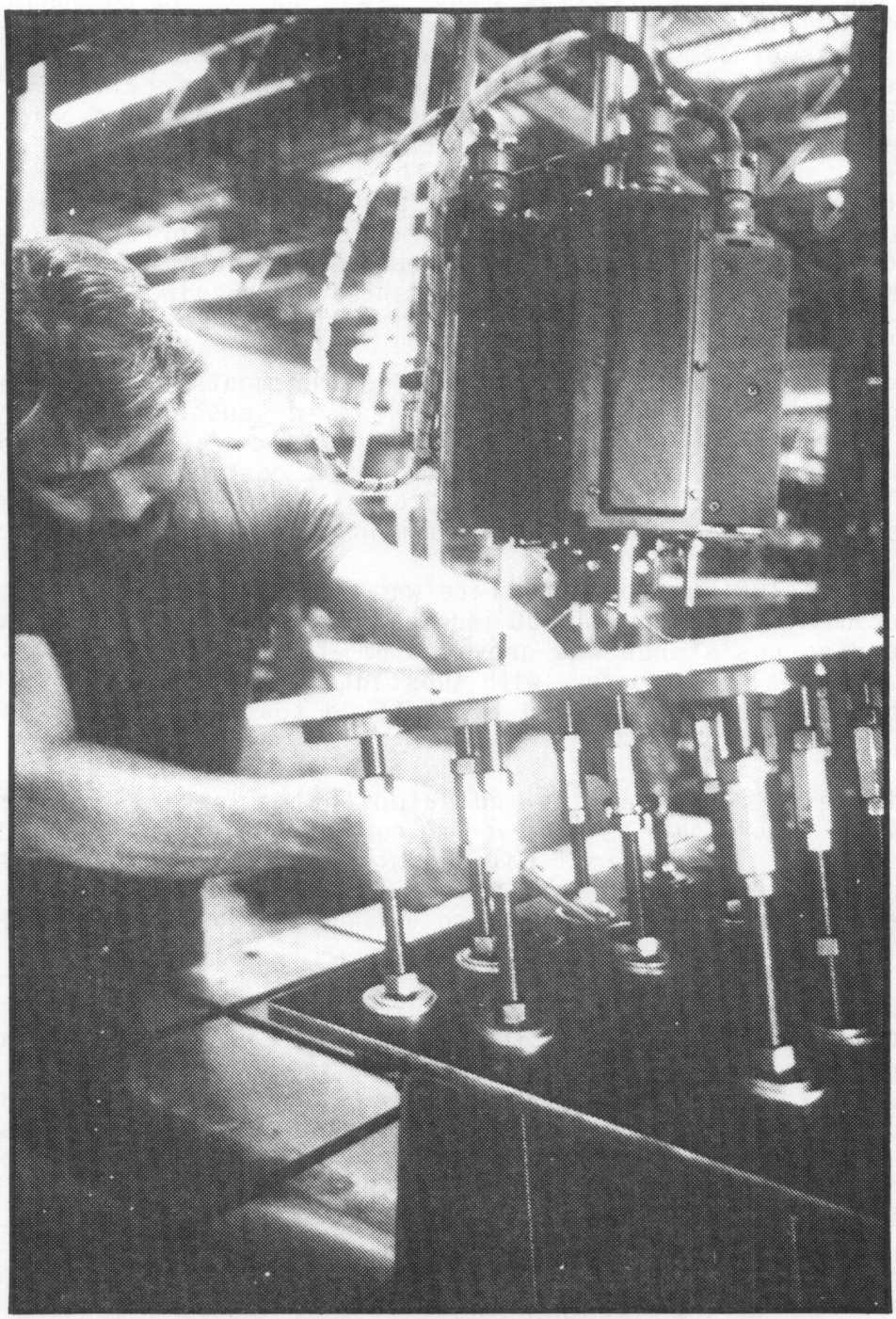

FIG. 4.4 FASTENER ADJUSTMENT

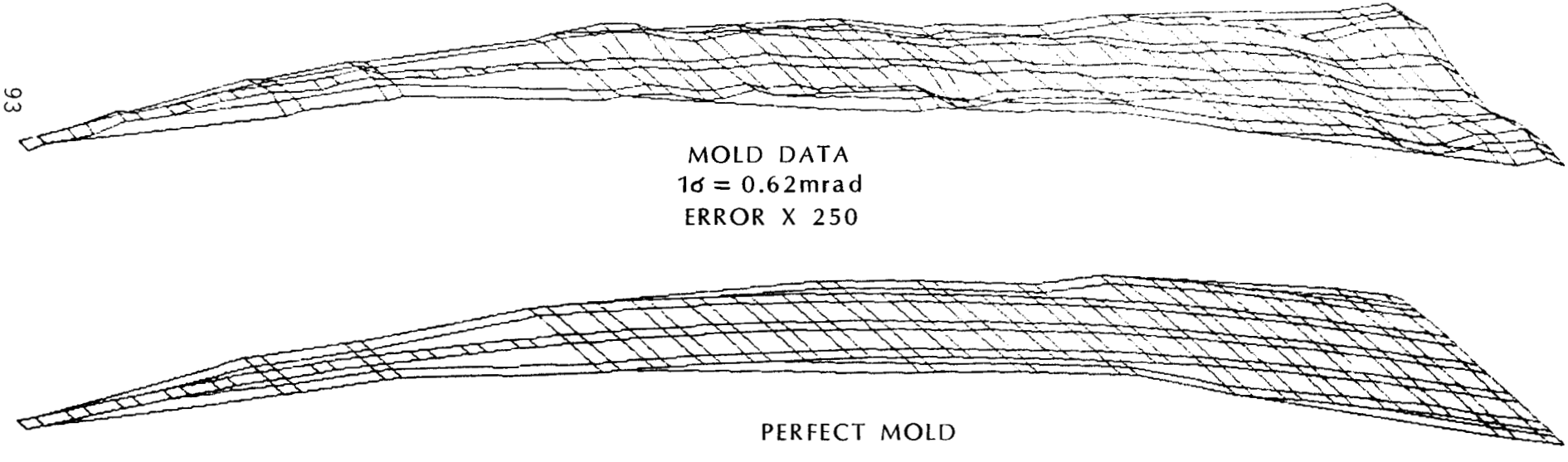

FIG. 4.5 ADJUSTABLE MOLD SURFACE

The area weighted slope error for the mold was 0.60 mrad (-0.24 mrad uncertainty) with the majority of the error occurring at the edge and a small wave at the wide end. Further adjustment was abandoned due because of the proximity of accuracy and uncertainty.

4.2.2 Optical Panel Components and Geometry. Panel components were similar to the final design, though some modifications were required to implement the prototype within contractural limitations. Individual hat-shaped trusses were used rather than corrugated panels; a slotted channel replaced the rolled channel; and 0.8-mm aluminum stock was used for the skins. The first 2 variations were implementd because of the limited power available to existing pyramid bending equipment. Prototype sample fabrication, described in the previous section, indicated that no significant error or accuracy was introduced by minor modification of core geometry (panel versus hat, see Figure 4.6). The slotted channel required a parabolic bend, which precluded use of outside equipment. Parabolic roll bending was implemented accurately on smaller sections by SKI in previous development efforts. Consequently, the process was not in question and the expedient fabrication process shown in Figure 4.7 was adopted.

The final variation, skin thickness, was altered only because 0.6-mm stock in 1.5-m widths was unavailable in small quantities. The importance of skin preform increases with thickness; spring back error tends to increase as well. The slightly thicker skin apparently did not have a substantial impact in this area, because no significant elastic recovery occurred in the prototype facet.

The geometry of the prototype optical panel is shown in Figures 4.8 and 4.9. This panel was dimensionally identical to the final design.

4.2.3. Results. Slope data on the fabricated gore were generated through direct profile measurement, with the equipment and data software discussed in Appendix B. The approach was identical to measurement of the contour tooling, and the location of measurements was correspondent. The graphical representation of the gore is presented in Figure 4.10 at different magnification. The one sigma slope deviation was 1 mrad (uncertainty 0.24 mrad).

The mold and gore are displayed at the same error magnification in Figure 4.11. Of interest was the basic reproduction of the error pattern from the mold to the gore. Errors occurring in a similar place were of identical sign, though they were magnified in the facet. This pattern reproduction indicated that petal performance was a function of tool accuracy. The low magnitude of slope deviation also indicated that tool error amplification

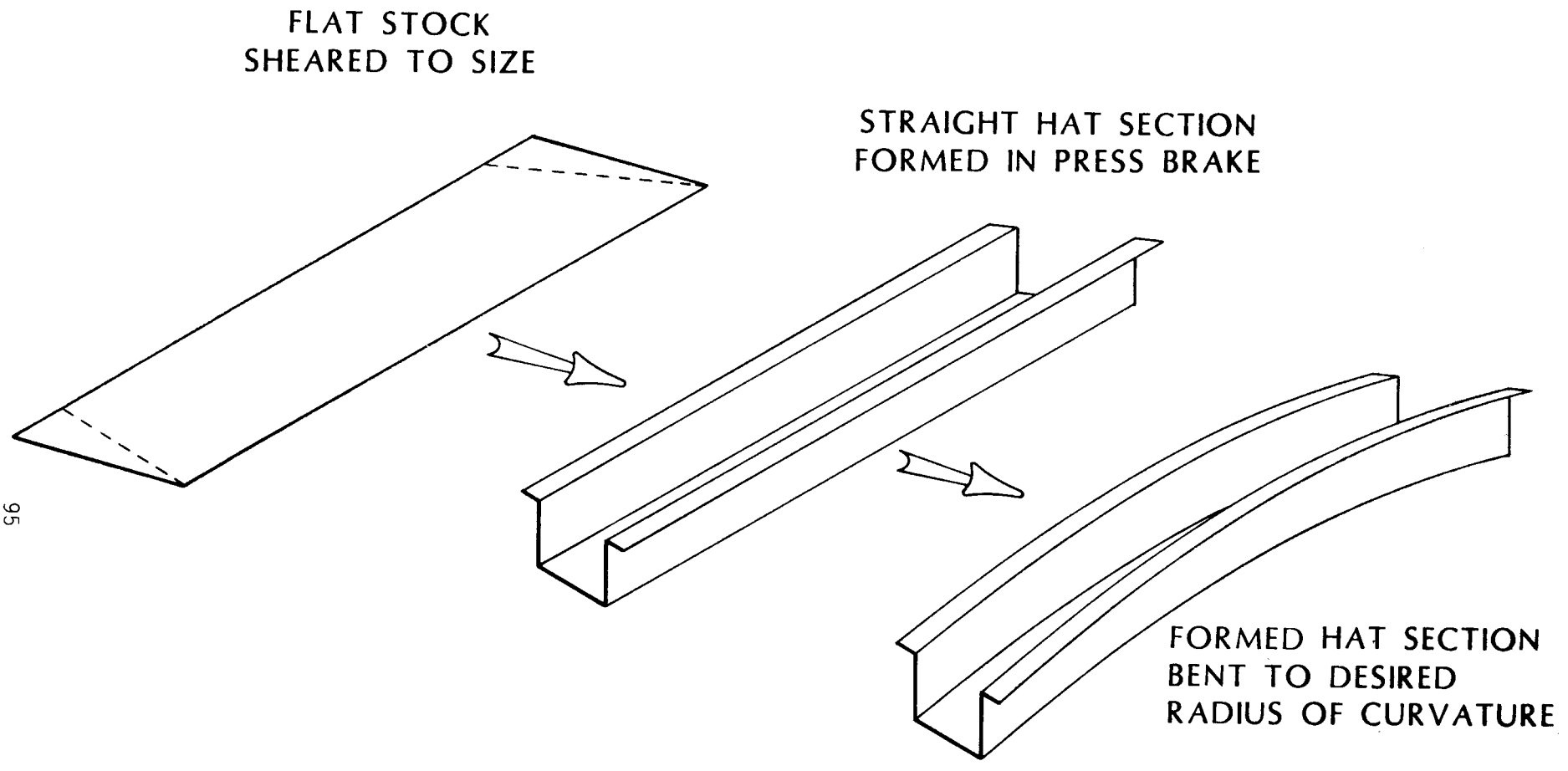

FIG. 4.6 PROTOTYPE OPTICAL ASSEMBLY HAT SECTION PRODUCTION

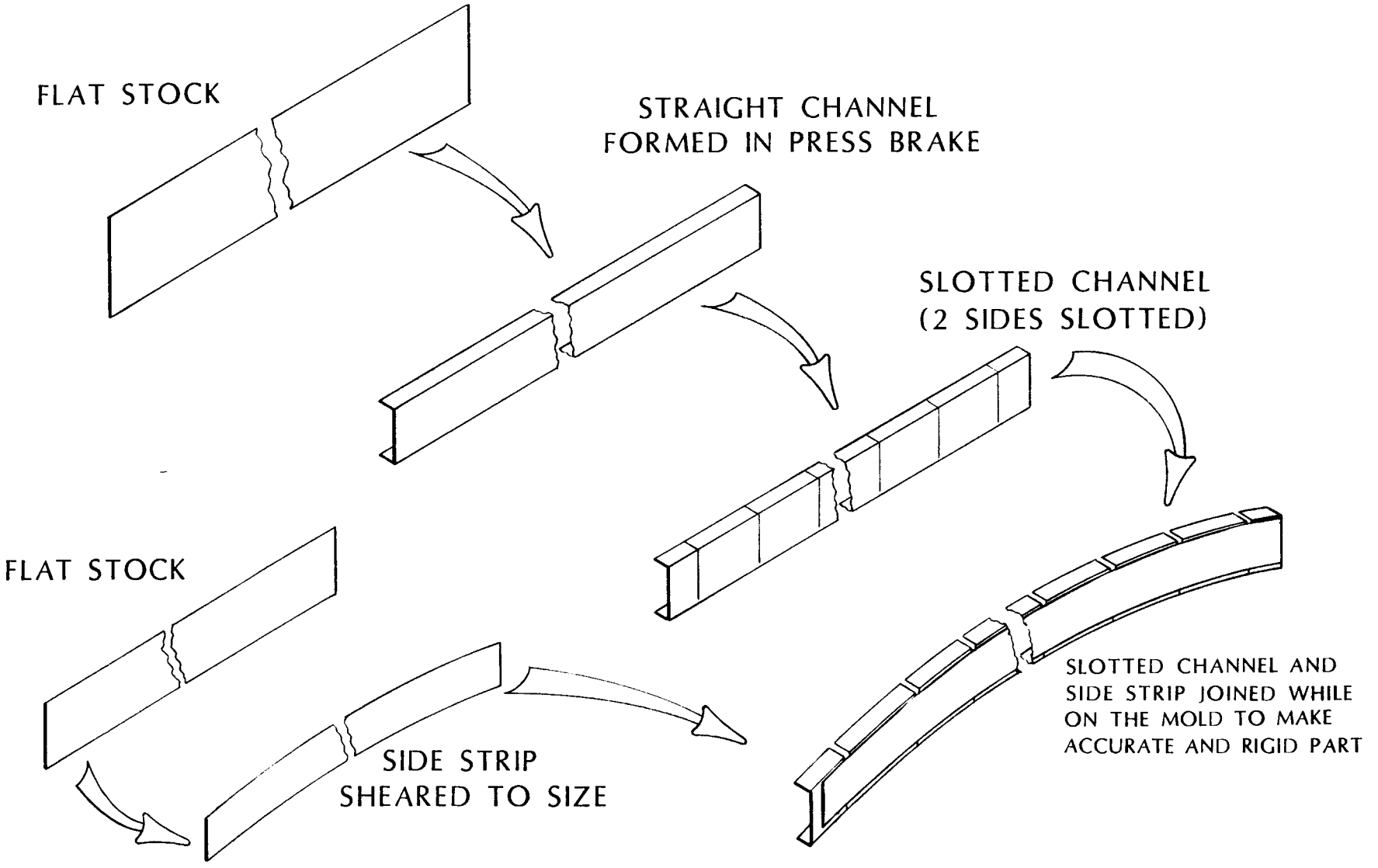

FIG. 4.7 PROTOTYPE OPTICAL ASSEMBLY SIDE CHANNEL AND STRIP PRODUCTION

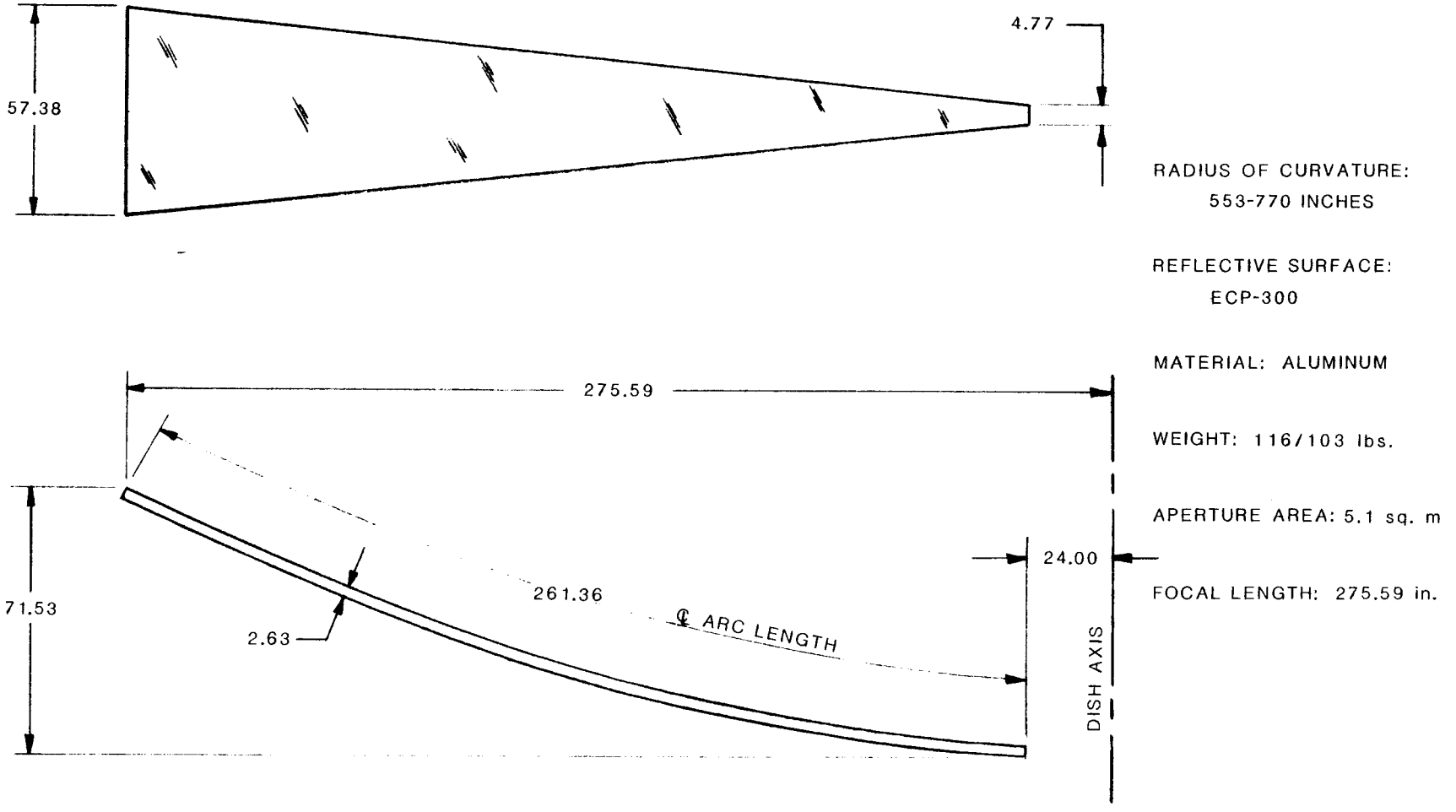

FIG. 4.8 PROTOTYPE OPTICAL ASSEMBLY

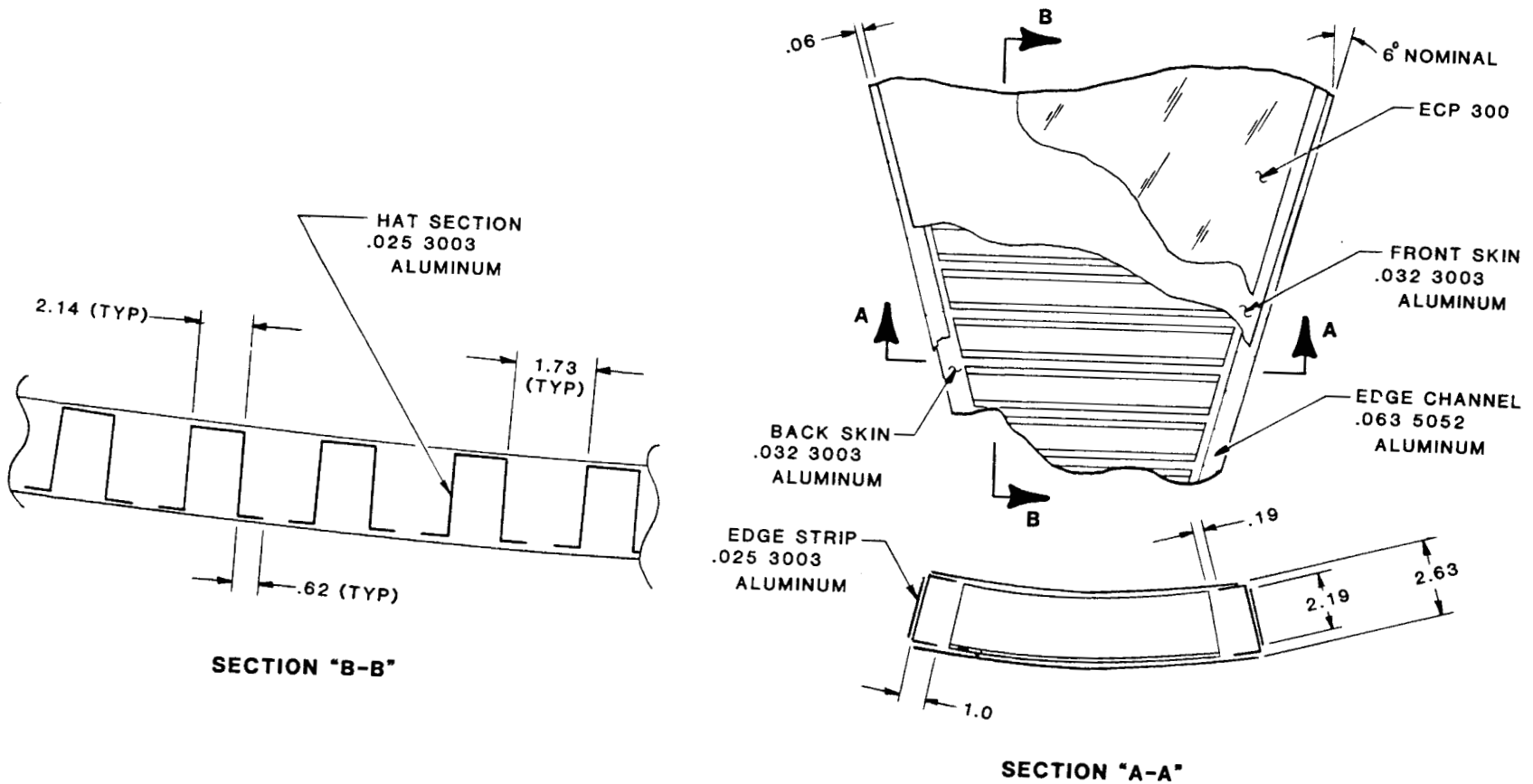

FIG. 4.9 PROTOTYPE OPTICAL ASSEMBLY DETAILS

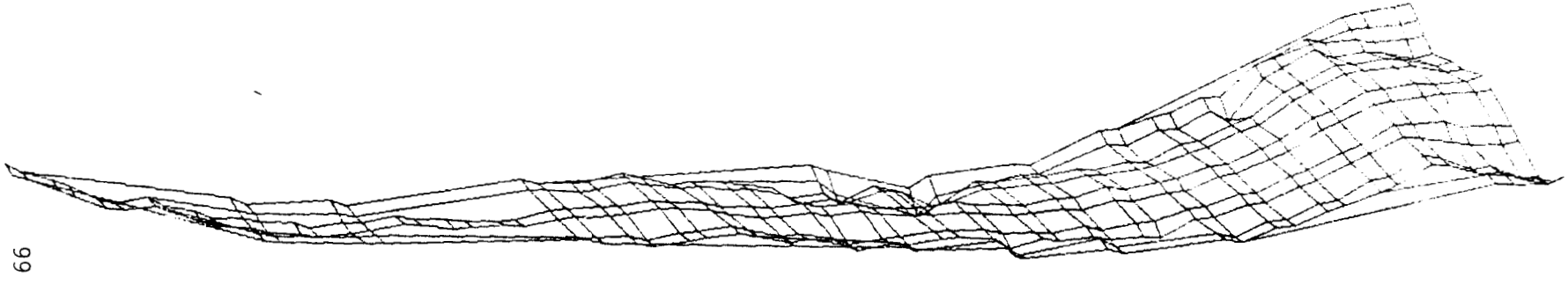

GORE
1σ = 1.06mrad
ERROR X 250

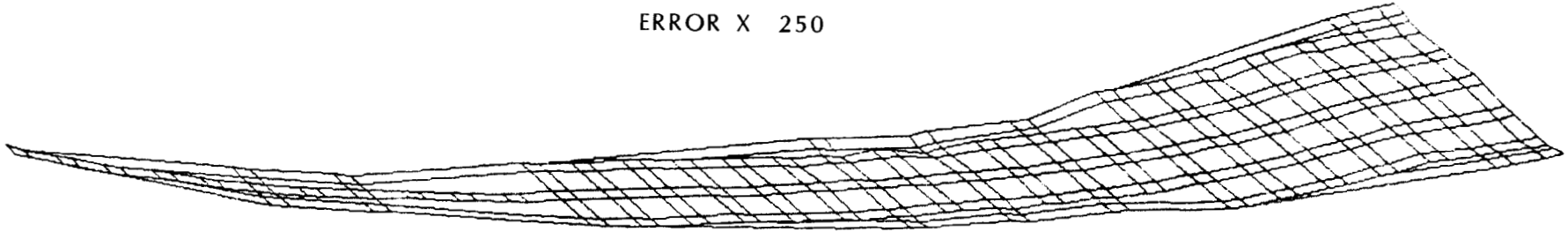

GORE
1σ = 1.06mrad
ERROR X 50

FIG. 4.10 GORE SURFACE

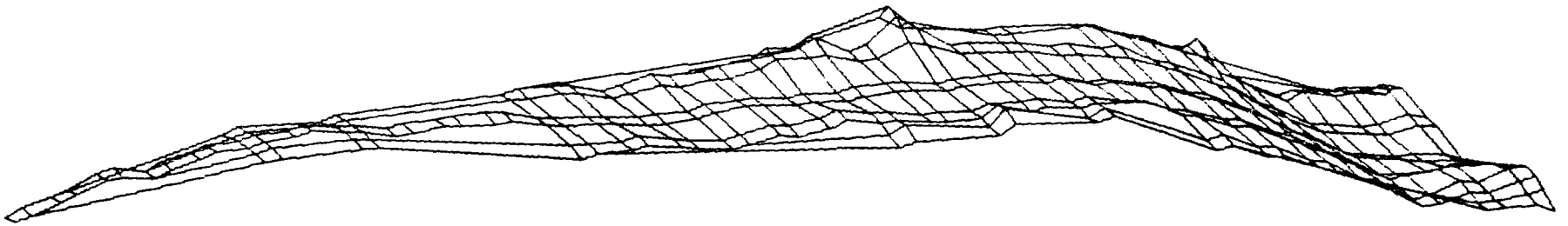

INVERTED GORE
1σ = 1.06mrad
ERROR X 250

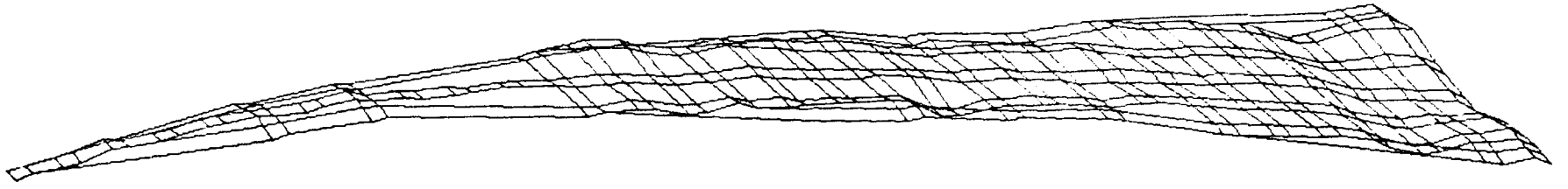

MOLD DATA
1σ = 0.62mrad
ERROR X 250

FIG. 4.11 MOLD AND GORE SURFACES

was within an acceptable range. The prototype petals fabricated are shown in Figures 4.12 and 4.13.

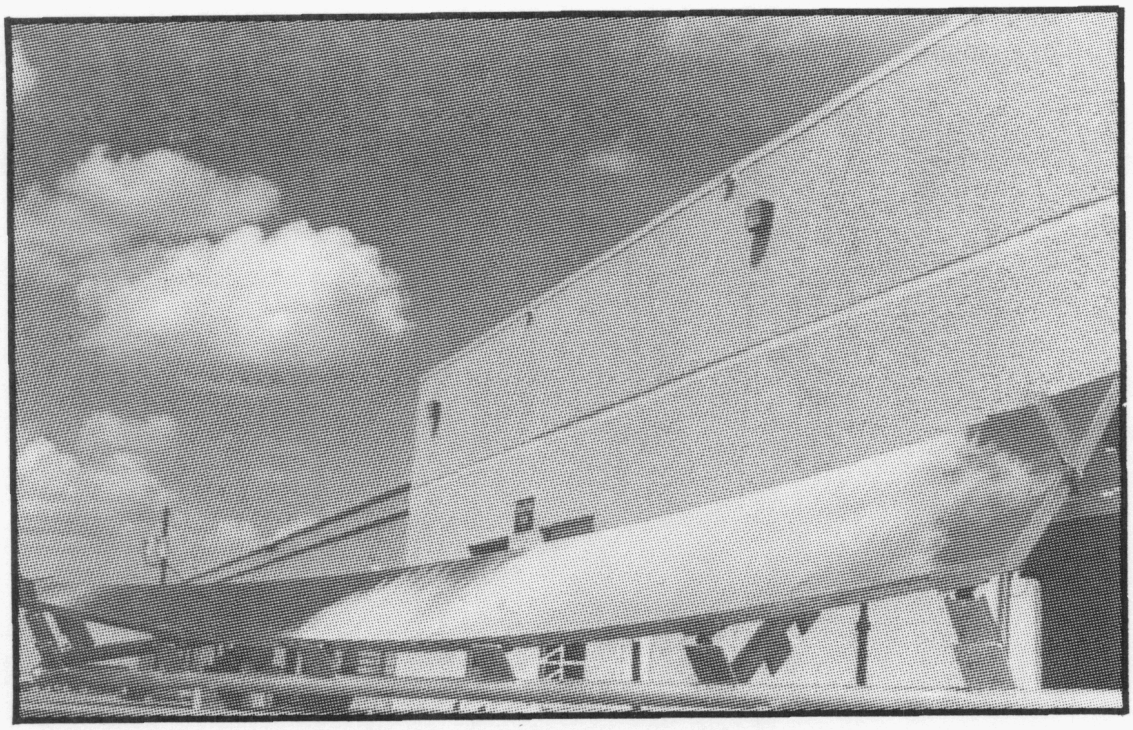

FIG. 4.12 PROTOTYPE FACET

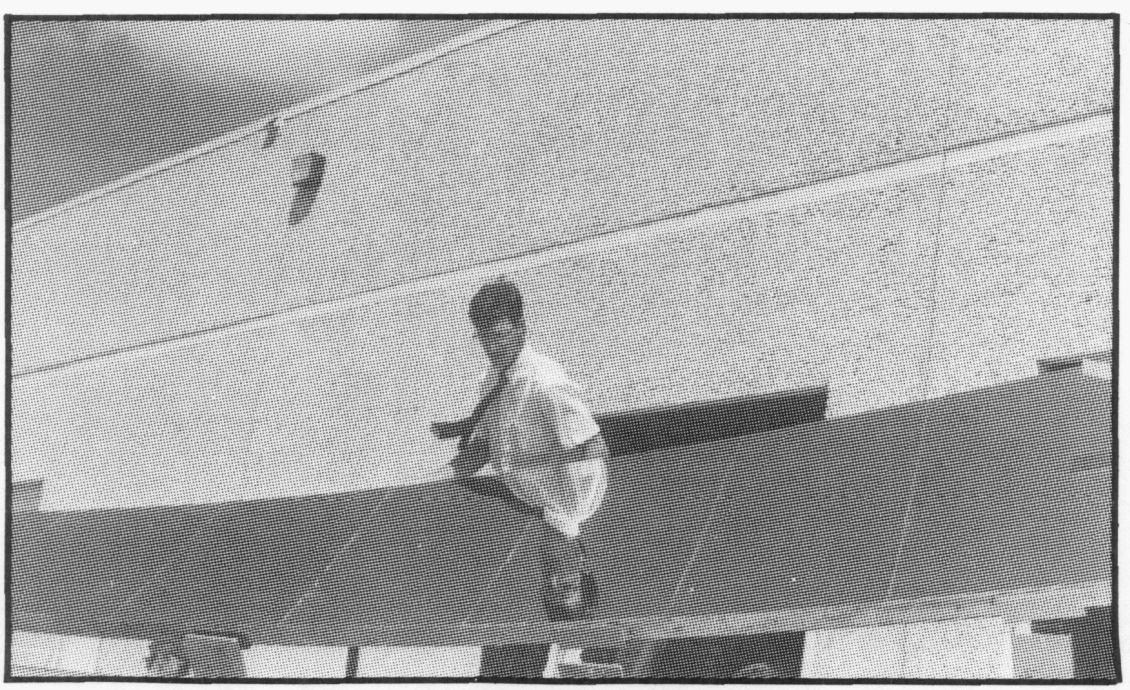

FIG. 4.13 PROTOTYPE FACET DETAIL

4.3 CONCLUSION

The fabrication of a full-scale prototype facet with excellent surface accuracy demonstrated several key features of the proposed design:

Panel slope errors of 1 mrad or less could be achieved and were demonstrated with sandwich panel construction on an accurately contoured assembly tool.

Panel accuracy was primarily a function of tool accuracy.

Stresses induced in fabrication did not result in significant error from elastic recovery (spring-back).

These conclusions reinforce the performance predictions made in the design development. The systematic definition of existing error indicated that the assembly process is repeatable.

5.0 CONCLUSION

This report completes the requirements for Phase I of the point-focus concentrator contract. The design of the optical elements, rear structure, and power conversion assembly (PCA) supports, along with the construction and analysis of a reflector assembly, were accomplished during this phase. Design of the pedestal, drive, and other components, and construction of a prototype concentrator are planned for later development.

The Phase I effort resulted in a structurally efficient, low-cost dish design and a full-scale optical element that are very accurate.

The optical assembly exhibited a large stiffness-to-weight ratio; optical accuracy was maintained under operating loads. This stiffness was achieved by connecting each petal through a joint capable of load transfer. The reflective surface acted as a continuous plate. Survival loads were transferred through a secondary rear structure, thus alleviating the optical surface from requirements for strength as well as stiffness. Careful balance of stiffness and restraint in the connection between the two structures minimized localized loads and deformations. The total reflector assembly weight was kept below 60 lbs/m^2.

Manufacturing processes were a fundamental part of the design. Conventional manufacturing processes were widely used, and scrap losses were minimized in an effort to demonstrate a producible assembly. Adjustment was provided to eliminate potential error in construction. The dish was made rigid following construction; subsequent adjustment was not required in spite of the oscillatory load environment. The total costs for the concentrator ranged from \$78 to $108/m^2$ at annual production rates of 1,000 and 10,000 assemblies, respectively.

An innovative approach was taken to the PCA support design that allowed quick emergency defocus and ground level receiver maintenance. The PCA was supported on three hinged struts. One strut retracted upon power failure or receiver emergency and swung the PCA away from the focal point. This avoided the requirements for fast auxiliary power response. The strut could also be mechanically lowered to bring the PCA close to the ground for easy maintenance access.

A full-scale optical petal was fabricated to demonstrate the design concept. The optical accuracy of the panel was exceptional; slope error was kept to 1 mrad (one sigma, 0.24 mrad uncertainty).

The optical panel was assembled on an adjustable mold and its accuracy was determined with coordinate data measurement equipment optimized for slope definition. The adjustable mold

represents a new, low-cost approach for fixturing optical assemblies. The measurement system had the capability of directly mapping the surface of large facets and accurately determining their inaccuracies.

To continue the progress of this point-focus program, final design of the remaining components should be accomplished, followed by a full-scale demonstration of the concentrator.

The combination of structural design, producibility, and optical accuracy resulted in a low-cost, high-performance approach to point-focus technology.

6.0 REFERENCES

1. L. D. Jaffe, Optimization of Dish Solar Collectors With and Without Secondary Concentrators, DOE/JPL-1060-57 (Pasadena, California: Jet Propulsion Laboratory, California Institute of Technology, May 15, 1982).

2. Optical Performance Software, DOE/CS/35348-T1 (Minneapolis, Minnesota : Honeywell, Inc.).

3. Solar Kinetics, Inc., Design Specification for a Point-Focus Solar Concentrator, Contract #21-3695 (Albuquerque, NM: Sandia National Laboratories, 1985).

4. E. J. Roschke, Wind Loading on Solar Concentrators: Same General Considerations, JPL-1060-66 (Pasadena, California: Jet Propulsion Laboratory, May 1, 1987).

5. E. Cohn, Calculation of Wind Forces and Pressures on Antennas, (New York, New York: Annals New York Academy of Sciences, Volume 116, 1964).

6. R. J. Roark and W. C. Young, Formulas for Stress and Strain, 5th Edition, (New York, New York: McGraw-Hill, 1975).

7. Second Generation Heliostat Development for Solar Central Receiver Systems, Final Report, SAND 81-8178 (Bechtel National, Inc., San Francisco and Booz-Allen and Hamilton, Inc., Cleveland, Ohio: Northrup, Inc., 1981).

APPENDIX A

SLOPE ERROR AND SURFACE CONTOUR MEASUREMENT

A measurement system was developed to characterize the facet and mold surfaces. This system mechanically measured both the slope and X, Y, Z position of a surface. The large capacity of the system (7.5 x 2 x 1.5 m) allowed characterization of full-scale facets. Uncertainty was 0.24 mrad and data could be presented numerically or graphically.

A.1 Purpose

Parts that were assembled on molds to demanding tolerances, such as optical facets, were sensitive to subtleties in design and construction. Adhesive cure, cure pressure, amount of adhesive, cure time, method of fixturing, and fit tolerance could all have had a significant impact on the optical accuracy. These items had to be defined and held within bounds in order to achieve precise optical facets. Definition of such items could be determined empirically. That is, facets could be assembled and analyzed to provide feedback on the next part's design and method of construction. Precise feedback was essential for improvement. The coordinate data measurement system (CDM) provided this feedback.

The measurement system allowed characterization of the mold facets. By comparing of the facet and the mold, errors could be categorized as systematic or random. Errors in the surface of adjustable molds were removed with feedback for adjustment. The CDM could also provide the means to adjust the mold away from the theoretical shape (windage) to accommodate systematic facet error.

A.2 Description

The coordinate data measurement system was designed to provide a dual output: displacement and slope. The displacement provided the axial location of any point on the optical element surface with respect to a global Cartesian coordinate system. The global system that was used corresponds roughly to a radial (X) and tangential (Y) system, with Z defined by the right-hand rule. The CDM is shown in Figure A1; the X-axis runs the length of the surface table, the Y-axis its width; the Z-axis is vertical.

Translation was provided along precision ground rails with linear bearings in the X- and Y-axes. Translation in the Z-axis was provided by a driven ball screw. The screw path was stabilized with linear bearings and precision rails; the screw nut was doubled and opposed to eliminate backlash. Optical encoders provided all global displacements. The Y- and Z-axes were provided with linear optical encoders that provided for the full carriage motion. The X-axis was furnished with a friction wheel and rotary encoder.

The CDM provided direct slope measurement through the use of four additional linear encoders mounted on the tip of the Z screw (see Figure A2). These encoders operated independent of the global displacement measurements; their accuracy was largely dependent upon their relationship to one another and the slope of their mounting plate. The profile measurement itself was largely uncoupled from global displacement error. This approach was taken to limit the expense associated with extremely large volume precision measurement. The encoder displays are shown in Figure A3. The upper four displays represent the displacement of each of the surface encoders.

These four surface encoders were mounted on a 75-mm square pattern. The ball screw was lowered until all four points contacted the surface. The relative displacement of these encoders provided two triangular, arbitrarily located planes from which surface normal could be calculated. Errors with a characteristic dimension substantially less than 75 mm could not be measured with the same precision available to larger patterns.

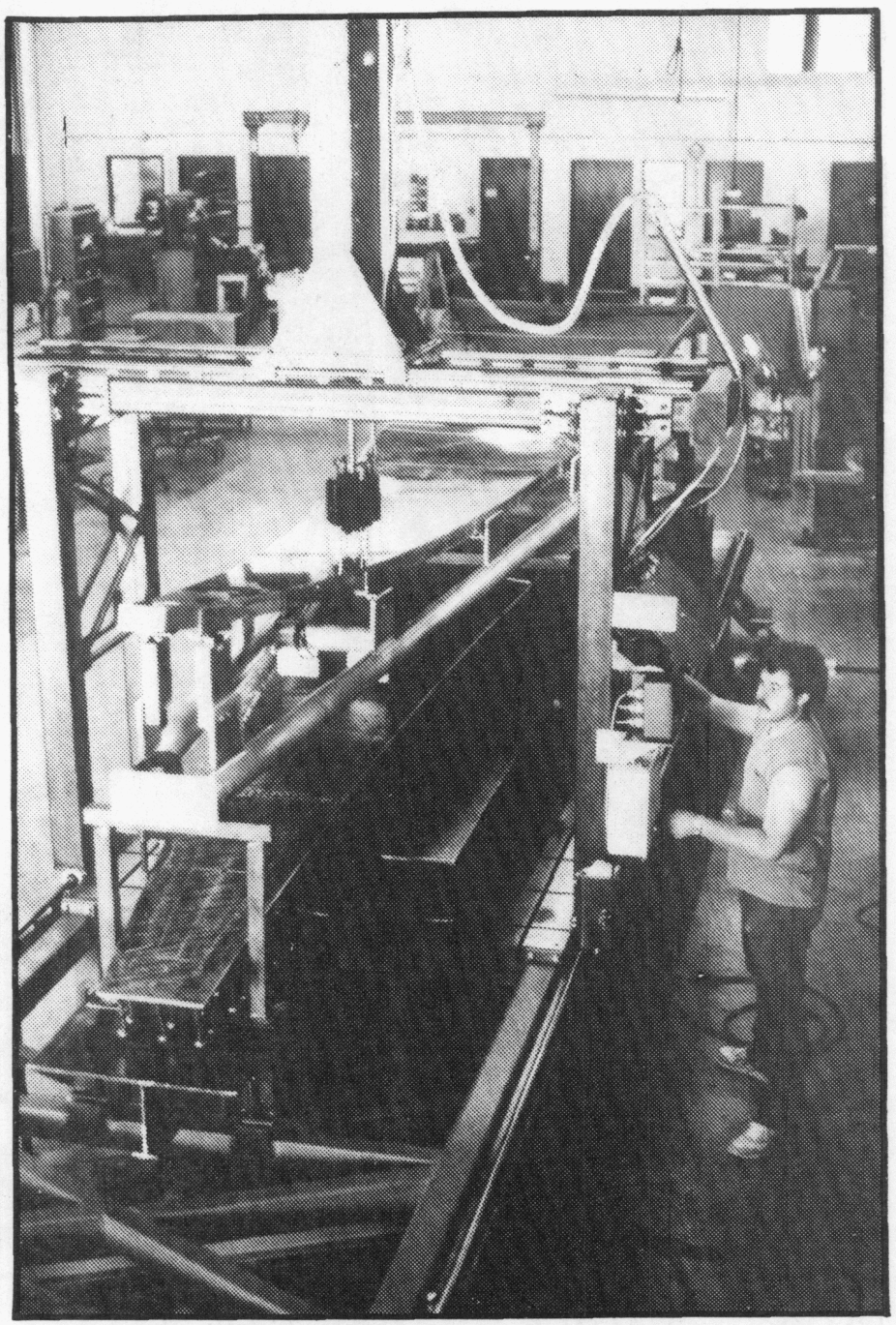

FIG. A1 COORDINATE DATA MEASUREMENT SYSTEM

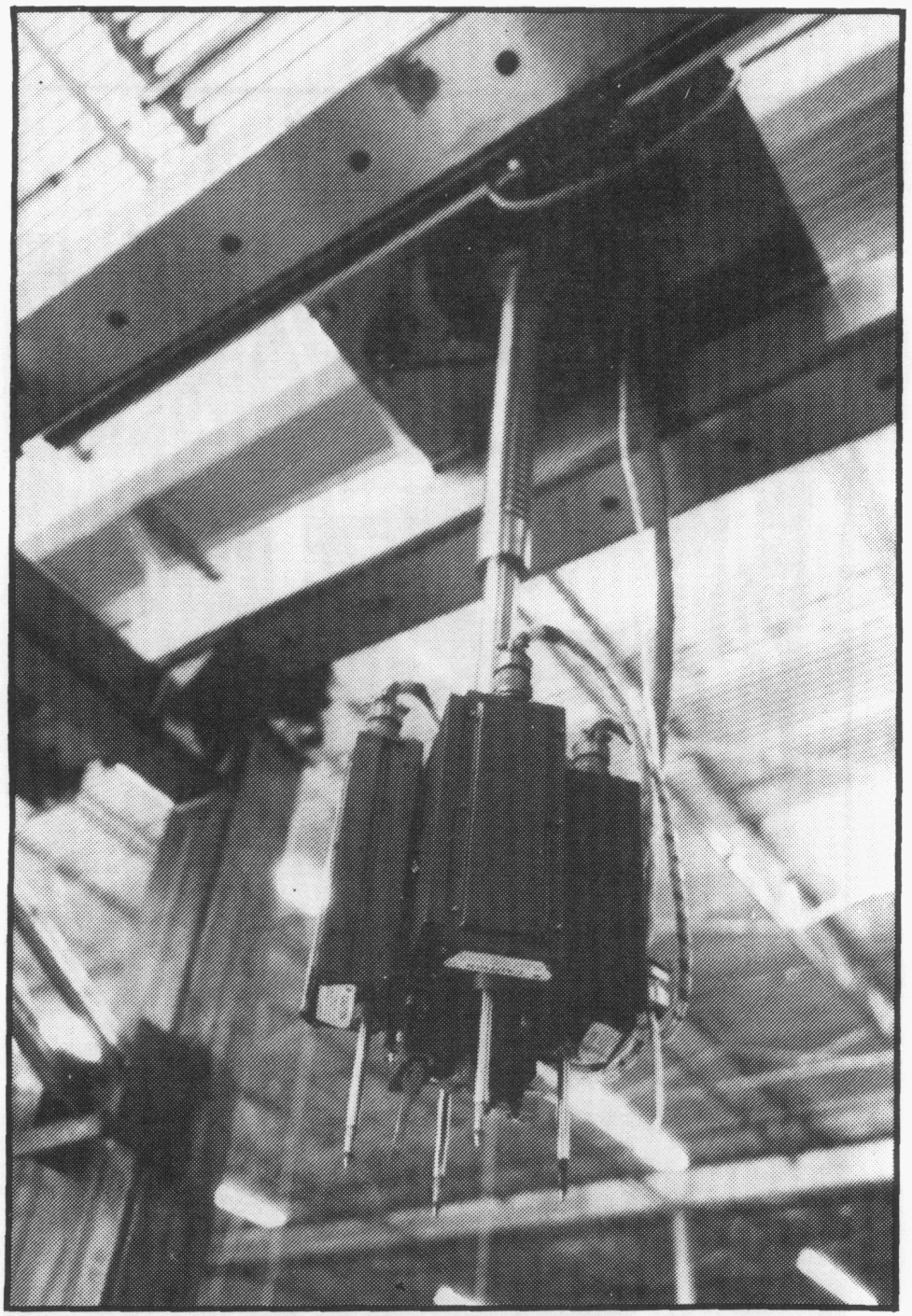

FIG. A2 SURFACE ENCODER ASSEMBLY

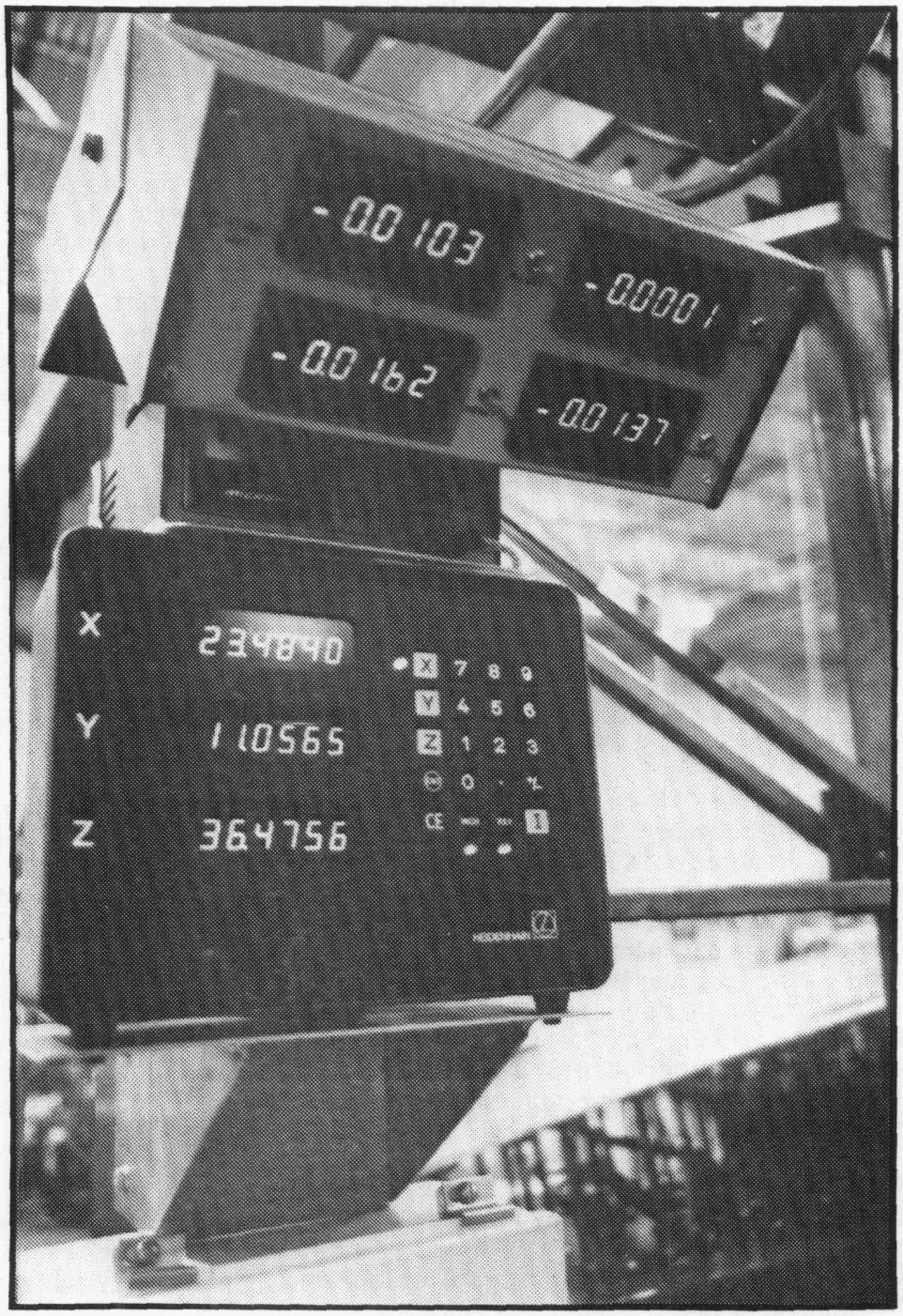

FIG. A3 ENCODER DISPLAYS

A.3 Accuracy

As part of the design of the measuring system, an uncertainty analysis was performed. This analysis identified sensitive parameters, gave component performance constraints, and provided an estimate of overall system performance. Upon completion of the construction, the system was calibrated and actual uncertainty values were assessed.

A3.1 Initial Predictions.

The uncertainty analysis performed during the design of the measuring system grouped the sources of error into the following four catagories: structure, transducer, environment, and data acquisition (Table A1). Structural error included height variation of the rails, sag due to transient loads, rail alignment error, and others. Transducer error included spacing of surface encoders, encoder inaccuracies, and similar errors. Error due to thermal expansion was included in the environmental category. Data acquisition error included error of electrical equipment.

Table A2 provides the predicted uncertainty for each category and gives the total estimated uncertainty for the system. The primary translation error was associated with the structure. The primary slope error resulted from transducer error and data acquisition. The total error was an RMS value of each independent error source. The predicted slope error was 0.4 mrad and a maximum of 0.3 mm in translation error. These values, as well as all presented error values, were reported as one standard deviation.

To determine if these values were acceptable, their impact on determination of the slope accuracy of a facet was assessed. Slope accuracy is simply the difference between the actual slope of an object and its theoretical slope. The actual slope of the surface is measured semidirectly with an accuracy of 0.4 mrad. The theoretical slope of a surface is a function of the X and Y position, but varies slowly for large errors in translation. For example, an error of 1.4 mm in the X-axis results in only 0.1-mrad error in the theoretical slope determination. On this basis, the uncertainty in the translations was judged to be tolerable, and close attention was given to reduction of the slope uncertainty.

A3.2 Calibration.

Calibration of the measurement system was accomplished with a series of tests against known standards. The results indicated that the slope and vertical displacement uncertainty were better than predicted.

One source of significant improvement over the predicted values was in the data translation. The encoders chosen for the

TABLE A1

SOURCE OF ERRORS

I. STRUCTURE

1. HEIGHT VARIATIONS
2. HEIGHT DIFFERENCE BETWEEN RAILS
3. CAMBER OF RAIL
4. SAG DUE TO TRANSIENT LOAD
5. "SQUARENESS" OF RAILS
6. BALL SCREW DISTORTION

II. TRANSDUCER

1. SURFACE ENCODERS (SE)
   a) "NON-SQUARE" MOUNTING PLATE
   b) SE SPACING ERROR
   c) SE CALIBRATI N ERROR
   d) SE "ROUNDED-TIP" ERROR
2. POSITION TRANSDUCERS
   a) X-AXIS
   b) Y-AXIS
   c) Z-AXIS

III. ENVIRONMENT

IV. DATA ACQUISITION

1. SIGNAL TRANSLATION
2. ANALOG TO DIGITAL CONVERSION
3. DATA TRUNCATION

TABLE A2

INITIAL UNCERTAINTY PREDICTIONS

SOURCE	x (mm)	y (mm)	z (mm)	Ox (mrad)	Oy (mrad)
STRUCTURE ERROR	0.22	0.20	0.05	.19	.19
TRANSDUCER ERROR	0.20	0.08	0.02	.22	.22
ENVIRONMENT ERROR	0.12	0.02	0.02	-----	-----
DATA ACQUISITION ERROR	0.005	0.005	0.02	.27	.27
DATA UNCERTAINTY	0.33	0.22	0.08	.40	.40

measuring system were completely digital and, therefore, their electronics were not affected by temperature change, as are analog devices. For this reason, the actual data translation error became insignificant.

The measurement system recorded slope independent of X, Y, Z placement; uncertainty in translation had no direct impact on slope. The following description of slope uncertainty is, therefore, separated from the description of translation error.

A3.2.1 Slope Calibration. Slope uncertainty was determined with three tests. The first test was used to assess the error of each surface encoder. The second identified the error caused by rocking of the encoder assembly, as it moved from point-to-point. The third test isolated the uncertainty of slope measurements taken at any one location.

Gage blocks were used to judge the accuracy of each surface encoder. The surface encoder assembly was lowered onto a box square until the four probes contacted. Gage blocks were placed between the encoder tips and the box square and data were recorded at each end of travel. The accuracy of the gage blocks was +0.25, -0.15 microns. The data indicated that all of the surface encoders were accurate to 2.5 microns, which was the resolution of the encoder displays and was negligible in the uncertainty determination.

The second test was to identify slope uncertainty due to rocking of the surface encoder assembly. Rocking had two primary sources: rail height differences and canting of the ball screw nut. To combine these two effects, a level surface was placed under the surface encoders. The ball screw was raised and lowered through several revolutions of the nut, with the surface encoders in contact with the surface. Data were recorded at many heights and the process was repeated at several random locations. The surface (a box square) was leveled to within 0.01 mrad using a machinist's level. Uncertainty defined by this test was calculated to be 0.21 mrad between encoders A and B, 0.06 mrad between B and C, 0.20 mrad between C and D, and 0.07 mrad between D and A. The four surface encoders were labeled sequentially, with A being in the southeast corner, B being in the southwest corner and C in the northwest corner.

The slope recorded between any two encoders was the inverse tangent of their relative displacement over their spacing. The first test showed that the relative displacement could be accurately determined, which left the spacing between encoders as an unknown. The third test was directed toward establishing this unknown and its uncertainty. This test was performed by lowering the surface encoder assembly onto a steel plate inclined at a known slope. From the recorded data the actual spacing between the probes could be determined.

A sine plate and a gage block were used to establish the known slope (Figure A4). The sine plate was a polished steel block supported by two parallel round bars attached to its underside. The block was flat to within 0.03 microns/mm and the bars were spaced to 127 mm +/-5 microns. The sine plate was initially leveled and the surface encoders were lowered onto it. The 25.4 mm-gage block was then inserted under one of the bars to give a slope of 11.54°. Since the accuracy of the gage block was within 0.25 microns, the accuracy of the slope was within 0.04 mrad.

Repeated measurements were taken between the four pairs of encoders and established the spacing between each to within 3.5 microns. This uncertainty was due to the encoders not being perfectly parallel with one another. Their spacing changed depending upon the absolute displacement. The resulting uncertainty identified in this test was 0.07 mrad between encoders A and B, 0.06 mrad between B and C, 0.13 mrad between C and D, and 0.09 mrad between D and A.

The effect of the spacing error decreased with slopes less than 11.5°. In fact, on a level surface, slope was independent of spacing error. Only two of the 384 slopes measured on the mold and facet were more than 11.5°. Therefore, the values above represent maximums and the actual spacing uncertainty varied between 0 and 0.13 mrad.

The spacing between encoders was independent of rocking of the encoder assembly. Both the spacing error and the rocking were assumed to have normal distributions, and the RMS value of the two yielded the total slope uncertainty. Table A3 gives these values for the four pairs of encoders. The maximum slope uncertainty was between encoders C and D and was 0.24 mrad. This represented the maximum slope uncertainty for a mold or facet analysis. However, the other pairs of encoders had less uncertainty. In fact, one pair had a maximum uncertainty of less than 0.08 mrad.

A3.2.2 Translational Calibration. Uncertainty in the Z-axis was primarily a function of variations in rail height. Other contributors included inaccuracy of the Z-axis encoder, thermal expansion, and inaccuracy of the surface encoders. Two tests were executed to define the uncertainty from rail height and Z axis encoder. Combined with the thermal expansion results and tests of the surface encoders, the total Z-axis uncertainty was defined.

The effect of rail height variations was tested by attaching a target to the base of the ball screw and recording the variation in its height in several random locations. The height was monitored with a Nikon automatic level, which had an accuracy of better than 0.005 mrad. Target range was between 1.5 and 5 m. Results indicated a one sigma variation of 0.05 mm in CDM height.

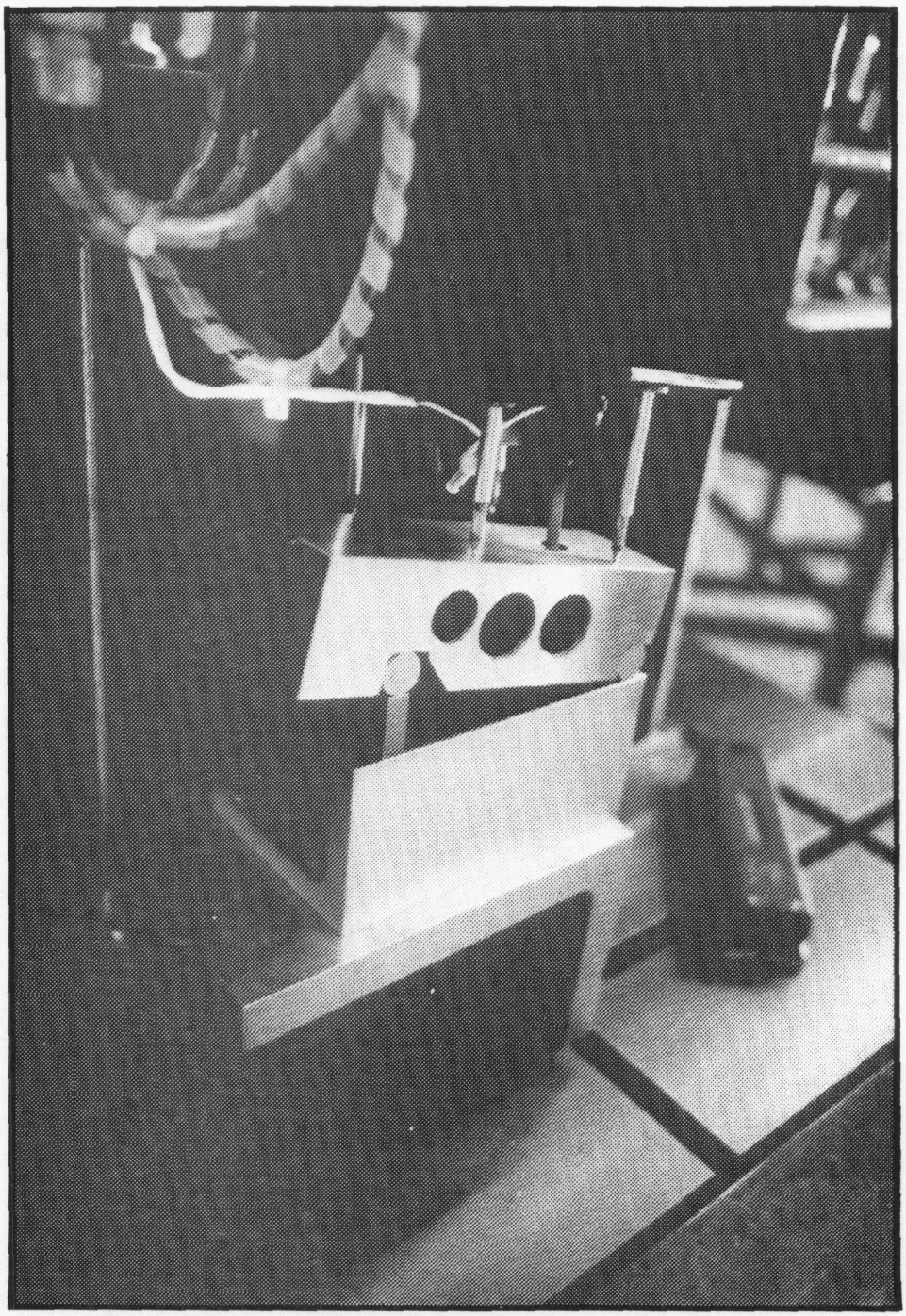

FIG. A4 SLOPE CALIBRATION

TABLE A3

SLOPE UNCERTAINTY

ENCODER PAIR	TEST 2 DUE TO ROCKING (mrad)	TEST 3* DUE TO SPACING (mrad)	TOTAL* (mrad)
A - B	.21	0 - .07	.21 - .22
B - C	.06	0 - .06	.06 - .08
C - D	.20	0 - .13	.20 - .24
D - A	.07	0 - .09	.07 - .11

* For slopes from zero to 11.5°

The accuracy of the 1.5-m long Z axis-encoder was defined by use of a 1-m standard. The standard had a calibrated accuracy of +/-0.9 microns against a secondary standard. Measurements of this standard with the Z-axis encoder indicated that the accuracy of the linear encoder was within the accuracy of the standard.

Uncertainty due to thermal expansion was determined analytically. The expansion coefficient of the carriages and ball screw was 11.7 mm/mm °C. The expansion coefficient for the linear encoder was similar (10.0 mm/mm °C). For measurements close to the surface table, thermal expansion had limited effect and was assumed to be zero. This was because the ball screw and carriage expanded and contracted as a unit, and expansion of the encoder was irrelevant in this position. At full retraction of the ball screw (maximum height), the expansion of the carriage and screw still canceled, but the change of length of the encoder became important. The temperature of the measuring system would vary only slightly during any given day, but could vary significantly according to the season. For this reason the temperature was recorded during every measurement session and compensations could be made. It was reasonable to assume that this compensation could be easily done within +/-3 °C. On this basis, the uncertainty due to thermal expansion ranged from 0 to 0.04 mm depending on extension of the screw.

Uncertainty of the surface encoders could also have impacted Z-axis uncertainty. However, previously mentioned tests showed that their effect was negligible.

The entire uncertainty of the Z measurements was the RMS value of these components. The result (as shown in Table A4) indicated an uncertainty from 0.05 to 0.06 mm corresponding to measurements at the surface and at maximum height, respectively.

Uncertainty of the Y measurements was established in four parts. First, the accuracy of the Y encoder was measured with the 1-m standard. The calibrated accuracy of the encoder was determined to be .008 mm. Second, the Y uncertainty associated with wobble and rocking of the ball screw was identified. From the detailed testing of the slope uncertainty, it was found that the ball screw's tilt was uncertain to 0.07 mrad along the Y-axis. This tilt resulted in an error of 0.1 mm with the screw fully extended. The error at lesser extensions would have been proportionally less. The camber of the X rails also contributed to Y uncertainty, and was measured independently. An automatic level was positioned at the end of the rail, and the camber was determined to be 0.05 mm. The last item that contributed to Y uncertainty was thermal expansion. The expansion coefficient of the Y encoder was 10.0 mm/mm °C. At the extreme ends of the travel, this resulted in an uncertainty of .02 mm, assuming compensation to within +/-3 °C. Table A5 summarizes the Y uncertainty. In the least favorable position (ball screw fully extended and Y/Z carriage to maximum travel) the uncertainty was 0.11 mm.

TABLE A4

Z UNCERTAINTY

SOURCE	UNCERTAINTY IN MOST FAVORABLE POSITION (mm)	UNCERTAINTY IN LEAST FAVORABLE POSITION (mm)
Rail height	0.05	0.05
Encoder	0.00	0.008
Temperature	0.00	0.04
Total (RMS)	0.05	0.06

TABLE A5

Y UNCERTAINTY

SOURCE	UNCERTAINTY IN MOST FAVORABLE POSITION (mm)	UNCERTAINTY IN LEAST FAVORABLE POSITION (mm)
Encoder	0	0.008
Rocking	0	0.10
Rail Camber	0.05	0.05
Temperature	0	0.02
Total (RMS)	0.05	0.11

X-axis uncertainty was subdivided into five categories. The first category was the uncertainty due to rocking of the ball screw in the X-direction. From the slope tests, the tilt in the X-direction was found to be 0.21 mrad. For the fully extended screw, this translated to 0.32 mm uncertainty. As described in the previous section, the X-axis measuring device was a friction wheel and rotary encoder assembly. The accuracy of this unit was confirmed by measurements of the 1-m standard. Uncertainty was primarily a result of slippage between the rail and wheel, and had a maximum value of 0.30 mm at the extremes of travel. Close to the reference point (center of X-travel) any error was negligible. The third category of X-uncertainty involved hysteresis of the X-carriage. Since the X-carriage was driven from one side only, the other side tended to lag behind a slight amount. This was measured by approaching a stop from both directions and measuring the difference. The hysteresis was measured at only 0.015 mm. The fourth category of X-error was due to the Y-rails not being square with the X-rails or perfectly straight. The uncertainty of this category was determined to be 0.17 mm by reference to the surface table. The final category--thermal expansion--was determined analytically. The friction wheel was aluminum and had an expansion coefficient of 23E-6 mm/mm °C. This resulted in a maximum uncertainty of X-measurements of 0.26 mm based on calibration to +/-3 °C. This represented the uncertainty at full travel. Uncertainty close to the center of the table would have been negligible. Table A6 summarizes the results of the X-uncertainty. In the worst possible orientation (ball screw fully extended and at the end of X-travel), the uncertainty was 0.53 mm.

Table A7 summarizes the uncertainty of all measurements. The minimum and maximum uncertainty represent the span of uncertainty for any measurement depending on location and encoder groups. The critical value is the maximum slope uncertainty of 0.24 mrad. This means that the actual slope values of the facet and mold could be measured, with confidence, to better than 0.24 mrad.

TABLE A6

X-UNCERTAINTY

SOURCE	UNCERTAINTY IN MOST FAVORABLE POSITION (mm)	UNCERTAINTY IN LEAST FAVORABLE POSITION (mm)
Rocking	0	0.32
Encoder	0	0.30
Hysteresis	0.015	0.015
Y rail placement	0.17	0.17
Temperature	0	0.26
Total (RMS)	0.17	0.54

TABLE A7

MEASURING SYSTEM UNCERTAINTY
FROM CALIBRATION

	RANGE	UNCERTAINTY
Slope		0.06 - 0.24 mrad
X-axis	7.5 m	0.17 - 0.54 mm
Y-axis	1.8 m	0.05 - 0.11 mm
Z-axis	1.5 m	0.05 - 0.06 mm

A.4 Data Analysis Procedure

The CDM was designed and built to allow precise measurement of the surface contours of an optical panel. The data taken by the measurement system required extensive processing to convert the raw numbers into a useable form. The objectives of the processing program were

* Determine the accuracy of the mold and gore. A convenient way of characterizing the surface is by the computation of the one sigma slope error.

* Identify large and small slope errors in such a way that their location and relative contribution to slope error are known and that the appropriate corrective refinements to the adjustable mold can be made.

A map was developed to locate the X- and Y-coordinates at which measurements should be recorded. The selected points reflected the quality of the entire gore and did not bias results toward certain portions of the panel. Points were selected along the edge and center. The number of points was weighted according to area. Adjustment points on the mold were selected as a basis for layout. Figure A5 illustrates the map and cluster numbering sequence that was used. Each square cluster represents the points simultaneously recorded by the set of four surface encoders. Determination of slope was based on the relative height of the points within a cluster and was not dependent on the spacing between clusters.

Considerable uncertainty existed in the manual positioning of a large panel. The exact location of the measured piece with respect to the measurement machine coordinate system could not be predetermined. A procedure was developed to determine the relative position based upon minimizing slope error. For a parabolic gore, the equation governing the shape of this ideal panel would be

$$4Fz = x^2 + y^2,$$

where F is the focal length and X, Y, and Z are the Cartesian coordinates. Figure A6 illustrates the coordinate transformation.

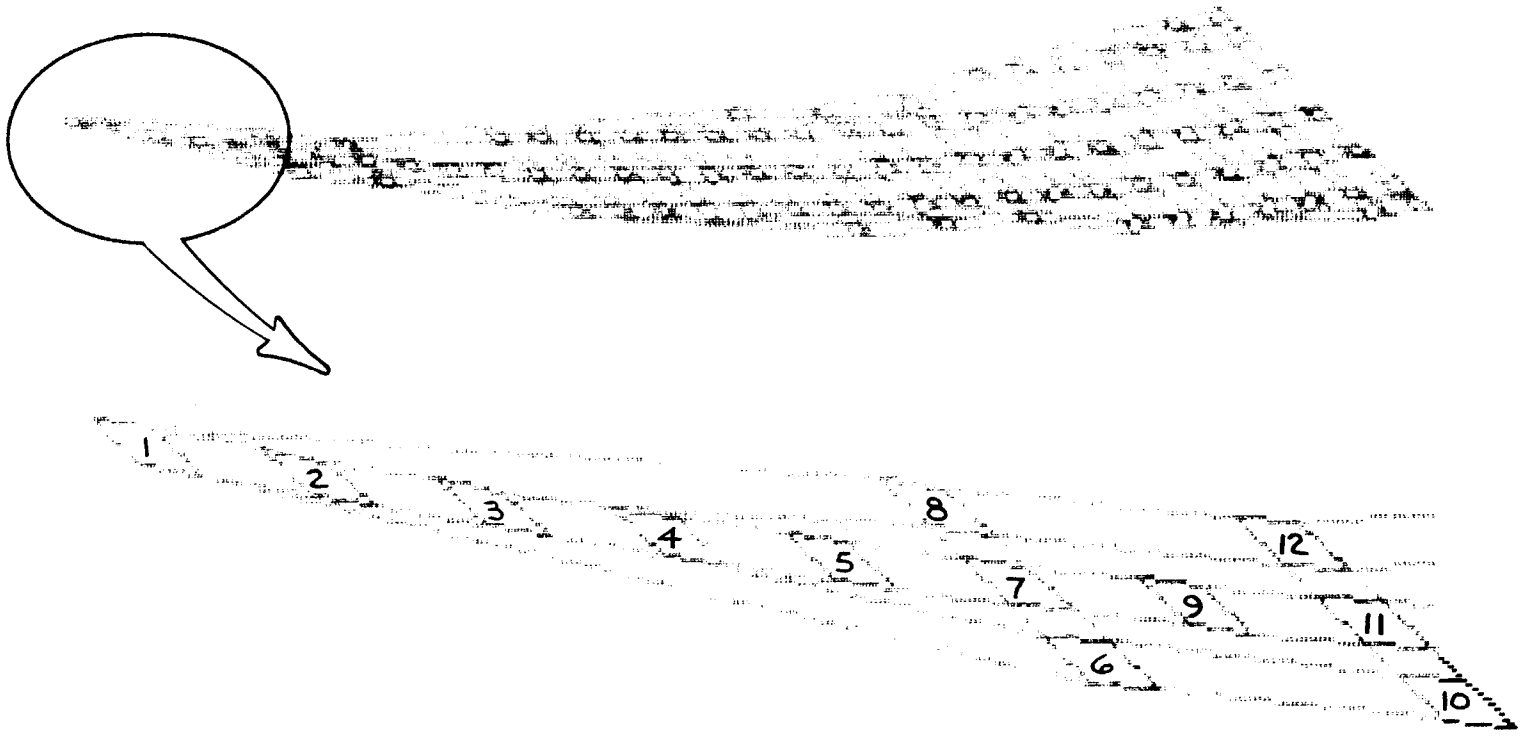

FIG. A5 MEASUREMENT MAP AND CLUSTER NUMBERING SEQUENCE FOR MOLD AND GORE

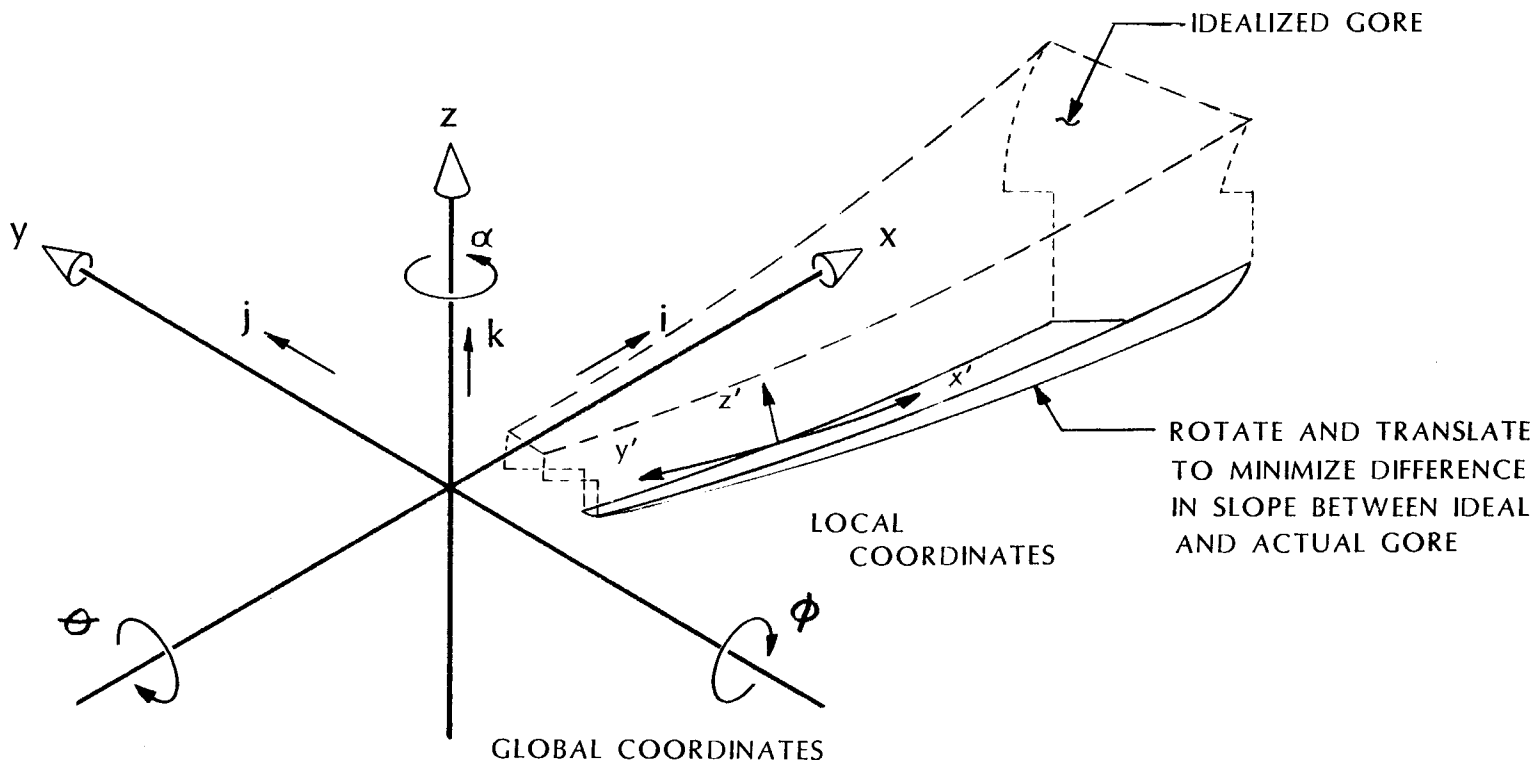

FIG. A6 TRANSFORMATION OF LOCAL TO GLOBAL COORDINATES

The seven variables pertinent to this transformation were

F - Focal length
O - Rotation about the X-axis
O - Rotation about the Y-axis
  - Rotation about the Z-axis
i - Translation along X
j - Translation along Y
k - Translation along Z

Accuracy was most sensitive to rotation about X- and Y-axes. The transformation was particularly sensitive to rotation about the X and Y-axes. The remaining variables impacted slope in a less direct fashion, or not at all. The focal length, rotation about the Z-axis, and the translators in the X- and Y-direction could generally be determined through direct measurement, with accuracy sufficient with little or no impact upon the selection of critical transformation variables. The Z-translator had no impact upon slope error or coordinate transformation. The X transformation coordinate was useful for graphic presentation and was determined with the numerical iteration on transformation variables.

The transformation variables were assumed and the slope error of the facet was calculated based upon this assumed relative position of global and local axes. The most sensitive variables (rotation about X and Y) were adjusted first to reduce error. The iteration was defined as acceptable when additional passes could not improve the slope match better than 0.001 mrad. The secondary variables (focal length, i, j) were adjusted next. The lower sensitivity resulted in a slower convergence. The same error criterion was used for an acceptable fit. Subsequent adjustment about or along the Z-axis did not improve or detract from the transformation.

Initially, the iterative procedure was tested with several sets of generated data with known error distributions that were randomly and systematically imposed upon a facet. The facet was randomly oriented with respect to the global axis within the bounds of accuracy on each transformation variable that could be predetermined with conventional measurement equipment. The iterative procedure was successful at predicting the slope errors of the generated data within the 0.001-mrad accuracy requirement. As the difference between initial assumptions and actual transformation increased, the number of iterations required did increase. Computation times were acceptable for facets of reasonable shape. The numerical iteration screen output is illustrated in Figure A7.

THE MOST CURRENT VALUES ARE AT THE TOP OF EACH COLUMN

PASS NUMBER	5	
X SLOPE ERROR (MR)	Y SLOPE ERROR (MR)	FOCAL LENGTH (INCHES)
.7174	.5177	275.5900
.7173	.5177	275.5900
.7173	.5181	275.5900
.8490	2.3635	275.5900
24.3392	26.5497	275.5900

THETA ROTATION (DEGS)	PHI ROTATION (DEGS)	Z TRANSLATOR (INCHES)
-.0009	-15.3403	-24.4442
-.0009	-15.3403	-24.4442
-.0022	-15.3397	-24.4423
.1299	-15.3137	-24.3568
.0001	-15.3400	-24.3641

X TRANSLATOR (INCHES)	Y TRANSLATOR (INCHES)
.00000	.00000
.00000	.00000
.00000	.00000
.00000	.00000
.00000	.00000

FIG. A7 NUMERICAL ITERATION DISPLAY

The calculation of slope error is simply the difference between the measured slope value and the transformed ideal slope. The slope error is defined at each cluster on the map. The slope error at any measured point may also be presented. This absolute information was particularly useful in the adjustment of the mold and the comparison of error location in the facet and mold.

The data can also be presented in graphic format by superimposing the error and transformed ideal optical element. The error can be independently scaled to observe effects of different magnitude. Figure A8 illustrates the type of graphic output used. The error was scaled to eliminate minor and random error in order to dramatize a relaxed corner; a systematic error.

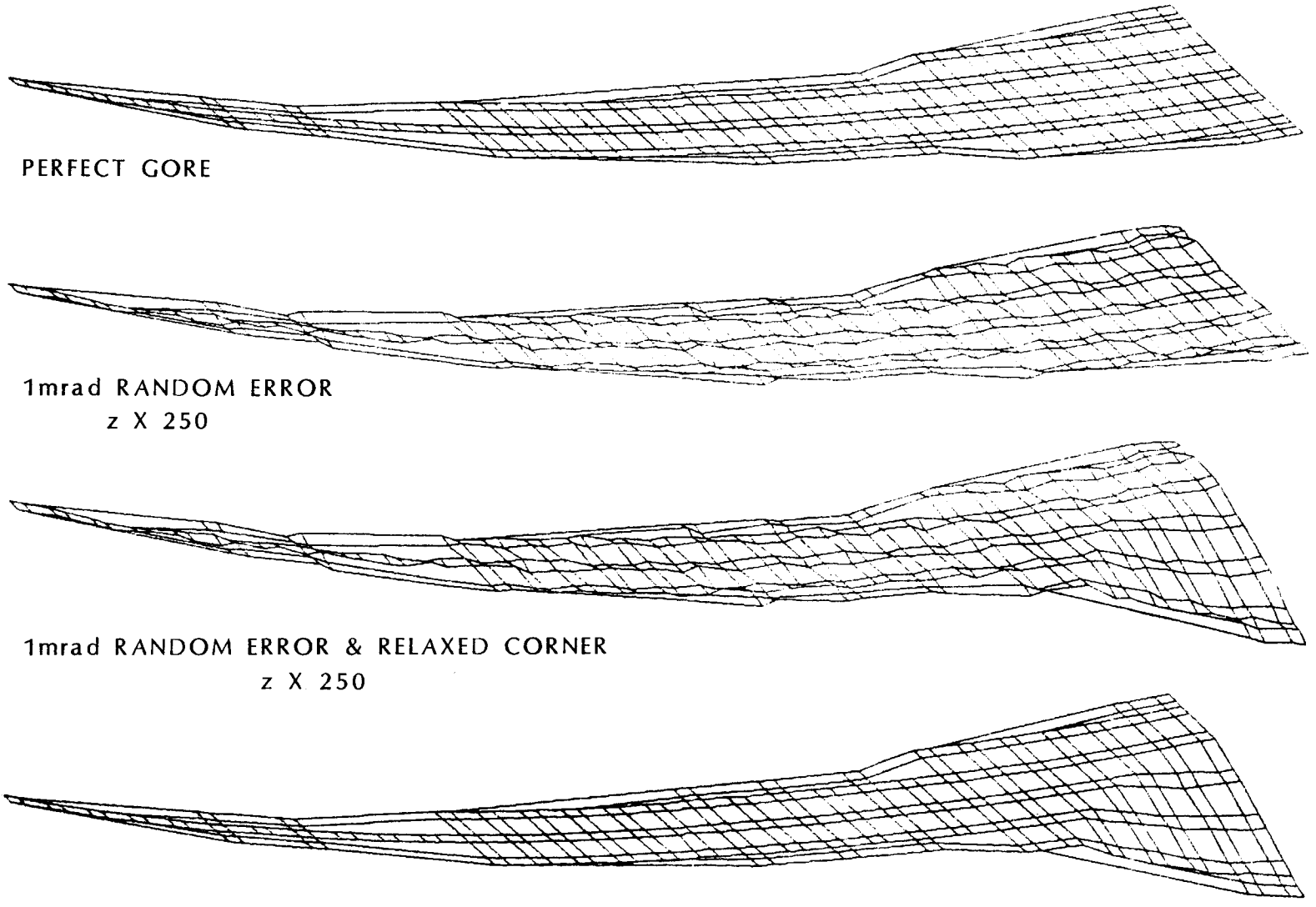

FIG. A8 REPRESENTATIVE GRAPHICAL OUTPUT

A.5 Conclusion

The measurement system developed under this contract has the capability to accurately quantify displacement and slope of large area contour tooling and concentrator facets. The CDM can provide the precise feedback required to identify systematic slope error in a facet and correct the problem through tool adjustment. The system performance exceeded the projected accuracy. Uncertainty in slope measurements, the key performance characteristic of a reflecting solar concentrator, was 0.24 mrad.

The data generated from the measurement equipment was successfully analyzed and are presented in numeric and graphic formats. The relationship between the facet and the global CDM axes was defined statistically to eliminate reliance upon arbitrary tooling marks. Data translation and analysis had little impact upon the uncertainty of the measurements.

APPENDIX B

THREE-DIMENSIONAL ROLL BENDING

The baseline optical panel design required that the skins be formed to the final contour prior to being assembled as a panel. This approach, as opposed to using unformed sheets, reduced spring-back loads and allowed more latitude in panel construction design.

The two conventional approaches to forming aluminum sheets to three-dimensional contours have significant shortcomings; namely large initial costs and poor production capabilities. For this reason, an innovative method of forming sheets was pursued. This new method, termed "three-dimensional (3-D) roll bending," is similar to conventional roll bending in that a set of rollers is used to bend the sheet about one axis. The difference is that the 3-D roll distorts each roller to provide a contour about the second axis that results in a three-dimensional (dished) part.

The development effort did not initially prove to be successful. Further effort was abandoned when prototype samples indicated that skin forming was not required.

B.1 Background

Stretch forming and stamping are two conventional approaches to forming sheets into three-dimensional shapes. The stretch forming process uses a flat piece of sheet metal and stretches it over a punch. The punch is an accurately formed mold in the desired shape of the part. This process is slow and is not conducive to high production rates. The punch is a large, accurate part, and the process suffers from high cost. A large scrap loss for gore-shaped parts was inherent with this technique. The stock material had to be rectangular; approximately 50 percent of the stock served only as a carrier for the skin and was subsequently lost.

Stamping overcame many of these drawbacks. The production rate was adequate and scrap loss was reduced. Trim allowance did continue to impose some scrap, however, and cost was substantial. Preliminary investigations indicated that tooling would be prohibitive in a prototype investigation effort. There were indications that production costs of large gores would also be prohibitive and the baseline design would require alteration to accommodate inner and outer petals. This design accommodation increased scrap and part complexity. Consequently, three-dimensional roll bending was explored.

B.2 Description

Three-dimensional roll bending had the potential to greatly reduce the cost of forming compound curves in sheet metal. If successful, complex parts could have been produced in a continuous coil line process at high production rates and low costs.

The configuration of the rolls was the first major question in the development of the roll former. Four major possibilites existed: a pyramid, three-roll single pinch, three-roll double pinch, and four-roll double pinch (Figure B1).

The pyramid is a common bending roll; the top roll moves up and down to control the radius of curvature. The symmetric bending of this process resulted in a length of material at both the trailing and leading edge of a sheet that would not be formed.

The three-roll single-pinch machine overcame part of this problem. The bottom or top roll was adjusted to pinch the material and form the perpendicular curve, and the outboard roll was adjusted to form the radius of curvature along the gore. It was possible to prebend the leading edge only; the trailing edge could be bent only by turning the material end for end.

The three-roll double-pinch machine allowed prebend on both the leading and trailing edges, with bending in the perpendicular plane occurring in the more desirable pinch direction. Unfortunately, the lack of a fixed reference for bending complicated the numerical controls of the roll positions.

Finally, the four-roll machine incorporated all of the desirable features at the expense of increased complexity by virtue of the additional roll.

The conceptual approach is shown in Figure B2. A three-roll double-pinch arrangement was used because it offered the best restraint and control of the sheet. The three-roll configuration provided the conventional curvature about one axis. Curvature about the second axis was induced by the curvature of the rolls themselves. The curvature of the rolls could be controlled by a set of motorized rams as support rolls. Change in the curvature of the rolls, and the relative position of one roll to another, resulted in a change in shape. This shape change provided control of the radius of curvature from one end to the other as was required in a gore.

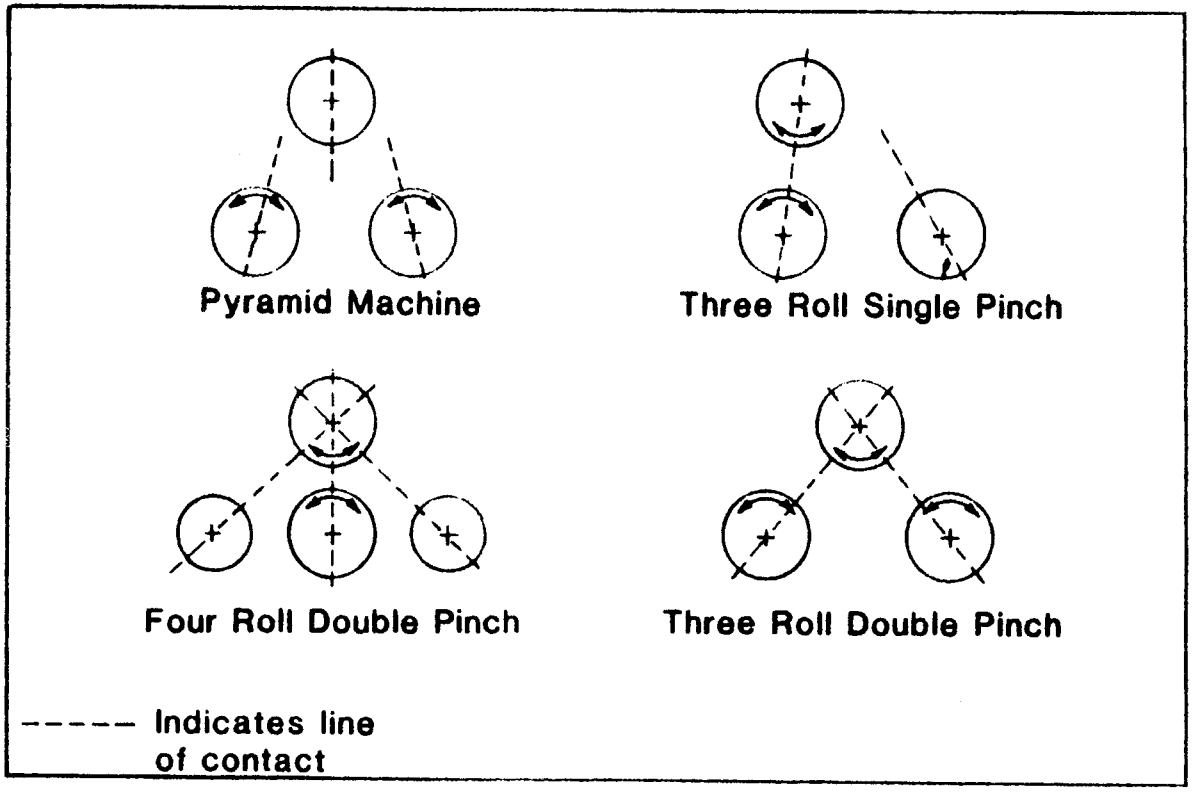

FIG. B1 TYPICAL ROLL CONFIGURATIONS

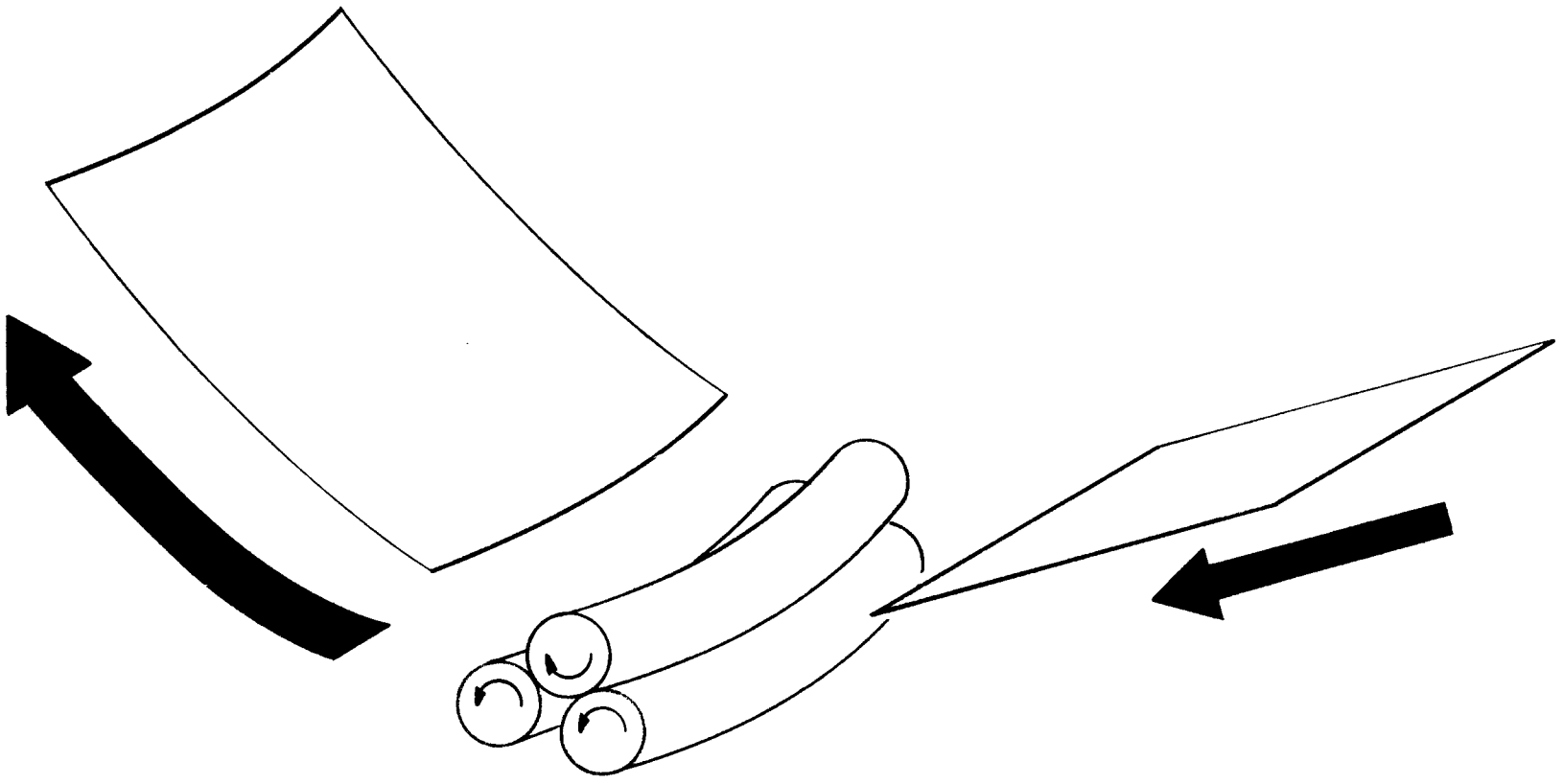

FIG. B2 THREE DIMENSIONAL ROLL FORMER

To address the feasibility of this innovative concept, a small-scale roll former was built and tested. To avoid the high costs associated with controlling the curvature of the rolls, a set of rolls was machined to simulate this effect (Figure B3). The top roll was made convex, and the two lower rolls had matching concave surfaces. The upper roll was adjustable in the vertical direction and pushed against the lower two rolls (Figure B4). The lower two rolls could translate in the horizontal plane but were forced toward each other with hydraulic cylinders. Their travel was limited by contact with the top roll. Adjustment of the height of the top roll controlled the position of the bottom rolls and, therefore, controlled the curvature about one axis.

Figure B5 shows the roll former. The two vertical jack screws in the top of the figure were used for top roll adjustment. Hydraulic pressure was supplied by a pump located beneath the rolls. The horizontal, cylindrical shaft seen above these rolls served as a brace for the housing and was not used for forming.

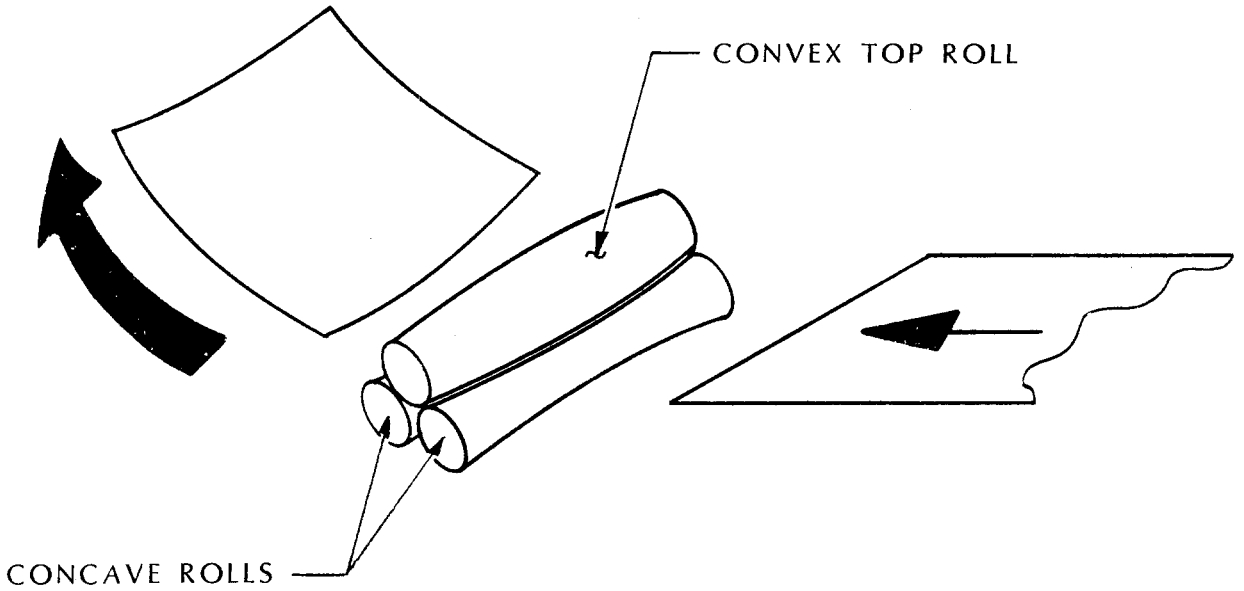

FIG. B3 ROLL FORMER CONFIGURATION

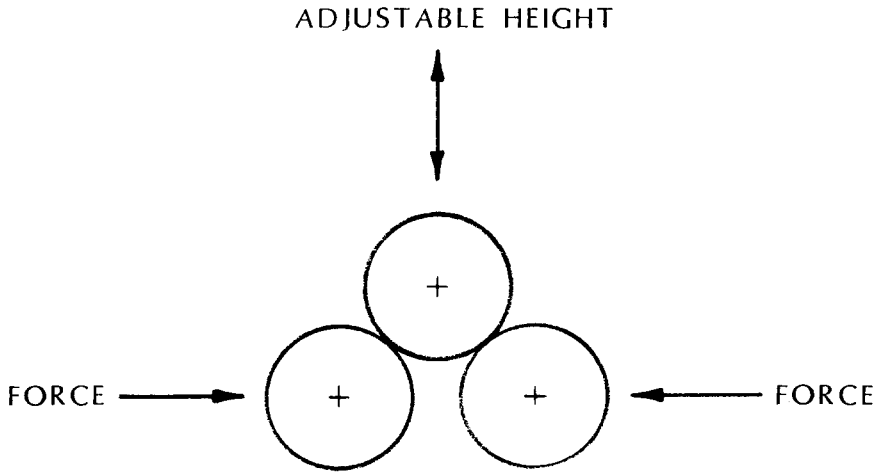

FIG. B4 ROLLER CONTROL

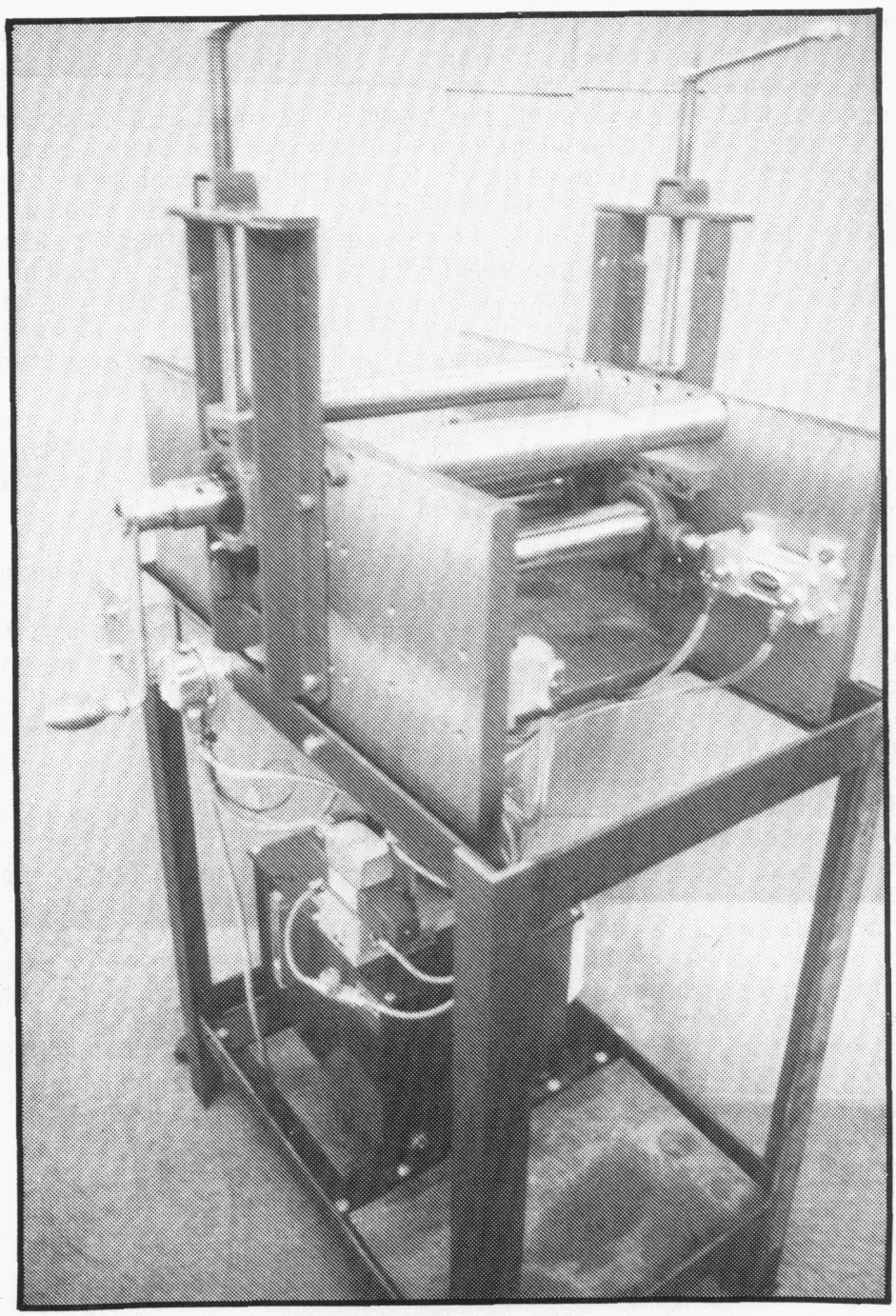

FIG. B5 THREE-DIMENSIONAL ROLL FORMER

B.3 Results

Analysis of the expected stress distribution in a parabolic gore section indicated that the edges of the sheet would need to be closely controlled during forming to avoid buckling. Buckling would be caused by the high compressive stress along the edges of the sheets. This stress could be visualized by using a rectangular sheet as an example. If the sheet were rolled in a conventional former, no part of the sheet would change length. The deformation would be caused completely by bending stresses across the thickness of the sheet. In forming a compound shape, the sheet would change length. The primary stresses would be axial rather than bending. The sheet would minimize its strain energy, and half the sheet would be in axial tension while the other half would be in axial compression. The magnitude of these stresses would be large. In fact, to permanently form the sheet, the stresses would have to be greater than the yield strength. Axial tensile loads above yield would not necessarily be troublesome, but axial compressive loads of this magnitude might easily produce instabilities (buckling) in sheet metal.

Initial results with the roll former proved that this was the case. The edges of the sheets buckled and no repeatable shape was achieved in the first set of tests.

Two approaches were taken to eliminate buckling. The unsupported span of the sheet was minimized, and the compressive stress in the sheet was reduced. The first approach required modification of the rolls to allow a closer fit. This changed the buckling pattern but did not eliminate it. The second approach used the motion of the top roll and a high pinching pressure between the rolls to stretch the part as it was being formed.

The imposition of tensile membrane stress through stretch eliminated the buckling but created other difficulties. Figure B6 shows the parts made by this method. Figure B6(A) represents the shape achieved initially. The desired part had a dished contour with all edges rising, the edges of the actual part dropped, creating a saddle shape. It is believed that this effect was caused not by axial or bending loads, but by cold working. In order to hold the part tightly enough to allow stretching, the pressure of the rolls yielded the metal between each roll. This compressive yielding across the thickness caused the sheets to elongate. The longer sections then tended to have a larger radius of curvature (due to larger circumference) in the opposite direction, thus creating the saddle shape.

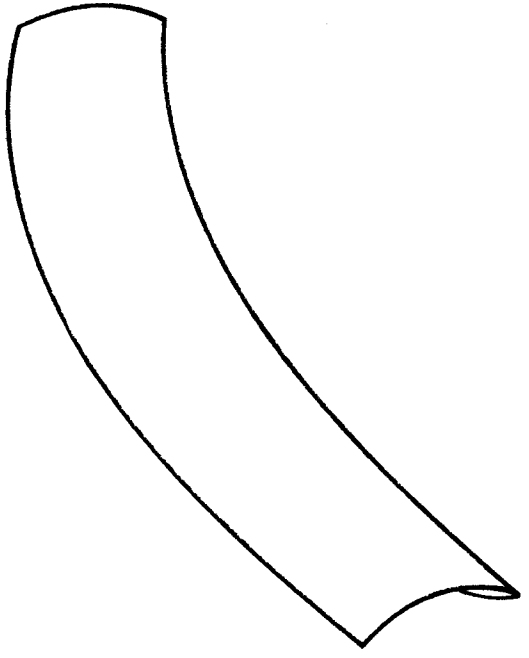

SADDLE
(A)

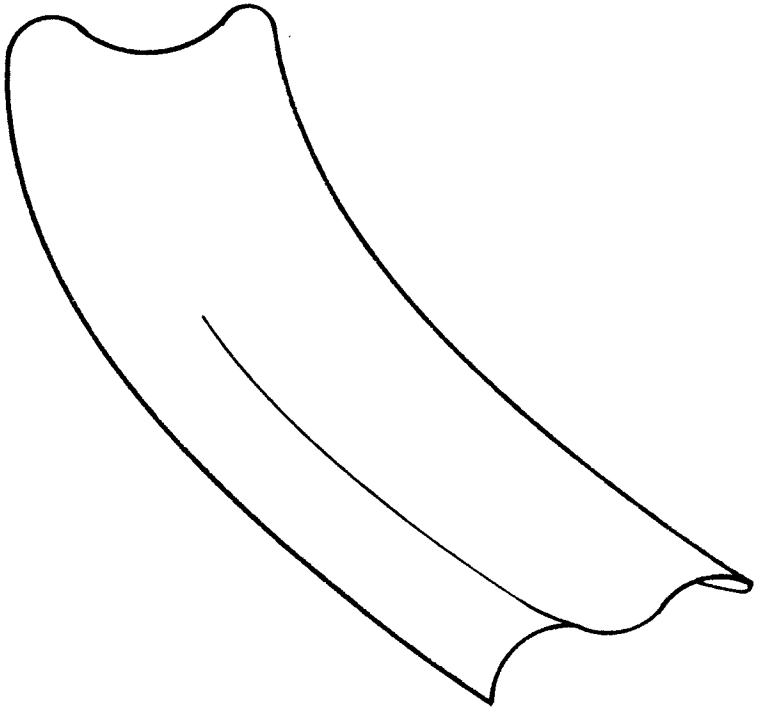

DOUBLE SADDLE
(B)

FIG. B6 THREE DIMENSIONAL ROLL FORMED SHAPES

Some experimentation was done to try to control the cold working in such a way that the cold working itself would cause the desired shape. It was found that this approach was extremely sensitive to many subtleties. For instance, nominal variations in stock thickness (from piece to piece and across the width of a sheet) caused significant changes in the final part. Slight imperfections in the contour of the rolls were greatly exaggerated. Figure B6(B) represents the shape in these attempts. The process could not be controlled.

From the testing done with a small-scale, modified roll former, it was concluded that three-dimensional roll bending of sheet metal cannot be used to form dish skins. Although combined cold working and roll forming can create three-dimensional shapes, control of the process makes it impractical as a forming method.

STANDARD DISTRIBUTION FOR SAND REPORTS

DOE/TIC-4500(Rev.74)UC-62 (328)

AAI Corporation
P.O. Box 6787
Baltimore, MD 21204

Acurex Aerotherm (2)
555 Clyde Avenue
Mountain View, CA 94039
Attn: J. Schaefer
H. Morse

Alabama A&M University (2)
Department of Physics
P.O. Box 271
Normal, AL 35762
Attn: M. D. Aggarwal
A. Tan

Alpha Solarco
600 Vine St.
Cincinnati, OH 45202

Applied Concepts
405 Stoney Creek Blvd.
P.O. Box 490
Edinburg, VA 22824
Attn: J. S. Hauger

Applied Concepts
2501 S. Larimer County Rd. 21
Berthound, CO 80513
Attn: S. Pond

Arizona Public Service Co. (2)
P.O. Box 21666
Phoenix, AZ 85036
Attn: J. McGuirk
E. Weber

Australian National University
Department of Engineering Physics
P.O. Box 4
Canberra ACT 2600, AUSTRALIA
Attn: Prof. Stephen Kaneff

Barber-Nichols Engineering
6325 West 55th Ave.
Arvada, CO 80002
Attn: R. Barber

BDM Corporation
1801 Randolph Street
Albuquerque, NM 87106
Attn: W. E. Schwinkendorf

Battelle Memorial Institute
Pacific Northwest Laboratory
4000 NE 41st St.
Seattle, WA 98105
Attn: K. Drumheller

Battelle Memorial Institute
Pacific Northwest Laboratory
P.O. Box 999
Richland, WA 99352
Attn: T. Williams

Bechtel Group, Inc.
P.O. Box 3965
50 Beale Street
San Francisco, CA 94119
Attn: P. DeLaquil

Black & Veatch
P.O. Box 8405
Kansas City, MO 64114
Attn: J. C. Grosskreutz

Boeing Engineering & Construction
P.O. Box 3999
Seattle, WA 98124
Attn: R. Gillette

Budd Company (The)
Fort Washington, PA 19034
Attn: W. W. Dickhart

Budd Company (The)
Plastic R&D Center
356 Executive Drive
Troy, MI 48084
Attn: K. A. Iseler

Burns & Roe (2)
800 Kinderkamack Road
Oradell, NJ 07649
Attn: G. Fontana
R. Cherdack

California Energy Commission
1516 - 9th Street
Sacramento, CA 95814
Attn: Alec Jenkins

Cal Poly State University
San Luis Obisbo, CA 93407
Attn: E. J. Carnegie

California Institute of Technology
Aeronautics Library
MS 205-45
Pasadena, CA 91125
Attn: Jean Anderson

California Polytechnic University
Dept. of Mechanical Engineering
Pamona, CA 91768
Attn: W. B. Stine

Chicago Bridge and Iron
800 Jorie Blvd.
Oak Brook, IL 60521
Attn: J. M. Shah

Colorado State University
Ft. Collins, CO 80523
Attn: T. G. Lenz

Columbia Gas System Service Corp.
1600 Dublin Road
Columbus, OH 43215
Attn: J. Philip Dechow

Datron Systems, Inc.
200 West Los Angeles Ave.
Simi Valley, CA 93065-1650

DSET
Box 1850
Black Canyon Stage I
Phoenix, AZ 85029
Attn: G. A. Zerlaut

Donnelly Corporation
49 West Third Street
Holland, MI 49423
Attn: M. DeVries

Electric Power Research Inst. (2)
3412 Hillview Avenue
Palo Alto, CA 94303
Attn: E. A. Demeo
J. E. Cummings

Energy Technology Engr. Ctr.
Rockwell International Corp.
P.O. Box 1449
Canoga Park, CA 91304
Attn: W. L. Bigelow

ENTECH, Inc. (3)
P.O. Box 612246
DFW Airport, TX 75261
Attn: R. R. Walters
W. Hesse
M. O'Neill

Eurodrive, Inc.
30599 San Antonio Rd.
Hayward, CA 94544

Florida Solar Energy Center
300 State Road 401
Cape Canaveral, FL 32920
Attn: Library

Ford Aerospace
Ford Road
Newport Beach, CA 92663
Attn: R. H. Babbe

Ford Motor Company
Glass Div., Technical Center
25500 West Outer Drive
Lincoln Park, MI 48246
Attn: V. L. Lindberg

Foster Wheeler Solar Dev. Corp. (2)
12 Peach Tree Hill Road
Livingston, NJ 07039
Attn: M. D. Garber
R. J. Zoschak

Garrett Turbine Engine Co.
111 South 34th Street
P.O. Box 5217
Phoenix, AZ 85010
Attn: Ed Strain

Georgia Power Co.
7 Solar Circle
Shenandoah, GA 30264
Attn: E. Ney

Heery Energy Consultants, Inc.
Project Energy Manager
880 West Peachtree St. NW
Atlanta, GA 30309
Attn: Glenn Bellamy

Highland Plating
10001 N. Orange Drive
Los Angeles, CA 90038
Attn: M. Faith

Industrial Solar Technologies
5775 West 52nd Ave.
Denver, CO 80212
Attn: Randy Gee

Institute of Gas Technology
Attn: Library
34245 State Street
Chicago, IL 60616

Jet Propulsion Laboratory
4800 Oak Grove Drive
Pasadena, CA 91109
Attn: M. Alper

Kearney & Associates
14022 Condessa Drive
Del Mar, CA 92014
Attn: David W. Kearney

LaCour Kiln Service
P.O. Box 247
Canton, MS 39046
Attn: J. A. LaCour

LaJet Energy Co. (2)
P.O. Box 3599
Abilene, TX 79604
Attn: Monte McGlaun
Carl Williams

L'Garde, Inc.
1555 Placentia Avenue
Newport Beach, CA 92663
Attn: Mitchell Thomas

John Lucas
865 Canterbury Road
San Marino, CA 91108

Martin Marietta Corp. (2)
12250 So. Hwy. 75
Littleton, CO 80125
Attn: Tom Tracey
H. Wroten

McCarter Corporation
200 E. Washington St.
P.O. Box 351
Norristown, PA 19404
Attn: R. A. Powell

McDonnell-Douglas Astronautics
Company (3)
5301 Bolsa Avenue
Huntington Beach, CA 92647
Attn: R. L. Gervais
J. Rogan
D. Steinmeyer

Mechanical Technology, Inc. (2)
968 Albany Shaker Road
Latham, NY 12110
Attn: G. R. Dochat
J. Wagner

Meridian Corporation
5113 Leesburg Pike
Suite 700
Falls Church, VA 22041
Attn: D. Kumar

Midwest Research Institute (2)
425 Volker Blvd.
Kansas City, MO 64110
Attn: R. L. Martin
J. Williamson

NASA Lewis Research Center
21000 Brook Park Road
Cleveland, OH 44135
Attn: R. Beremand, MS 301-2
J. Savino, MS 301-5
T. McCoy, MS 301-5
R. Puthoff
R. Corrigan

New Mexico Solar Energy Institute
New Mexico State University
Box 3SOL
Las Cruces, NM 88003

Parsons of California
P.O. Box 6189
Stockton, CA 95206
Attn: D. R. Biddle

PG&E
3400 Crow Canyon Rd.
San Ramon, CA 94583
Attn: J. Iannucci
G. Braun

Polydyne, Inc.
1900 S. Norfolk St., Suite 209
San Mateo, CA 94403
Attn: Peter Bos

Power Kinetics, Inc.
415 River Street
Troy, NY 12180-2822
Attn: W. E. Rogers

Reinhold Industries
Division of Keene Corp.
1287 E. Imperial Highway
Santa Fe Springs, CA 90670
Attn: J. Flynt

Renewable Energy Institute
1001 Connecticut Avenue NW
Suite 719
Washington, DC 20036
Attn: Kevin Porter

Research Systems, Inc.
Suburban Trust Bldg.,
Suite 203
5410 Indian Head Hwy.
Oxon Hill, MD 20745
Attn: T. A. Chubb

Rockwell International
Energy Systems Group
8900 De Soto Avenue
Canoga Park, CA 91304
Attn: T. Springer

Rockwell International
Space Station Systems Division
12214 Lakewood Blvd.
Downey, CA 90241
Attn: I. M. Chen

Sanders Associates
MER 15-2350
C.S. 2035
Nashua, NH 03061-2035
Attn: J. Kesseli

Science Applications
International Corp.
10401 Roselle Street
San Diego, CA 92121
Attn: Barry Butler

Solactor Corporation
2065 Keystone Blvd.
Miami, FL 33181
Attn: Joseph Womack

Solar Energy Industries Association
Suite 610
1730 North Lynn St.
Arlington, VA 22209-2009
Attn: C. LaPorta

Solar Energy Research Inst. (6)
1617 Cole Blvd.
Golden, CO 80401
Attn: D. Blake
B. P. Gupta
J. Thornton
D. Johnson
M. Murphy
D. Hawkins

Solar Kinetics, Inc.
P.O. Box 540636
Dallas, TX 75354-0636
Attn: J. A. Hutchison

Solar Steam
P.O. Box 32
Fox Island, WA 98333
Attn: D. E. Wood

Southern California Edison (3)
P.O. Box 800
Rosemead, CA 92807
Attn: J. N. Reeves
P. Skvarna

SLEMCO
19655 Redberry Dr.
Los Gatos, CA 95030
Attn: A. J. Slemmons

Stearns-Catalytic Corp.
Box 5888
Denver, CO 80217
Attn: T. E. Olson

Stirling Thermal Motors
2841 Boardwalk
Ann Arbor, MI 48104
Attn: Ben Ziph

Sun Exploration and Production Co.
P.O. Box 2880
Dallas, TX 75221-2880
Attn: R. I. Benner

Sun Power, Inc.
6 Byard St.
Athens, OH 45701
Attn: Mac Thayer

Sundstrand ATG
P.O. Box 7002
Rockford, IL 61125
Attn: D. Chaudoir

Suntec Systems, Inc.
P.O. Box 315
Savage, MN 55378
Attn: Harrison Randolph
J. H. Davison

Swedlow, Inc.
12122 Western Avenue
Garden Grove, CA 92645
Attn: E. Nixon

3M-Energy Control Products (2)
207-1W 3M Center
St. Paul, MN 55144
Attn: B. Benson
J. L. Roche

Texas Tech University
Dept. of Electrical Engineering
P.O. Box 4439
Lubbock, TX 79409
Attn: E. A. O'Hair

TRW (3)
Space & Technology Group
One Space Park
Redondo Beach, CA 90278
Attn: G. M. Reppucci
A. D. Schoenfeld
J. S. Archer

U.S. Department of Energy (4)
Albuquerque Operations Office
P.O. Box 5400
Albuquerque, NM 87185
Attn: C. Garcia
D. Graves
N. Lackey

U.S. Department of Energy
Office of Solar Heat Technologies
Forrestal Building
Washington, DC 20585
Attn: Fred Morse

U.S. Department of Energy
Office of Solar Heat Technologies
Forrestal Building
Washington, DC 20585
Attn: C. Carwile

U.S. Department of Energy
Division of Solar Thermal Tech.
Forrestal Building
Washington, DC 20585
Attn: Howard S. Coleman
R. Shivers
~~J. Greyerbiehl~~
S. Gronich
C. Mangold
M. Scheve
F. Wilkins

U.S. Department of Energy
San Francisco Operations Ofc.
1333 Broadway
Oakland, CA 94612
Attn: R. W. Hughey

U.S. Robotics
8100 N. McCormack Blvd.
Skokie, IL 60076
Attn: Paul Collard

University of Houston (2)
Energy Laboratory; SPA
Houston, TX 77004
Attn: Lorin Vant-Hull
A. F. Hildebrandt

University of New Mexico (2)
Department of Mechanical Engr.
Albuquerque, NM 87131
Attn: M. W. Wilden
W. A. Gross

Viking Solar Systems, Inc.
1850 Earlmont Ave.
La Canada, CA 91011
Attn: George Goranson

WG Associates
6607 Stonebrook Circle
Dallas, TX 75240
Attn: Vern Goldberg

0400 R. P. Stromberg
1510 J. W. Nunziato
1513 D. W. Larson
1810 R. G. Kepler
1820 R. E. Whan
1824 J. N. Sweet
1830 M. J. Davis
1832 W. B. Jones
1840 R. J. Eagan
1841 R. B. Diegle
1842 R. E. Loehman
1846 D. H. Doughty
2520 N. J. Magnani
2525 R. P. Clark
2540 G. N. Beeler
2541 J. P. Abbin
3141 S. A. Landenberger (5)
3151 W. L. Garner (3)
3154 C. H. Dalin
3160 J. E. Mitchell
6000 D. L. Hartley
6200 V. L. Dugan
6220 D. G. Schueler
6221 E. C. Boes
6222 J. V. Otts
6223 G. J. Jones
6224 D. E. Arvizu
6225 H. M. Dodd
6226 J. T. Holmes
6227 J. A. Leonard (20)
6250 B. W. Marshall
6254 B. Granoff
7470 J. L. Ledman
7471 D. L. Stewart
8024 P. W. Dean
8470 R. L. Rinne
8471 A. C. Skinrood